Structure and magnetism of defected carbon materials

Doctoral Thesis

to obtain the degree of doctor
from Radboud University Nijmegen

by

Mikhail A. Akhukov

Structure and magnetism of defected carbon materials

Mikhail A. Akhukov

Cover image: spin density isosurface plot of the sample AC09-0708, see Fig. 5.12.

Structure and magnetism of defected carbon materials

Proefschrift

ter verkrijging van de graad van doctor
aan de Radboud Universiteit Nijmegen
op gezag van de rector magnificus prof. mr. S. C. J. J. Kortmann,
volgens besluit van het college van decanen
in het openbaar te verdedigen op maandag 25 februari 2013
om 10:30 uur precies

door

Mikhail A. Akhukov

geboren op 28 Mei 1982
te Orenburg, Rusland

Contents

Chapter 1

Introduction

1.1 Magnetism in carbon materials

Carbon has a unique place among all elements. Its position in the middle of the second period of the periodic table of elements allows different types of hybridization of its 4 valence electrons during the formation of covalent bonds like sp (triple bonds), sp^2 (graphitic bond) and sp^3 (diamond bond). This feature explains the variety of its allotropes and compounds with other elements. Within all possible allotropes, probably, graphene shown in Fig. 1.1 is the most interesting at the moment[1].

Graphene is a one atom thick two-dimensional allotrope of carbon where all atoms are in sp^2 hybridization. It has the honeycomb hexagonal lattice which can be represented as a Bravais lattice with a basis. The two atoms in the unit cell define two interpenetrating lattices that make graphene a bipartite structure. This feature leads to its unique structural and electronic properties and will play an important role in our search for magnetic states.

All carbon nanostructures derived from graphene like nanoribbons, graphene with grain boundaries and nanotubes inherit many of its properties and introduce new ones. Beside graphene and its derivatives which have rather high order and symmetry we will also consider the opposite situation where the order and symmetry are almost absent i.e. amorphous carbon and carbon nanofoams.

While highly symmetric graphene is non magnetic, any feature that breaks its symmetry may introduce magnetic properties. Disordered structures like amorphous carbon, edges and defects where dangling bonds can be localized are the most promising structures for the search of magnetic states, as observed experimentally [2, 3, 4, 5, 6, 7, 8, 9, 10]. The possibility of intrinsic long-range magnetic order in carbon is important

$$\mathbf{a}_1 = r_{cc}(-\frac{\sqrt{3}}{2}, \frac{3}{2})$$

$$\mathbf{a}_2 = r_{cc}(+\frac{\sqrt{3}}{2}, \frac{3}{2})$$

$$\mathbf{R}_A = r_{cc}(0,0)$$

$$\mathbf{R}_B = r_{cc}(0,1)$$

$$r_{cc} = 1.42\text{Å}$$
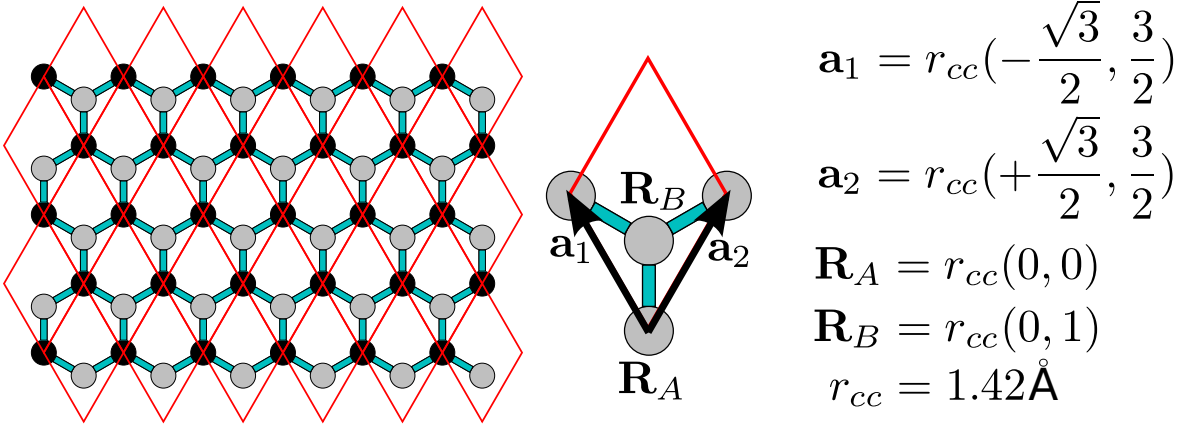
Figure 1.1: 2D honeycomb hexagonal lattice of graphene made of two interpenetrating lattices that make graphene a bipartite structure. Atoms belonging to each sublattice are marked by black and gray balls respectively.

from both fundamental and applied scientific point of view since the properties of $s - p$ electron magnetic materials can be essentially different from those of conventional $d - f$ electron magnetic materials. Following general theoretical consideration [11], the $s - p$ electron magnetic materials may have much higher Curie temperature than conventional magnetic semiconductors making them perspective candidates for new magnetic materials.

1.2   Brief historical and experimental overview

Despite the fact that magnetic phenomena are known to humanity from the time of Greek and Chinese civilizations and magnetism found its application in many things like compass needles, the possibility of magnetic properties of non metallic, carbon based, materials made of light elements was considered in 20-th century only.

The interest in graphite and in its defects under irradiation initiated during world war II because of its importance in nuclear reactors. Since graphite was used to slow down the high energy neutrons to thermal energies in the reactor's active region, the intense irradiation of graphite by neutrons and fissile products formed huge amount of defects in the structure of graphite.

However, possibly because at that time the main priorities were related to the development of nuclear weapons and nuclear energetics, the study of the magnetic properties of graphite and carbon materials was not addressed for many years.

An interest in the magnetic properties of non metallic carbon based materials can be found in works on organic magnets in the late 80's [14, 15, 16]. However the first results had low reproducibility. One of the first well reproducible experimental
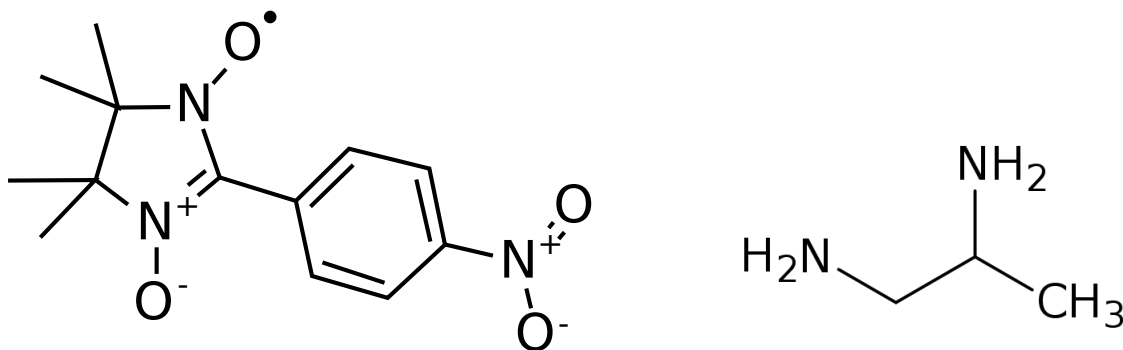
Figure 1.2: Two different compounds used as a starting material to produce organic magnets in Ref. [12] (left: p-nitrophenyl nitronyl nitroxide) and in Ref. [13] (right: 1,2-diaminopropane).

results related to manufacturing of organic magnets based on light elements only was published in Ref. [12] in 1991 where p-nitrophenyl nitronyl nitroxide was used as a starting material (see Fig. 1.2 Left). Also in Ref. [13] in 1992 organic magnets were synthesed based on another compounds (see Fig. 1.2 Right). In this work, the starting material (1,2-diaminopropane) with high ratio of hydrogen to carbon (H/C = 3.3) was heated at 1225K and then pyrolized during 30 minutes. The obtained carbon product was an air-stable material with amorphous-like structure that was readily attracted to a permanent magnet at room temperature and was estimated to have an average saturation magnetization of 0.022 μ_B per carbon atom.
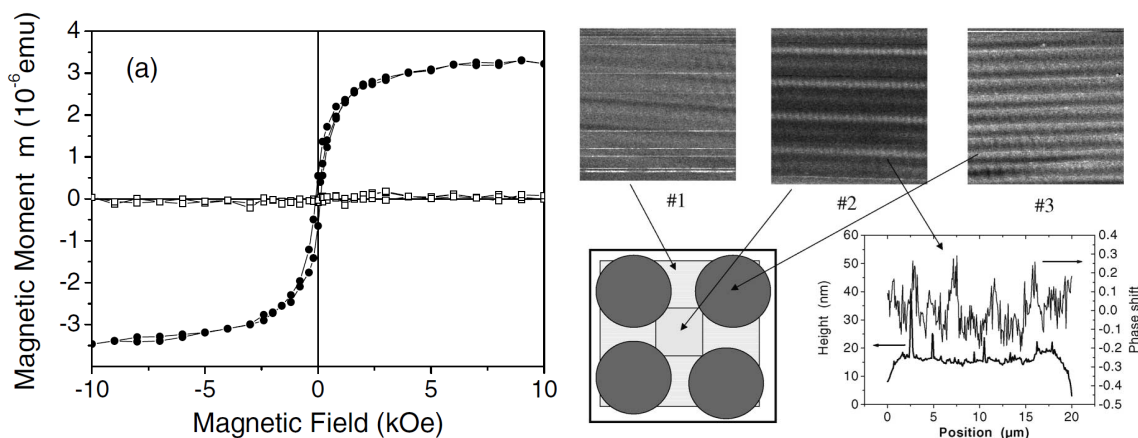
Figure 1.3: Left panel: Magnetic moment measured at T>300 K as a function of the magnetic field, for a HOPG graphite sample before (white point) and after (black points) proton irradiation. Right panel: Top: Phase gradient pictures obtained at room temperature from Magnetic Force Microscopy (MFM) at three surfaces of a sample corresponding to increasing irradiation stages #1, #2, and #3; see sketch at the bottom left of the figure. Bottom right: Topography and phase gradient line scans of the middle MFM picture obtained at stage #2 showing that topography and magnetic signals are not correlated. From [3].

A new page in the history of the magnetic properties of carbon based materials was opened by the discovery of magnetic signals in the bulk phase of rhombohedral C_{60} [17] and later in Refs. [2, 3, 4, 5, 10] in various carbon based materials that were proven to be impurity free within the accuracy of the used techniques. For a review, see [18]. The ferromagnetism in graphitic materials was shown to be closely related to the lattice imperfections as demonstrated by induced magnetism in proton-irradiated highly oriented pyrolytic graphite (HOPG) [3]. In Fig. 1.3 we report their observations showing the appearance of magnetic moments (black points in Fig. 1.3 Left) after proton irradiation and magnetic domains with periodicity depending on the irradiation dose (Fig. 1.3 #1, #2, #3). Beside graphite and polymerised fullerenes, ferromagnetism has been observed in other carbon-based materials such as carbon nanofoam [9], proton irradiated thin carbon films [6] and nitrogen and carbon ion implanted nanodiamonds [7]. All these observations suggest an inherent ferromagnetic behaviour of carbon-based materials. However, the question of the purity of the studied samples from magnetic impurities remains the most critical up to this day. In the recent work [19] it was clearly shown that materials studied in previous experiments, produced by the same manufacturers with the same quality, have small amounts of ferromagnetic impurities distributed as a few micron sized spots over the whole sample and buried under the surface. The chemical decomposition of these spots corresponds to magnetic elements like Fe, Ni, Co and other. At the same time, for impurity free samples only diamagnetic behaviour was observed. The experimental observations are therefore not yet conclusive.

1.3   Computational approach

Throughout this thesis we use the Density Functional Theory (DFT) [20, 21] package SIESTA [22, 23, 24] which implements a localized basis set based on Numerical Atomic Orbitals (NAO) [25] within the Local Density Approximation with Ceperley-Alder parametrization (LDA-CA) [26, 27] and Generalized Gradient Approximations with Perdew-Burke-Ernzerhof exchange model (GGA-PBE) [28]. A detailed description of the Density Functional Theory can be found in [29, 30, 31]. In each chapter we describe the particular implementation most suitable for the studied systems.

Here we briefly describe few aspects related to the selected computational technique. Within LDA-DFT and GGA-DFT the original many-body problem of interacting electrons in a static external potential is reduced to the problem of non-interacting electrons in an effective potential which includes the external potential and the effects of the Coulomb interactions between the electrons, namely the exchange and correlation interactions. This is done by using the one-particle Kohn-Sham equation:

$$\left[-\frac{1}{2}\nabla^2 + V_{eff}(\mathbf{r}) \right] \psi_i(\mathbf{r}) = \epsilon_i \psi_i(\mathbf{r}) \tag{1.1}$$

where the effective single-particle potential can be written as

$$V_{eff}(\mathbf{r}) = V_{ext}(\mathbf{r}) + V_{Hartree}[n] + V_{xc}[n] \tag{1.2}$$

and $n(\mathbf{r})$ is electronic charge density calculated as

$$n(\mathbf{r}) = \sum_i^N |\psi_i(r)|^2 \tag{1.3}$$

where V_{ext} is a static external potential and the second term $V_{Hartree}$ denotes the so-called Hartree term describing the electron-electron Coulomb repulsion. The exchange correlation term V_{xc}, which includes all many-particle interactions, can be found by means of Quantum Monte Carlo simulations for the homogeneous electron gas within the LDA [26, 27]. For the GGA, effects of weak inhomogeneities are additionally taken into account[28]. In general, GGA gives much more accurate results for cohesive energy, equilibrium structure and related characteristics of molecules and crystals. Neither LDA nor GGA, however, can take into account van der Waals interactions which are crucially important to describe the interlayer binding in graphite. As a result, GGA without van der Waals interaction cannot describe the stability of graphite [32] whereas, by chance, due to error cancellation, LDA gives a relatively accurate interlayer distance and binding energy in graphite. Therefore, it is now common practice to use the LDA for calculation of multilayer graphitic systems (see e.g. [33] and references therein).

The next expansion of the eigenstates $\psi_i(\mathbf{r})$ in terms of functions with known properties is used to solve equation (1.1):

$$\psi_i(\mathbf{r}) = \sum_\alpha c_{i\alpha} f_\alpha(\mathbf{r}) \tag{1.4}$$

The set of functions $f_\alpha(\mathbf{r})$ is also known as *basis* and is discussed in the next section.

1.4 Basis set techniques

There are a number of methods of expansion of the eigenvectors, that use different basis functions. As it can be expected, each method has its own benefits and pitfalls. There are three main families of methods depending on the basis sets: atomic sphere methods, plane waves, localized basis sets. The basis functions can be defined either analytically or numerically.

Moreover, there are the so-called all electrons and pseudo-potentials approaches. The first one takes into account all electrons in the atoms while the second one re-

places the core electrons by norm conserving pseudo-potentials and takes into account explicitly only valence electrons.

The first family of methods, i.e. atomic spheres methods which are usually used in all electrons metheods are the most general for precise solutions of the Kohn-Sham equation (1.1). The atomic spheres methods are rather accurate within DFT, asymptotically complete and allow systematic convergence. At the same time such methods have difficulties in the software implementation. They are very expensive from the computational point of view of used resources and cpu time. Beside technical issues, atomic spheres methods give high absolute values of the total energies, so if the differences in relevant energies are small, the calculation must be very well converged.

The next family of methods, i.e. plane wave methods, are widely used among physicists because they are conceptually simple, asymptotically complete, allow systematic convergence and are easy to implement using Fast Fourier Transforms. However the disadvantage of plane wave methods is the representation of localized, atomic wave functions. Tenth of thousands of plane waves per atom or even more depending on the system are required to achieve good accuracy, making the method computationally expensive. Such methods are not suitable for so-called order-N methods, that have linear dependence of computational resources, like memory and cpu time, on the size of the system. In fact, order-N methods are based on locality while the used plane waves are extended over the whole system.

The last family of methods is the localized basis sets that may be based on different types of localized functions such as atomic orbitals:

$$\psi_{Ilmn}(\mathbf{r}) = R_{Iln}(|\mathbf{r}_I|) Y_{lm}\left(\frac{\mathbf{r}_I}{|\mathbf{r}_I|}\right), \tag{1.5}$$

where R_{Iln} is the radial part of the orbital labelled by the index n, l and m define the angular momentum and Y_{lm} are spherical harmonics, $\mathbf{r}_I = \mathbf{r} - \mathbf{Q}_I$ with $\mathbf{Q}_I$ the coordinate of the I-th atom,

The orbital index n gives the possibility of having more than one orbital with the same l and m and therefore the same angular dependence, which is conventionally called a multiple-ζ basis assembled from individual basis functions known as first-ζ, second-ζ, etc.

In the SIESTA package, the radial part of equation (1.5) is represented numerically (numerical atomic orbitals), i.e. it does not have a general analytical form. For a single function, i.e. first-ζ, R_l is found by solving the equation of an isolated pseudoatom

$$\left[-\frac{1}{2r}\frac{d^2}{dr^2}r + \frac{l(l+1)}{2r^2} + V_l^{ps}(r) + V_l^{conf}(r)\right] R_l(r) = \epsilon_l R_l(r) \tag{1.6}$$

where V_l^{ps} is the same pseudopotential for orbital l that will be used for the system of interest and V_l^{conf} is an infinite square well potential of width R_c where R_c is a suitable cut-off. This equation is solved numerically in a logarithmic grid using the Numerov method [34]. The approach described above allows to generate the first-ζ

basis function for each l. A set of single-ζ basis functions forms a so called minimal basis set, which is abbreviated in the SIESTA package as SZ (single-ζ).

The second-ζ basis function $\psi_l^{2\zeta}(r)$ have the same tail as the first-ζ but change to a simple polynomial behaviour inside the "split radius" r_l^s:

$$\psi_l^{2\zeta}(r) = \begin{cases} r^l(a_l - b_l r^2) & \text{if } r < r_l^s, \\ \psi_l^{1\zeta}(r) & \text{if } r \geq r_l^s. \end{cases} \tag{1.7}$$

where a_l and b_l are determined by imposing continuity of the orbital and its first derivative at r_l^s. In Fig.1.4(a),(c) we show the first and second ζ basis functions for the 2s and 2p orbitals of Oxygen [35]. In practice, instead of $\psi^{2\zeta}$ it is more convenient to use the function $\psi^{1\zeta} - \psi^{2\zeta}$, which is zero beyond r_l^s as shown in Fig.1.4(b),(d).
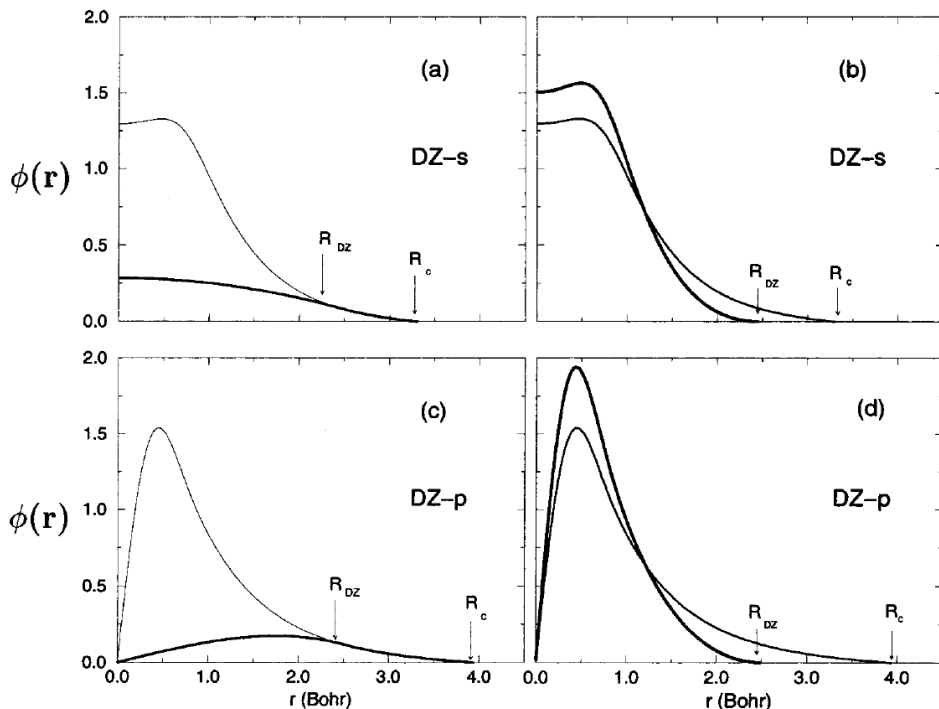
Figure 1.4: First (thin line) and second (thick line) ζ basis functions for the 2s (a) and 2p (c) orbitals of an Oxygen pseudoatom. Here r_l^s is indicated as R_{DZ}. In panels (b) and (d) the second ζ basis function is replaced by the normalized linear combination $\psi^{1\zeta} - \psi^{2\zeta}$. (From [35])

The basis set based on the first-ζ and second-ζ basis functions is called in the SIESTA package as double-ζ and abbreviated as DZ.

To achieve well converged results, in addition to the atomic valence orbitals, it is usually necessary to include also polarization orbitals. The polarization orbitals $\psi_{l+1}(r)$ are obtained from previous-ζ $\psi_l(r)$ by applying a small electric field E and using first-order perturbation theory. The basis set based on the first-ζ, second-ζ

9

and polarization basis functions is called in the SIESTA package as double-ζ plus polarization and abbreviated as DZP.

In general, methods based on localized basis sets are rather efficient in implementation, relatively cheap from a computational point of view, since their locality is suitable for order-N methods. Moreover they have a direct physical interpretation as atomic wave functions. However, the typical localized basis sets methods have difficulties in systematic convergence of wave functions that require a preliminary validation of the parameters controlling the convergence procedure. Usually the basis set have to be prepared and tested for different systems before calculations. Such tests are available to the community of SIESTA users. As it was said in the beginning of this section we use an implementation of localized basis set based on atomic orbitals because, besides the advantages listed before, the method is conceptually suitable to describe defects and finite systems. This is a balanced solution from the point of view of computational resources like time and memory and accuracy of calculations, that allows us to use this technique to perform massive numerical study of magnetic properties in disordered carbon structures based on rather expensive generate and test approaches.

1.5 Spin polarized calculations

In the case of spin polarized calculation with collinear spins, the Kohn-Sham equation (1.1) can be rewritten in terms of spin up and spin down orbitals $\psi_i^+(\mathbf{r})$ and $\psi_i^-(\mathbf{r})$ as

$$\left[-\frac{1}{2}\nabla^2 + V_{eff}^\pm(\mathbf{r}) \right] \psi_i^\pm(\mathbf{r}) = \epsilon_i^\pm \psi_i^\pm(\mathbf{r}) \tag{1.8}$$

which introduces two sets of values for $n(\mathbf{r})$ and $V_{eff}(\mathbf{r})$, one for spin up and another for spin down. Thus, the calculations can be repeated twice in an almost independent way separately for each spin component, because only the term $V_{xc}(\mathbf{r})$ in V_{eff} depends simultaneously on the two spin components.

The values

$$n^+(\mathbf{r}) = \sum_i^N |\psi_i^+(r)|^2 \quad and \quad n^-(\mathbf{r}) = \sum_i^N |\psi_i^-(r)|^2 \tag{1.9}$$

represent electronic charges for spin up and spin down orbitals respectively and

$$m(\mathbf{r}) = n^+(\mathbf{r}) - n^-(\mathbf{r}) \tag{1.10}$$

represents the 3D spin density or magnetisation.

At the same time, by means of the decomposition of the eigenstates $\psi_i(\mathbf{r})$ over the atomic basis functions implemented in the SIESTA package, it is possible to express

the spin polarization s_i (also called atomic magnetisation) separately for each atom with index i in terms of the atomic charges $q_i^+ \equiv q_i^{up}$ and $q_i^- \equiv q_i^{down}$ as

$$s_i = q_i^+ - q_i^- \tag{1.11}$$

We note that the use of a localized basis gives the possibility to extract the atomic spin polarizations s_i based on the values q_i^+ and q_i^- which can be taken directly from the SIESTA output. While the file with $n^\pm(\mathbf{r})$ usually has a size of few megabytes, the data related to $q_i^\pm$ is just a table of size equal to the number of atoms in the system. For example in Figs. 3.9, 3.10, 3.11 the visualisation of atomic magnetisation is done by means of the $q_i^\pm$ taken directly from the SIESTA package output.

In case of spin polarized calculations, the values $n^+(\mathbf{r})$, $n^-(\mathbf{r})$, q_i^+, q_i^- can be found in the SIESTA output. Since $n^\pm(\mathbf{r})$ are saved as 3D arrays of values on a grid in real space, we can convert such data to the file format directly suitable for visualisation using the VESTA program [36]. The visualisation of 3D data is given as iso-surface plots, where the predefined value c:

$$\min_{\mathbf{r}} m(\mathbf{r}) < c < \max_{\mathbf{r}} m(\mathbf{r}) \tag{1.12}$$

is used to produce the surface of constant magnetisation, i.e. the solution of equation

$$m(\mathbf{r}) = c \tag{1.13}$$

Examples of visualisations made by means of the VESTA program according to the above described procedure can be found in Figs. 3.9, 3.10, 4.1, 5.2, 5.6, 5.9, 5.10, 5.11, 5.12.

1.6 Burgers vector and Frank equation of large angle grain boundaries

In 1926, Frenkel estimated the theoretical yield stress of a crystal as about 10% of the Young's modulus [37], a value which is 3 order of magnitude larger than observed experimentally. Several years later, in 1934 Orovan [38], Tailor [39] and Polanyi [40] realized that Frenkel estimate for ideal crystals was not representative since the real carriers of large deformations in solids are linear topological defects, called *dislocations*. As shown later by Peierls [41] and Nabarro [42] this result solved the contradiction discovered by Frenkel.

The simplest example of dislocation in a crystalline lattice is a defect made by insertion of a half of atomic plane. Such defect, known as *edge dislocation*, is shown in Fig. 1.5a, where the glide plane is indicated by a dashed line.

a)

b)
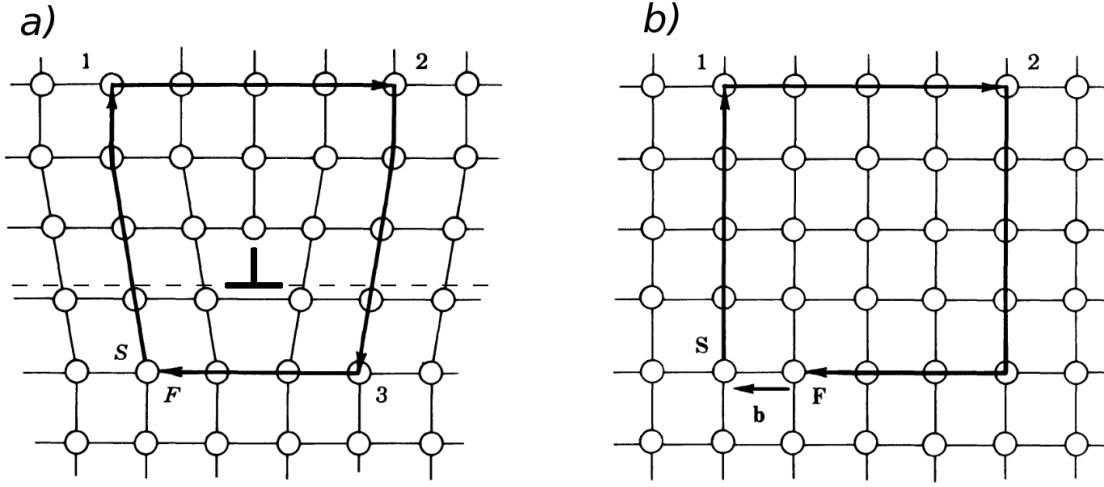
Figure 1.5: (a) Edge dislocation in a simple cubic lattice with Burgers circuits and (b) a perfect reference crystal. The glide plane is shown by a dashed line in (a). Adapted from [43] page 22.

To describe the dislocation as a topological defect, Burgers introduced an important quantity now known as *Burgers vector*. Following Frank [44] we define the Burgers vector as described below.

First we form a closed, clockwise *Burgers circuit S-1-2-3-F*, contour around the dislocation line and far enough from it (Fig. 1.5a). Then, we draw the same circuit in the perfect reference lattice, as shown in Fig. 1.5b. The vector required to close the lattice circuit, drawn from finish F to start S in Fig. 1.5b, is the *Burgers vector* $\mathbf{b}$ of the dislocation. The symbol adopted to represent a general dislocation is $\perp$.

a)

b)
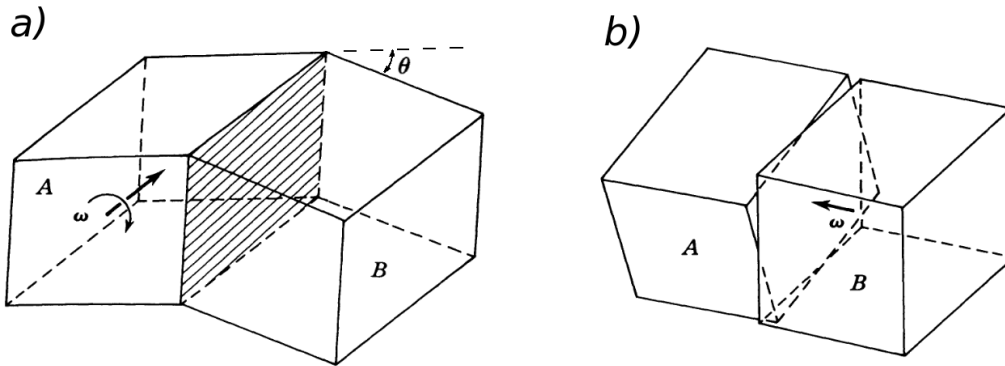
Figure 1.6: (a) Tilt grain boundary (a) between two grains A and B misoriented with tilt angle θ, defined by rotation vector ω which belongs to the plane of the grain boundary. (b) Twist grain boundary where the rotation vector ω is normal to the boundary plane. Adapted from [43] page 704.

Dislocations are topological defects related to long-range translational order. There is also another type of linear topological defects, i.e. topological defects related to long

range orientational order known as *disclinations*. The angular deficit and rotation of the defect can be represented by the *Frank vector*. For instance, in the honeycomb lattice, elementary disclinations are created by pentagons or heptagons. For a pentagon, the angle deficit is 360°/5-60° = 12° and the direction of the Frank vector is orthogonal to the plane of honeycomb lattice. Free disclinations never occur in bulk materials since they have energy quickly increasing with sample size. Nevertheless, they can be considered as building blocks for the construction of other defects. For example, a dislocation can be represented as a *disclination dipole*, namely a pair of disclinations with equal and opposite Frank vectors and distance R (*dipole arm*) from each other. For example an edge dislocation in the honeycomb lattice can be constructed from a pentagon-heptagon pair, as shown in Fig. 1.7.
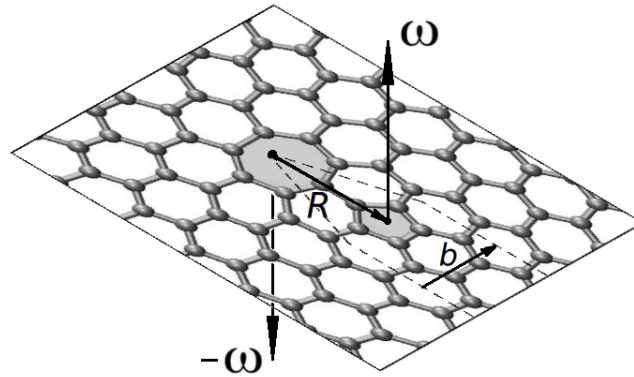
Figure 1.7: 57-dislocation represented as a disclination dipole made of two 5- and 7-fold rings, see text, where ω is the Frank vector. The vector R represents the dipole arm and the Burgers vector $b = \omega \times R$. Adapted from [45].

Dislocations are important not only to understand the mechanical properties of solids but also their crystalline structure. X-ray diffraction shows that most real crystals have multigrain structure. The interface where two single crystals A and B of different orientations (see Fig. 1.6) join each other is called *grain boundary*.

If grain B can be brought into the same orientation as grain A by a rotation ω, then the vector ω defines the rotation axis and the misorientaion or *tilt angle θ*. The vector ω is nothing but the Frank vector for the grain boundary. If ω lies in the plane of the grain boundary, the grain boundary is called a *pure tilt grain boundary* (Fig 1.6a), while if ω is perpendicular to the grain boundary plane, it is a *pure twist grain boundary* (Fig 1.6b). In general, a grain boundary has a mixed character, containing both tilt and twist components.

To get basic geometric relations for grain boundaries, let us consider a simple cubic crystal with the grain boundary in a symmetrical positions with respect to the (100) planes of the two grains and with rotation axis parallel to [001]. Then the simplest grain boundary with low energy is a tilt grain boundary composed as an array of elementary edge dislocations with Burgers vector **b**, tilt angle θ and separation D. (see Fig 1.8a).
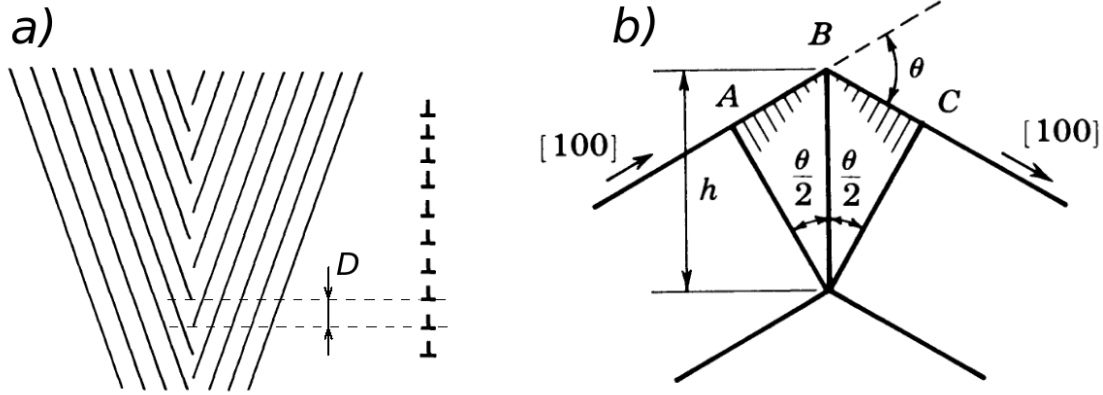
Figure 1.8: Symmetric (100) tilt grain boundary with misorientation angle θ in a simple cubic crystal composed as an array of elementary edge dislocations. Only the extra atomic planes are shown (a) with mean separation between dislocations D and corresponding geometrical scheme (b) where h is an arbitrary large enough segment of grain boundary. Adapted from [43] pages 704-705.
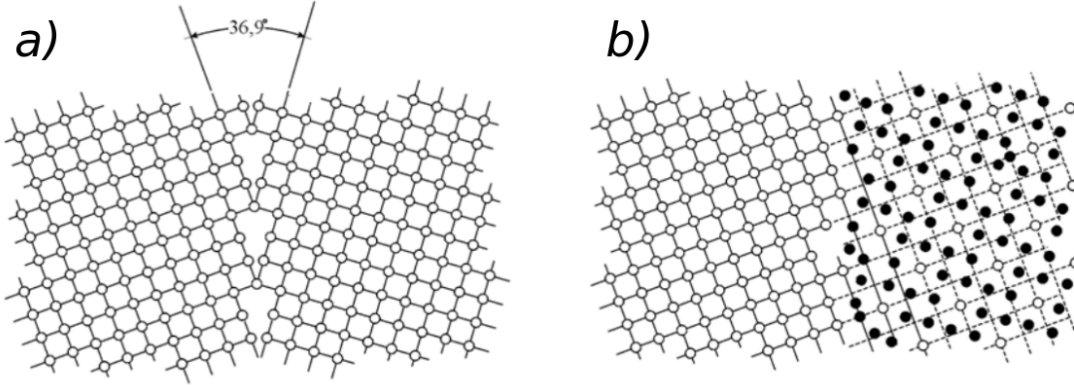
Figure 1.9: Large angle grain boundary with misorientation angle $\theta = 36.9°$ in simple cubic crystal (a). For this specific tilt angle, few atoms from both grains occupy positions which are common for both grains (b). Such atoms are shown by white balls in the right grain. As a result, such grain boundaries are called special grain boundary which can be described by Coincidence Site Lattice (CSL) [46] as opposed to all other grain boundaries called general grain boundaries (Adapted from [47] section 3.3.4).

From Fig. 1.8b the number n_p of half planes introduced when we described the dislocation (see Fig. 1.5a) is

$$n_p = \frac{AB + BC}{b} \tag{1.14}$$

Since

$$AB = BC = h\sin(\theta/2) \tag{1.15}$$

14

where h is an arbitrary large enough segment of grain boundary, then

$$n_p = \frac{2h}{b}\sin(\theta/2) \tag{1.16}$$

and the mean separation between dislocations in the grain boundary is

$$D = \frac{h}{n_p} = \frac{b}{2\sin(\theta/2)} \tag{1.17}$$

If the misorientation angle between neighbouring grains is rather small (5-10°), then such grain boundaries are called low angle grain boundaries. In this case equation (1.17) can be simplified as

$$D \approx \frac{b}{\theta} \tag{1.18}$$

If the misorientation angle is greater than 10°, then such grain boundaries are called large angle grain boundaries (see Fig. 1.9).

The equation (1.17) rewritten in the form

$$b = 2D\sin(\theta/2) \tag{1.19}$$

constitutes the particular case of Frank's equation (see [43] page 707-708) which we use in our work related to the study of grain boundaries with dangling bonds in chapter 3.

Chapter 2

Mechanism and free-energy barrier of the type-57 reconstruction of the zigzag edge of graphene

Recent *ab initio* calculations without spin [P. Koskinen et al., Phys. Rev. Lett. **101**, 115502 (2008)] predict that the zigzag edges of graphene should be reconstructed, albeit with an energy barrier to be overcome. After verifying that spin-polarized calculations give qualitatively the same result, we study the mechanism and the free-energy of the reconstruction of the zigzag edges from a periodic hexagon structure (zz) to an alternate pentagon-heptagon structure [zz(57)] using the empirical LCBOPII-potential. The zz(57) edges are stabilized by an almost triple bond similar to those of the armchair edges and we propose a way to account for this quantum mechanical effect in the empirical long-range carbon bond order potential II (LCBOPII). Aside from that, the reconstructed edge is flat as a result of tensile edge stress. The reconstruction occurs spontaneously in molecular dynamics simulations at high temperature, leading to the identification of a reaction coordinate for the reconstruction that allows us to calculate the free-energy barrier by using Monte Carlo simulations and umbrella sampling. At room temperature we find a free-energy barrier of 0.83 eV for the first transformations of two hexagons to a pentagon-heptagon pair that is higher than the one for a fully reconstructed edge and increasing with temperature.

2.1 Introduction

The macroscopic properties of any material depend strongly upon the microscopic structure. In graphene nanoribbons (GNRs) [48] (small stripes of graphene [1]), the edges play an important role because of the relatively large fraction of atoms situated at, or near, the edge. The band structure of GNRs differs substantially from that of bulk graphene, and, depending on width [49, 50] and edge type (zigzag or armchair), it can be either metallic or semiconducting [51, 48, 52], the latter with great potential for applications in electronics [53, 54]. The zigzag termination is the most-studied edge in theoretical studies of transport in GNRs because it allows a simple definition of boundary conditions, decoupling the two sublattices of the hexagonal crystal [55]. In these calculations, it is assumed that the atoms at the edges are saturated by hydrogen so that the band structure can be studied only in terms of the π band, neglecting the lower σ bands.

However, the situation might be more complicated than this. In fact, recent *ab initio* calculations by Koskinen *et al.* [56], based on the Density Functional Theory (DFT), have found that the reconstruction of the zigzag edge (zz) to a structure with alternating pentagons and heptagons, hereafter called zz(57), leads to a lower edge energy and to a self-passivating edge that would not bind hydrogen atoms and may be identifiable trough coherent electron focusing experiments [57]. Aside from that, the authors predict the zz(57) structure to have an edge energy also slightly lower than that of the armchair (ac) edge (see Fig. 2.1 for an illustration of these edge structures). While the theoretical stability of this zz(57) edge is still a topic of debate, primarily due to the influence of hydrogen pressure in realistic systems [58, 59, 60], several recent transmission electron microscopy experiments [61, 62, 63] have reported the experimental observation of a partially reconstructed zz edge. Furthermore, the semiconducting nature of this edge state may be a possible explanation as to why experimentally fabricated GNRs are predominantly semiconducting [64]. Since it has been shown theoretically that the zz edges are magnetic [51, 53], as a first step, we have verified using DFT [20, 21], as implemented in the SIESTA code [22], that the zz(57) edge is favoured over zz and ac edges also when spin polarization is taken into account.

In this chapter, we study the path and free-energy barriers for the zz to zz(57) edge reconstruction by means of Monte Carlo (MC) and Molecular Dynamics (MD) simulations based on the empirical long-range carbon bond order potential II (LCBOPII) [65]. The computational efficiency of this potential allows us to study not only the $T = 0$ K equilibrium structure of a fully reconstructed edge, but also to follow, for large samples and finite temperature, the path of reconstruction and to calculate the free-energy barrier for it. We find that the free-energy barrier for the reconstruction of a whole edge displays an unusual nonmonotonic trend, increasing up to about 700 K and slowly decreasing at higher temperatures. At room temperature, we find an energy barrier of 0.7 eV, in good agreement with the value of 0.6 eV found with DFT

at $T = 0$ K [56]. However, we find that the first step of the reconstruction, namely, the transformation of a single pair of hexagons into a pentagon-heptagon pair, has a higher free-energy barrier of 0.83 eV at room temperature, increasing to ~ 1 eV above 500 K; therefore, it is this barrier that determines the escape rate. The reconstruction of this edge will most likely happen in a sequence of transformations since successive transformations next to already existing pentagon-heptagon pairs are significantly easier, as we will show.

To be able to describe correctly the edge reconstruction, we have slightly modified the bond order potential LCBOPII. According to DFT calculations [56], the zz(57) and ac edges have a strong, almost triple, bond at the edges that stabilizes these two structures with respect to the zz that has graphitic bonds. The strong character of this bond is not predicted by the original version of the LCBOPII potential [65]. In fact, the conjugation term in the potential assumes that the electrons available for π bond formation are equally shared among the bonds with undercoordinated neighbours. As a consequence, the edge bond (marked by a thick red line in Fig. 2.1) is assigned as a double bond, in disagreement with the DFT result [56]. It is, however, possible to modify the LCBOPII conjugation term in such a way that it gives the proper bond character without loss of computational efficiency. This is explained in detail in the Appendix.

The chapter is organized as follows. In Sec. 2.2, we show the structure and energetics at $T = 0$ K in comparison to the DFT results of Ref. [56] and to our own *ab initio* calculations done with the SIESTA package [22], the latter with and without taking into account spin polarization. In Sec. 2.3, we derive a reaction coordinate for the transition from zz to zz(57) based on the results of MD simulations. In Sec. 2.4, we determine the free-energy barrier of the transformation of a full edge and of successive transformations of single pairs of hexagons to heptagon-pentagon pairs as a function of temperature. Sec. 2.5 contains the summary and conclusions.

2.2 $T = 0$ **K structure and energetics**

In Fig. 2.1, we show the zz, zz(57), and ac edge terminations. *Ab initio DFT* calculations [56] predict that the most stable edge of graphene is the zz(57), which can be considered as a reconstruction of the (metastable) zz edge. The zz(57) is also slightly favoured over the ac edge.

Before addressing temperature-dependent properties, we have to verify that the empirical potential LCBOPII gives the correct behaviour of graphene edges at $T = 0$ K. The crucial feature is the armrest bond of zz(57), where, according to the DFT calculations of Ref. [56], the bond length decreases to 1.24 Å, a length slightly longer but comparable to that of a triple bond, which is 1.20 Å. This fact makes the bond self-passivating because there are no more dangling bonds, as is the case for the zz edge. This feature is not reproduced by the original version of LCBOPII [65] and,
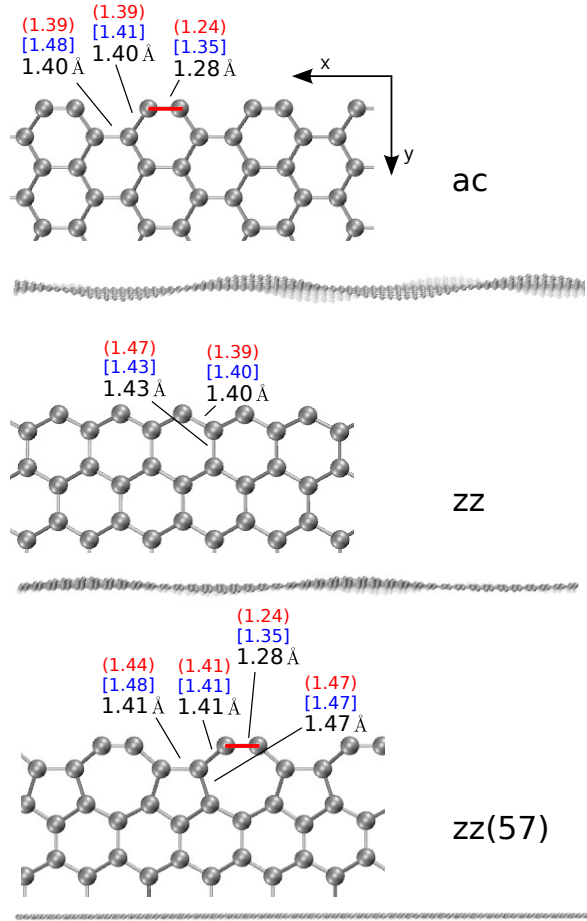
Figure 2.1: Top and lateral view of the equilibrium structure of (from top to bottom) ac, zz and zz(57) edges obtained with the improved LCBOPII potential used in this work with values of interatomic distances at the edge. For comparison, the DFT values [56] are given in round parentheses and those given by the original LCBOPII[65] are given in square parentheses.

therefore, we have devised a simple modification described in the Appendix that allows us to capture this feature correctly. It should be noted that the situation at the zz(57) and ac edges, with a bond between two twofold-coordinated atoms, is not common. The modification used here and described in the Appendix changes only this situation, while keeping the description of all other bonding configurations equal, and, therefore, does not affect the zz-edge.

Following Koskinen et al. [56], we define the edge energy as

$$\epsilon_{\text{edge}} = \frac{E - N\epsilon_{\text{bulk}}}{2L} \tag{2.1}$$

where N is the number of carbon atoms, E is the total energy of the sample, ϵ_{bulk} is the bulk energy per particle, L is the length of the edge and the factor 2 accounts for

the two edges of the sample. The energy difference between the zz and zz(57) is

$$\Delta\epsilon = (\epsilon_{\text{edge}}^{\text{zz}} - \epsilon_{\text{edge}}^{\text{zz}(57)}) \tag{2.2}$$

For a detailed comparison between the results of LCBOPII with those obtained by DFT, we have performed DFT calculations of the edge energy and equilibrium structure by means of the package SIESTA [22], that implements DFT on a localized basis set. We used the generalized gradient approximation with Perdew-Burke-Ernzerhof parametrization (GGA-PBE) [28] and did the calculations with and without taking into account spin polarization (SP), hereafter indicated as SP-SIESTA and SIESTA. A standard built-in double-ζ polarized (DZP) [25] basis set was used for all calculations. The cutoff radii of the atomic orbitals were obtained from an energy shift equal to 1.0 mRy. The real-space grid is equivalent to a plane-wave cutoff energy of 360 Ry. For all nonperiodical directions, an extra space larger than 15 Å was added to avoid spurious interactions. We used 50 k points for sampling the Brillouin zone. The geometry was relaxed using the conjugate gradient method until all forces were smaller than 0.02 eV/Å. In agreement with Ref.[56], we find that, for samples with a periodically repeated minimal unit cell in the x direction, the edge energy becomes constant for ribbon widths $\gtrsim 50$ Å.

Next, we calculate the edge energy by MC simulations with LCBOPII for a sample 50 Å wide, for which the edge energy is converged in the DFT calculations. In the x direction, we take a periodically repeated cell of length $L_x = 114$ Å. We equilibrate the samples by performing MC simulations while lowering the temperature in steps from 100 K to 0.1 K.

In Table 2.1, we compare the edge energies obtained by the different methods. Our DFT calculations with SIESTA give a value $\Delta\epsilon = 0.33$ eV/Å very close to the DFT value $\Delta\epsilon = 0.35$ eV/Å of Ref. [56]. Including spin polarization in SIESTA gives the same qualitative result, favouring zz(57), although with a significantly smaller energy gain $\Delta\epsilon = 0.13$ eV/Å.

In the original LCBOPII-potential [65], $\Delta\epsilon = -0.02$ eV/Å (favouring the zz-state). The modified potential (see Appendix) gives $\Delta\epsilon = 0.24$ eV/Å in qualitative agreement with the DFT results and in-between the values with and without SP.

In Fig. 2.1, we show the top and side views of the equilibrium edge structures and bond lengths found by DFT [56] and by the original and modified LCBOPII. Note that the LCBOPII calculations allow out-of-plain relaxation that is neither included in Ref. [56] nor in our own DFT results due to the choice of a minimal cell in the periodic x direction. The modified LCBOPII gives a bond length of the armrest of the zz(57) and ac edges of 1.28 Å, which is close to the 1.24 Å found by DFT. Furthermore, we note that the zz and ac edges are undulated in the out-of-plane direction, whereas the reconstructed zz(57) is completely flat. One possible reason is that the atoms at the edge favor a slightly different periodicity than the bulk one. Since the bulk size is fixed for wide enough samples, this will result in an edge stress. From Fig. 2.2, we can see that the equilibrium length of the unit cell in the periodic x direction of GNRs with

zz(57) edges calculated by SIESTA is slightly smaller than the bulk value, whereas for zz and ac, it is larger than the bulk value. As a consequence, zz(57) edges are subjected to tensile stress, while zz and ac are subjected to compressive stress that leads to out-of-plane distortion at the edges. The side views shown in Fig. 2.1 calculated by LCBOPII display exactly this behaviour. These features match the description of the edge elastic properties described in Ref. [66].
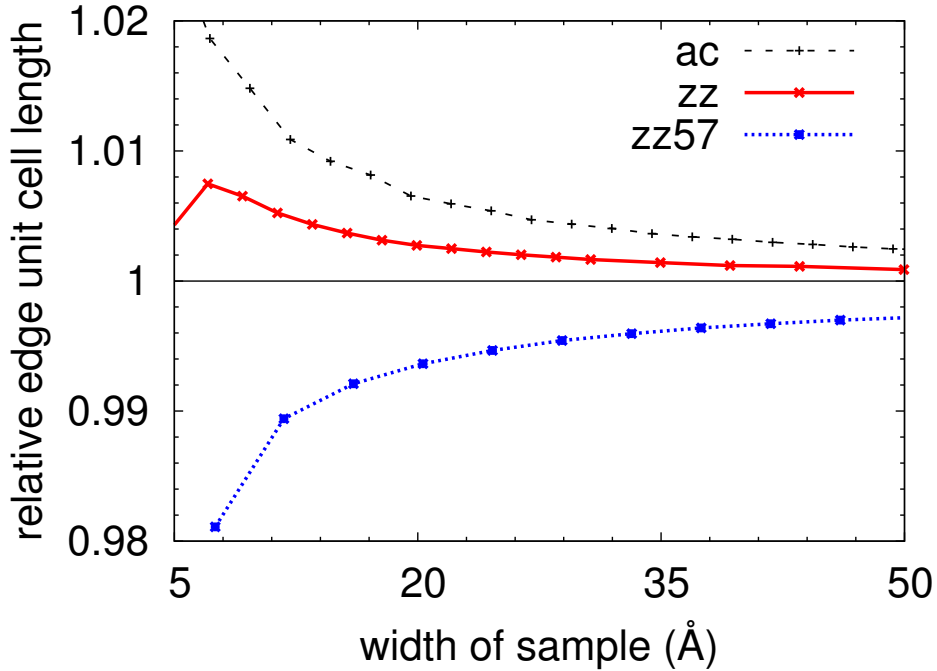
Figure 2.2: Equilibrium length in the periodic x direction of the unit cell divided by the bulk value as a function of the width of the sample for ac, zz and zz(57) edges found using SIESTA. The zz and ac cells are larger than the bulk value (straight line) causing edge stress that would result in (out-of-plane) buckling of the edge. The zz(57) cell is smaller than the bulk and subjected to tensile stress favouring a flat geometry.

2.3 Transition mechanism

Next, we employed MD[67] to examine the transition of the graphene edge from zz to zz(57). The MD simulation gives an insight into the dynamics of the transition. The simulation was done in the microcanonical (NVE) ensemble with time steps of 0.5 fs. The sample shown in the top panel of Fig. 2.3 is finite in all directions (no periodic boundary conditions). The temperature was equilibrated to approximately 1500 K, where the transition was found to take place within timescales of the order of picoseconds.

	LCBOPII	Modified LCBOPII	SIESTA	SP-SIESTA	DFT [56]
zz	1.05	1.05	1.34	1.15	1.31
ac	1.04	0.75	1.02	1.02	0.98
zz(57)	1.06	0.81	0.98	0.98	0.96

Table 2.1: Edge energy ϵ_{edge} in eV/Å obtained by (from left to right) the original LCBOPII [65], LCBOPII with the modification described in the Appendix, the DFT package SIESTA[22] without and with spin-polarization, and by DFT in Ref. [56] without spin-polarization. Note that the modified LCBOPII stabilizes also the ac edge that becomes slightly more favourable than the zz(57), at variance with the DFT results.

In Fig. 2.3, we show three snapshots during the transition of two hexagons at the zz edge to one pentagon-heptagon pair at the reconstructed edge. We see that, as the transition evolves, the distances r_{AB} and r_{AC} approximately interchange values, so that the nearest neighbours A and B become next nearest neighbors and the opposite for A and C. Based on this finding, we define a reaction coordinate d, as

$$d = \frac{r_{AB} - r_{57}}{r_{zz} - r_{57}}, \tag{2.3}$$

where $r_{zz} = 2.42$ Å and $r_{57} = 1.47$ Å are the equilibrium values at $T = 0$ K of r_{AB} for zz and zz(57), respectively. The identification of a reaction coordinate allows us to evaluate the free-energy barrier as described in details in Sec. 2.4.

For reference, we first compared the (free-) energy barrier at $T = 0$ K according to LCBOPII with that according to SIESTA and SP-SIESTA for a reaction path obtained by linear interpolation (in 129 steps) of all atomic positions from the zz to the zz(57) configuration for a sample 16 Å wide containing 32 atoms. The minimal energy configurations of the used initial zz-terminated and final zz(57)-terminated states were obtained with SIESTA. The energy barrier shown in Fig. 2.4, that does not include any further relaxation, represents an upper bound to the actual energy barrier. As a matter of fact, these values are about a factor 5 larger than those found with relaxation, as shown in Section 2.4, and are only meant to compare LCBOPII to SIESTA for a given fixed reaction path. The kink in the SP-SIESTA curve at $d \simeq 0.285$ marks the crossing of the energy curves from the non-SP and SP calculations, the one with the lowest energy being drawn here. The energy barrier according to LCBOPII is similar to that of SIESTA and SP-SIESTA, but LCBOPII gives a lower edge energy for both the zz and the zz(57). This fact can be partially explained by the too high cohesive energies of the DFT methods. For example, SIESTA gives 7.90 eV for bulk graphene, against the experimental value of 7.35 eV given by LCBOPII.
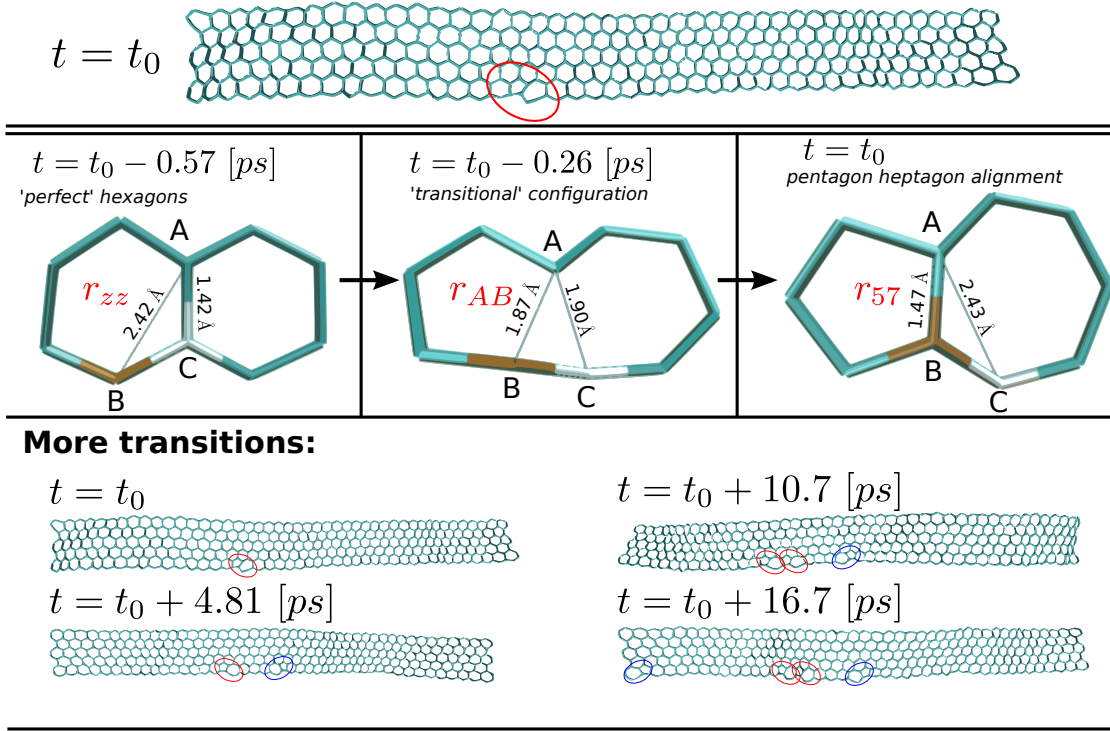
Figure 2.3: Top panel: Sample with one spontaneously reconstructed zz(57) cell. Middle panel: The first transition (at time $t = t_0$) is displayed in detail for different time frames, going from zz (upper left corner) to zz(57). This simulation was done at $\sim 1500\,\mathrm{K}$, in the NVE ensemble. Bottom panel: Successive transitions are shown where blue (right-oriented oval) and red represent the mirrored symmetric transitions.

2.4   Free-energy barrier

In this section, we study the free-energy barrier for the zz to zz(57) transition, which requires us to study unit cells with two hexagons that transform into one pentagon-heptagon pair. Therefore, from now on, all energies are given per unit cell (4.94 Å) rather than in eV/Å as done previously.

The energy barrier between zz and zz(57) states, ~ 0.6 eV per edge unit cell according to Ref. [56], is extremely difficult to overcome by thermal fluctuations at low temperatures (below approximately 1500 K) within computationally accessible time scales. An established technique to study this type of rare events computationally is the so called umbrella sampling method (see, e.g., [68], p. 168). The method is illustrated in Fig. 2.5. We first divide the reaction coordinate interval $[0, 1]$ into n equal parts (called windows) labelled by $i \in \{1, 2, \ldots, n\}$, where n is chosen such that the maximum energy change in one window is of the order of the thermal energy. We then perform n distinct MC simulations, where the modified LCBOPII potential $U_{LCBOPII}$
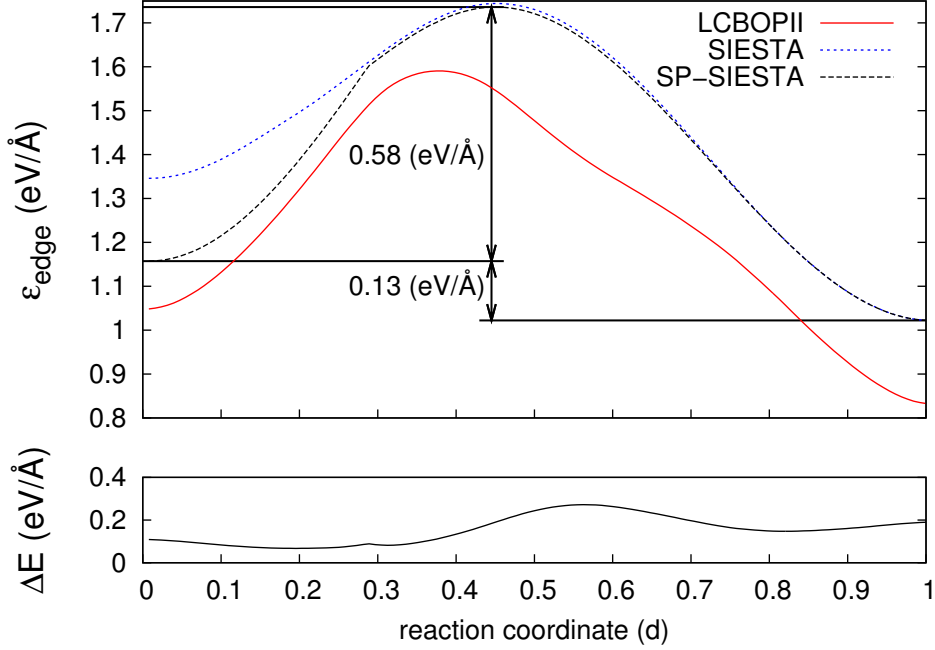
Figure 2.4: Top: Comparison between SIESTA (dotted blue line), SP-SIESTA (dashed black line) and the modified LCBOPII (solid red line) for the energy barrier from the zz-state ($d = 0$) to the zz(57) state ($d = 1$) of a sample 16 Å wide. The intermediate configurations are calculated by linearly interpolating the coordinates of the initial zz and final zz(57) state equilibrated in SP-SIESTA in 129 steps. This gives an upper bound to the energy barrier of 0.58 eV/Å (0.52 eV/Å) for SP-SIESTA (LCBOPII). Bottom: Difference ΔE between the energy barrier calculated by SP-SIESTA and the one calculated by the modified LCBOPII.

is replaced by

$$U = \begin{cases} U_{LCBOPII} & \text{if } d \text{ in window } i \\ \infty & \text{else} \end{cases} \qquad (2.4)$$

so that all MC moves outside the i-th umbrella window will be rejected. Second, by further dividing each windows in m subintervals (bins), we calculate the binned probability density $P_{i,j}$ for bin j in window i, where $j \in \{0, 1, \ldots, m\}$ (typically $m = 10$). Next, we can calculate the free-energy up to an additive constant within each window for each bin as $F_{i,j} = -k_B T \log(P_{i,j})$, where k_B is the Boltzmann constant. By assuming that the free-energy is continuous along the reaction path, the first (n-1) additive constants can be found by linear extrapolation of the last two binned points to match the first point in the next window. The last additive constant is chosen to set the free-energy of zz to zero.

In Fig. 2.6(a), we show the temperature dependence of the free-energy along the transition path for a sample with two fully reconstructed edges. We find that the free-energy barrier $F_b = F_{max} - F_{zz}$ is nonmonotonic, growing to 700K and decreasing at higher temperature, as shown Fig. 2.6(b). The energy barrier at $T = 0$ K, estimated by extrapolation, is approximately equal to 0.7 eV per edge unit cell, close to the value
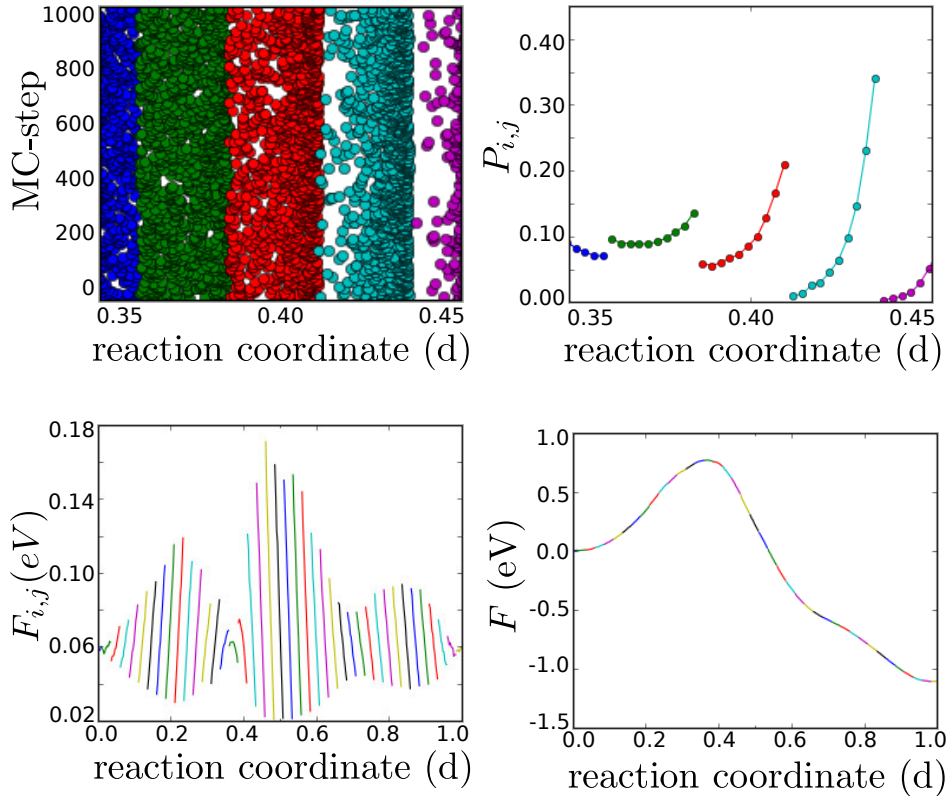
Figure 2.5: Four stages of umbrella sampling. From left to right, top to bottom: first 1000 sampling points for several windows 0.025 wide; probability $P_{i,j}$; relative free-energy, $F_{i,j} = -kT \log(P_{i,j})$; free-energy shifted by assuming continuity. Different colours are used to separate the windows.

0.6 eV obtained with the nudged elastic band method in Ref. [56]. It is interesting to compare this behaviour with that found for the initial step of the reconstruction, namely the transformation of a single pair of hexagons into a pentagon-heptagon pair. The comparison to the one calculated for fully reconstructed edges in Fig. 2.6(b) shows that the free-energy barrier for the first transformation is definitely higher than that for a full reconstruction, it grows more rapidly with temperature, and does not decrease up to 1000 K. This is almost the highest temperature we can study because, above the temperature where the transition occurs spontaneously, the umbrella sampling of single transformations can not be performed because transitions will occur spontaneously at other places.

Next we calculate the free-energy barrier for successive transformations of hexagon pairs. Our sample consists of 16 zz edge unit cells (8 pairs of hexagons) in the periodic x direction. To name different single transitions, we use an 8-digit code consisting of the numbers 0 (two hexagons), 1 (pentagon-heptagon pair) and 2 (transition from 0 to 1). The free-energy barrier of the successive transitions at $T = 300$ K are shown in Fig. 2.7 (the same simulation was performed at $T = 1000$ K). This shows that the
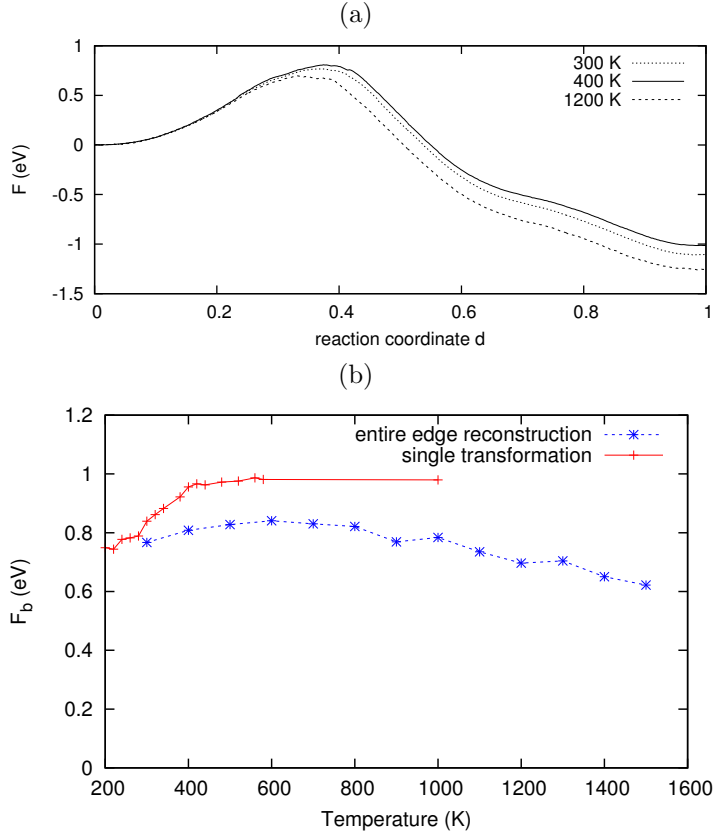
Figure 2.6: a) Free-energy per edge unit cell for different temperatures as a function of the reaction coordinate for the reconstructions of a whole edge. b) Comparison of the temperature dependence of the free-energy barrier for the reconstruction of a whole edge (*, blue) with the free-energy barrier for the transformation of a single unit cell (+, red).

free-energy barrier to create the first step of the reconstruction (20000000) is the most difficult [$F_b \approx 0.83$ (0.98) eV at 300 (1000) K]. All following transitions (12000000, 11200000, ...) are progressively easier [$F_b \approx 0.71 - 0.59$ (0.79 − 0.69) eV] and the last reconstruction (11111112) is the easiest [$F_b \approx 0.47$ (0.57) eV].

Based on these result we can now calculate a typical transition time for the first reconstruction (20000000).

2.4.1 Transition time

For a single transition, we can use transition state theory [69] to find a typical escape time τ_e for the system to go from one locally stable state (A) to another (B). In our case, the states represent, respectively, a zz sample (00000000) and the same sample with one heptagon-pentagon pair (10000000). The typical decay time from an
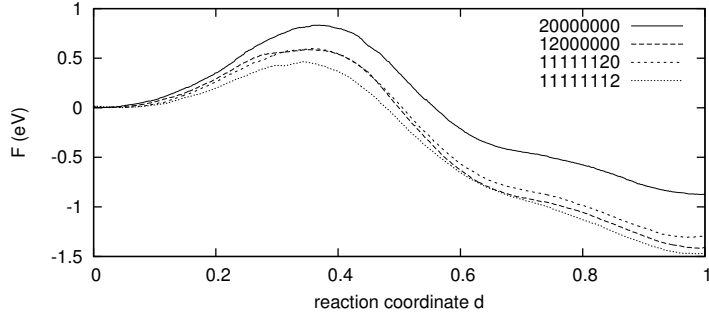
Figure 2.7: Free-energy per edge unit cell for successive transitions of a single pair of hexagons to a pentagon-heptagon pair as a function of the reaction coordinate. 0 means two zigzag cells at the edge, 1 means a (reconstructed) zz(57) cell, and 2 means the transition from zz to zz(57). The zero-energy point is chosen for convenience at the zz-state.

energy minimum is given by

$$\tau_s \sim M^{1/2} \left[\frac{d^2U}{dr^2} \right]_{r=r_a}^{-1/2},$$

where r_a is the equilibrium position of the system in state A and M is the mass of the particle escaping from the potential well that we take as the mass of a carbon atom. Fitting the free-energy near the minimum at zz gives $\tau_s \approx 3.4 \cdot 10^{-14}$ s. Then, an estimate of the timescale in which the system goes from A to B, the escape time, is given by $\tau_e \sim \tau_s \exp(F_b/E_{\text{noise}})$. We assume that E_{noise} can be approximated by the thermal energy $E_{\text{noise}} = k_B T$. At room temperature, with $F_b = 0.83$ eV, this gives a typical escape time of $\tau_e \approx 9$ s decreasing to ≈ 2 ps at $T = 1000$ K where $F_b \approx 1$ eV. This will result in blurred images in electron microscopy because the edge can switch between the two states very fast, while, at low temperatures, the zz can be a stable edge. At 1500 K, it can easily be observed in computer simulations and τ_e qualitatively matches the typical times between transitions as found in MD (see Fig. 2.3).

2.5   Conclusion

In summary, we have studied the edges of graphene nanoribbons using the LCBOPII potential by MD and MC simulations. A correct description of the armchair and, of the reconstructed zz(57) edge was achieved by a simple modification of the LCBOPII potential described in the Appendix. We have compared the equilibrium structure at $T = 0$ K with the results of *ab initio* calculations [56] and examined the role of out-of-plane displacements. We have identified a reaction coordinate for the zz to zz(57) edge reconstruction which allows us to calculate, by umbrella sampling MC, the free-energy profile for the transformation. At room temperature, we find the energy barrier for the reconstruction of a whole edge to be 0.7 eV per edge unit cell, in good agreement with

the value of 0.6 eV found with DFT at $T = 0$ K. However, we find that the first step of the reconstruction, namely, the transformation of a single pair of hexagons into a pentagon-heptagon pair has a higher energy barrier of about 0.83 eV and, therefore, it is this barrier that determines the escape rate. The escape time derived from this value might justify the abundance of nonreconstructed zz edges experimentally observed at room temperature.

2.6 Improved treatment of conjugation

The hereafter described modification of LCBOPII to improve the description of the edge bonds of a graphene ribbon concerns the conjugation term F_{ij}^{conj}, which represents a contribution to the bond order. According to LCBOPII [65], F_{ij}^{conj} depends linearly on the number of valence electrons available for the bond ij supplied by the atoms i and j. In the original version, the four valence electrons of an undercoordinated C atom, i.e., an atom with less than four neighbours, are distributed according to the following rule. One electron is supplied to each bond with a saturated neighbour and the remaining electrons are equally shared among the bonds with the other neighbours. According to this rule, the graphene ac and zz(57) edge bonds (see Fig. 2.8a), with electron contributions of $N_{ij}^{el} = N_{ji}^{el} = 2$ from atoms i and j, will be assigned to be a double bond with an equilibrium bond distance of 1.33 Å. In contrast, DFT calculations predict an equilibrium bond distance of 1.24 Å, which corresponds to a bond strength in between double and triple, about 1/3 of a double and 2/3 of a triple bond. At the same time, according to the above LCBOPII rule, the contribution of $N_{ik}^{el} = 2$ electrons from atom i to the bond ik is not balanced by the contribution of $N_{ki}^{el} = 4/3$ electrons from the sp^2 coordinated atom k, giving rise to a frustrated situation, which is penalized with the so-called antibonding term A_{ij} in LCBOPII. This unfavourable situation can be resolved in a natural way by the alternative charge distribution shown in Fig. 2.8b, in which the edge atom i (j) supplies a number of electrons equal to 8/3 = (1/3)×2 + (2/3)×3 to the edge bond ij, leaving 4/3 electrons of i (j) for the bond ik (jl), in balance with the electron supply N_{ki}^{el} (N_{lj}^{el}) of the other neighbour k (l)

To improve the electron partition rule of LCBOPII, one could think of minimizing the following functional:

$$F(\{N_{ij}^{el}\}) = \sum_{<i,j>} \left(N_{ij}^{el} - N_{ji}^{el} \right)^2 \ , \tag{2.5}$$

the sum running over all neighbor pairs ij, under the constraints:

$$V_i = \sum_i N_{ij}^{el} = 4 \tag{2.6}$$

for all atoms i in the systems, $V_i = 4$ being the (effective) number of valence electrons

for carbon. It can be shown that, if one defines the electron charge on an atom i as:

$$Q_i^{el} = \frac{1}{2} \sum_i \left(N_{ij}^{el} + N_{ji}^{el} \right) \tag{2.7}$$

the minimization of F is equivalent to minimizing the charge transfer, providing a physical basis for our approach. However, minimizing F in Eq. (2.5) with the N constraints (2.6) is a nonlocal problem, which amount to solving a coupled set of $\gamma N/2 - N$ linear equations, γ being the average coordination number. For efficient MC or MD simulations, this is not desirable and we have to look for further approximations. To obtain the desired electron partition for the edge of a graphene ribbon, as depicted in Fig. 2.8(b), it appears to be sufficient to minimize only a part of the functional F, involving just the local environment of the edge bond ij. In particular, for bonds between two atoms with coordination 2, we minimize the functional:

$$\tilde{F} = \left(N_{ij}^{el} - N_{ji}^{el} \right)^2 + W_{ki} \left(N_{ik}^{el} - N_{ki}^{el} \right)^2 + W_{lj} \left(N_{jl}^{el} - N_{lj}^{el} \right)^2 \tag{2.8}$$

where the weight factors W_{ki} and W_{lj}, defined below, are added to account for possible saturation of the atoms k and l and where N_{ki}^{el} and N_{lj}^{el} are fixed by the rule:

$$N_{ki}^{el} = max \left(1, \frac{V_k}{N_{ki} + 1} \right) = max \left(1, \frac{4}{N_{ki} + 1} \right) \tag{2.9}$$

and similarly for N_{lj}^{el}. In Eq. (2.9), $N_{ki} = N_k - S_{N,ki}^{down}$ is the so-called reduced coordination of atom k, $N_k = \sum_m S_{N,km}^{down}$ being the total coordination of atom k [65]. Here, S_N^{down} is a smooth cutoff function for the short range (covalent) interactions, allowing for noninteger or fractional coordination. According to Eq. (2.9), in the case of the ac and zz(57) graphene edges, $N_{ki}^{el} = N_{lj}^{el} = 4/3$. Since, according to LCBOPII, the conjugation term in the case of a fractional neighbour k (l) of atom i (j) is evaluated as a weighted superposition of local configurations with only full neighbours (i.e., with $S_{N,ik}^{down} = 1$), the denominator in Eq. (2.9) is $N_{ki} + 1$ instead of $N_{ki} + S_{N,ki}^{down}$. The weight factor $W_{ki} = W_{ki}(N_{ki})$ in Eq. (2.8) depends on N_{ki}, and is defined as:

$$W_{ki} = \frac{1}{1 - S_{M,ki}^{up}} \tag{2.10}$$

where $S_{M,ki}^{up}$ is a switch function going from 0 to 1 for $N_{ki} + 1$ going from 3 to 4. Hence, W_{ki} diverges when k becomes a saturated neighbor, in which case minimisation of $\tilde{F}$ will lead to $N_{ik}^{el} = N_{ki}^{el} = 1$ as it should be. W_{jl} is defined likewise. In Eq. (2.8), N_{ij}^{el} and N_{ji}^{el} can be eliminated by using the constraints in Eq. (2.6), leaving us to minimize $\tilde{F}$ with respect to the two variables N_{ik}^{el} and N_{jl}^{el}, which, by straightforward minimization, leads to:

$$N_{ik}^{el} = \frac{(2 - S_{M,lj}^{up}) N_{ki}^{el} + (1 - S_{M,ki}^{up}) N_{lj}^{el}}{3 - S_{M,ki}^{up} - S_{M,lj}^{up}} \tag{2.11}$$

$$N_{jl}^{el} = \frac{(1 - S_{M,lj}^{up})N_{ki}^{el} + (2 - S_{M,ki}^{up})N_{lj}^{el}}{3 - S_{M,ki}^{up} - S_{M,lj}^{up}} \tag{2.12}$$

from which N_{ij}^{el} and N_{ji}^{el} can be determined using Eq. (2.6).
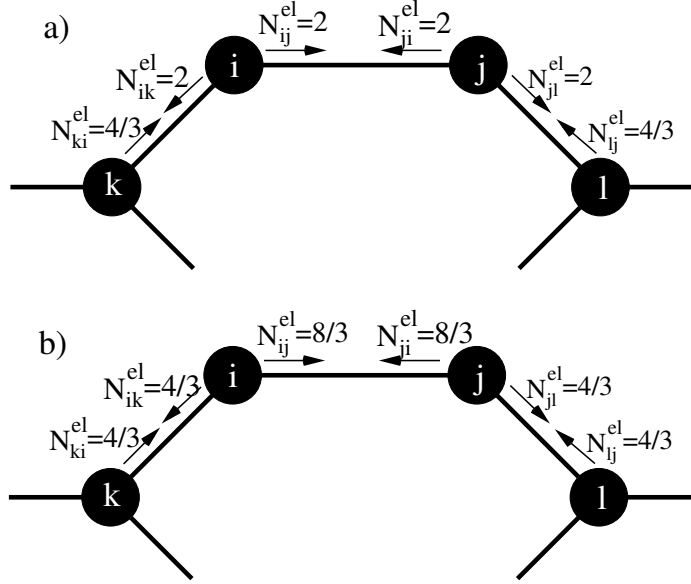
Figure 2.8: Electron partitions according to (a) the original and (b) the modified LCBOPII.

By applying Eqs. (2.11) and (2.12) to the graphene ribbon edge bond ij in Fig. 2.8, with $S_{M,ki}^{up} = S_{M,lj}^{up} = 0$, we find indeed the electron distribution given in Fig. 2.8(b). We note that the rule presented here correctly describes other configurations as well. For instance, if atom k would have an additional neighbor, so that atom k becomes saturated, then $S_{M,ki}^{up} = 1$, $N_{ki}^{el} = 1$, and $N_{ik}^{el} = 1$ corresponding to a single bond. If also atom l would have an additional neighbor, then we find $N_{jl}^{el} = N_{ik}^{el} = 1$ and $N_{ij}^{el} = N_{ji}^{el} = 3$ making ij a triple bond as it should be. On the other hand, if both atoms k and l would have one neighbour less, then $S_{M,ki}^{up} = S_{M,lj}^{up} = 0$, $N_{ki}^{el} = N_{lj}^{el} = 2$, leading to a double bond with $N_{ij}^{el} = N_{ji}^{el} = 2$.

For this work, we have only modified the conjugation term for a bond between two twofold-coordinated atoms, i.e., atoms with reduced coordination $N_{ij} = N_{ji} = 1$, where the effects are most significant. A more general treatment will be presented elsewhere [70].

Chapter 3

Dangling bonds and magnetism of grain boundaries in graphene

Grain boundaries with dangling bonds (DBGB) in graphene are studied by atomistic Monte Carlo and molecular dynamics simulations in combination with density functional (SIESTA) calculations. The most stable configurations are selected and their structure is analyzed in terms of grain boundary dislocations. It is shown that the grain boundary dislocation with the core consisting of pentagon, octagon and heptagon (5-8-7 defect) is a typical structural element of DBGB with relatively low energies. Electron energy spectrum and magnetic properties of the obtained DBGB are studied by density functional calculations. It is shown that the 5-8-7 defect is magnetic and that its magnetic moment survives after hydrogenation. The effects of hydrogenation and of out of plane deformations on the magnetic properties of DBGB are studied.

3.1 Introduction

Most potential applications of graphene require to construct macroscopically large samples that are bound to be polycrystalline. Several routes are currently actively pursued to obtain large samples in an efficient way. Examples are evaporation of surface layers of SiC [71, 72], solution of graphite without functionalization, in combination with sonication [73, 74, 75] to obtain graphene paper (laminate) and chemical vapor deposition on metals [76, 77]. Studies of graphene grown by these methods confirm the existence of grain boundaries (GB), as was observed in graphene on SiC [78], Ir(111) [79, 80], polycrystalline Ni [81] and Cu [82]. Although the presence of GB may be detrimental for electron mobility and mechanical strength, GB are potentially interesting by themselves, e.g. by metallicity along the grain as shown in Ref. [83]. Several theoretical papers have considered the structure [45, 84, 85, 86] and electronic [87] properties of tilt GB in graphene.

GB were subject of intensive experimental and theoretical study in the 70's of last century. At that time, the basic principles of formation of GB structures were understood and the special class of GB characterized by high symmetry was identified by use of the coincidence site lattice (CSL) approach [46]. These GB have optimal matching of the grains and, being energetically the most favourable, are dominant in well annealed polycrystalline samples. Most GB studied experimentally in graphene can indeed be classified as low energy structures within the CSL theory [86, 77]. These GB consist of regularly arranged dipoles of disclinations with rotation angles $\pm 60°$ associated with 5 and 7-fold carbon rings [45]. The distance between disclination dipoles depends on the misalignment of the grains. The high strength characteristics of these GB in graphene [84] confirms the strong bonding in the core of the 5-7 disclination dipoles.

In bulk materials, however, also less favourable GB with extrinsic structural defects, extra volume excess and large elastic strain have been observed depending on the treatment of polycrystalline samples [88]. Also for graphene, one may expect this situation for samples obtained by coalescence of independently growing nuclei as typical of chemical vapour deposition. The properties of more general GB have been considered in Ref. [89] and in Ref. [85] it was shown that, besides 5-7 pairs, there are 8-fold rings which dominate at tilt angle close to 15° as well as 4- and 9-fold rings with less probability. Beside having higher energy and excess free volume, these GB may also present dangling bonds and resemble structures found in amorphous graphene obtained by electron bombardment [90].

The possibility of dangling bonds makes these high energy GB particularly interesting since the dangling bonds can carry magnetic moments and are potential sources of magnetic ordering [91]. The possibility that grain boundaries can be a source of magnetism in graphitic materials was suggested in Ref.[10] based on the following experimental observations in highly oriented pyrolytic graphite (HOPG). STM studies of GB with different periodicities found some peaks in the local density of states at-

tributed to dangling bonds. Depending on the periodicity of the GB, these additional peaks in the density of states were either situated at the Fermi energy or split, which was interpreted as spin splitting. The room temperature ferromagnetism measured by magnetic force microscopy and bulk magnetization measurements was tentatively attributed to two-dimensional magnetic ordering at the grain boundaries. The observation of room temperature ferromagnetism was, however, not confirmed in other studies of HOPG [92]. Recently, a systematic study of samples of HOPG of different manufacturers [19] has convincingly attributed the macroscopic magnetic signal found in some of them to Fe-rich inclusions buried in the bulk. Nevertheless, the local STM data of Ref.[10] could still be related to the existence of localized magnetic moments and the possibility to achieve ferromagnetism in *sp* electron materials remains very appealing [11] and justifies further research.

In this chapter, we study systematically the structural, electronic and magnetic properties of GB with dangling bonds (DBGB) in graphene by a hierarchical approach based on classical atomistic simulations and ab-initio calculations. As a result of a massive search based on simulated annealing by classical Monte Carlo simulations, we find, that a particular structure with 5, 8 and 7 rings (5-8-7) appears to be kinetically stable up to high temperature and can be a common structural element of generic GB in graphene. According to our DFT calculations the 5-8-7 defect contains one dangling bond with an associated magnetic moment of $\simeq 0.5 - 1.0\mu_B$ with μ_B the Bohr magneton, that is only partially reduced by hydrogenation. This means that, in contrast to the low energy GB, a generic GB in graphene and graphite can have unpaired electrons and magnetic moments. Note that, according to our calculations, the hydrogenation of DBGB turns out to be energetically favourable, thus, the most probably realistic DBGB in graphene should be passivated by hydrogen. At the same time, all qualitative conclusions about the structure and magnetism of GB do not depend on this assumption.

The chapter is organized as follows. In section 3.2 we present the methods for atomistic simulations and ab-initio calculations. In section 3.3 we describe the structure and energetics of DBGB in graphene and in Section 3.4 we discuss their electronic structure and spin density. Finally, in Section 3.6 we give a summary and conclusions.

3.2 Method

A systematic study of GB is computationally demanding because it requires the examination of very large samples. Therefore we have done a first search for DBGB by means of Monte Carlo simulations based on the classical LCBOPII interatomic potential [65]. After having identified the 5-8-7 structure as a promising basic unit for DBGB, we have studied the electronic and magnetic properties by means of spin polarized Density Functional Theory (DFT) calculations as implemented in the SIESTA code. The drawing of flat pictures was done using the xyz2eps utility [93] written in

Python Programming Language [94]. The visualization of 3D structures together with 3D charge density was done using the VESTA visualization program [36].

3.2.1 Atomistic simulations with LCBOPII

The classical bond-order potential LCBOPII [65] has been shown to describe accurately the structure [95, 96] and elastic properties [97] of graphene as well as the phonons [98], the structure of the edges [99] and bilayer graphene [100]. The accuracy of this potential for dealing with GB has been validated against DFT calculations in Ref. [86]. For the present study, this potential has the important feature of being reactive, namely to allow breaking and formation of bonds as it would happen when grains meet.

We have used Monte Carlo simulations in the NPT ensemble, namely we have kept temperature T and number of particles N constant and allowed volume fluctuations as to keep the pressure P=0. To find (meta)stable structures we have done a simulated annealing lowering the temperatures from 3300K. The procedure to construct the samples is described in section 3.2.3.

3.2.2 DFT ab-initio calculations with the SIESTA code

We have performed spin polarized DFT [20, 21] calculations by means of the package SIESTA which implements DFT on a localized basis set [22, 23, 24]. We used GGA with Perdew-Burke-Ernzerhof parametrization (GGA-PBE) [28] and a standard built-in double-ζ polarized (DZP) [25] basis set to perform geometry relaxation of graphene samples with GB. The DZP basis set represents core electrons by norm-conserving Troullier-Martins pseudopotentials [101] in the Kleynman-Bylander nonlocal form [102]. For a carbon atom this basis set has 13 atomic orbitals: a double-ζ for 2s and 2p valence orbitals and a single-ζ set of five d orbitals. The cutoff radii of the atomic orbitals were obtained from an energy shift equal to 0.02 Ry which gives a cut-off radius of 2.22 Å for s orbitals and 2.58 Å for p orbitals. The real-space grid is equivalent to a plane-wave cutoff energy of 400 Ry, yielding $\approx$ 0.08 Å resolution for the sampling of real space. For non periodical directions, an extra space larger than 15 Å was added to avoid spurious interactions. We used k-point sampling of the Brillouin zone based on the Monkhorst-Pack scheme [103] where the number of k-points was defined similarly to the k-grid cutoff radii equal to 15 Å which usually gives 4-20 k-points depending on the sample size. The geometries were relaxed using the conjugate gradient method until all interatomic forces were smaller than 0.04 eV/Å and the total stress less than 0.0005 eV/Å^3. No geometrical constrains were applied during relaxation.
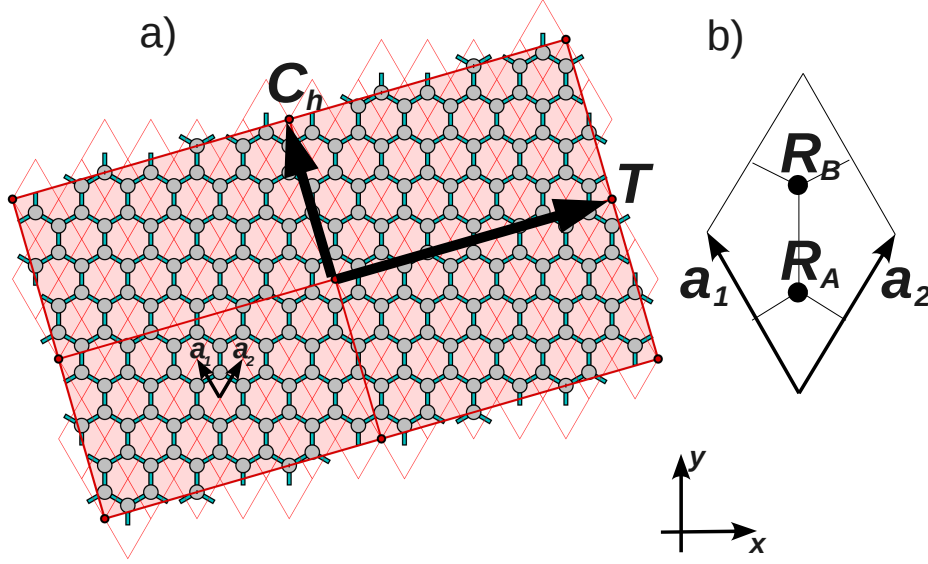
Figure 3.1: Definition of chirality vector $\mathbf{C}_h$ (a) and unit cell represented by lattice vectors $\mathbf{a}_1$ and $\mathbf{a}_2$ with basis ($\mathbf{R}_A$, $\mathbf{R}_B$) (b). For clarity the grain defined by vectors $\mathbf{C}_h$ and $\mathbf{T}$ is replicated twice along the direction of $\mathbf{C}_h$ and $\mathbf{T}$

3.2.3 Grain boundary structural model

It is common practice to generate GB by means of the coincidence site lattice (CSL) and this theory has also been used to study low-energy GB in graphene [86]. The CSL theory, however, includes only symmetric grain configurations and is not suitable to deal with generic GB, like the DBGB we study here. Therefore we use a more general model, inspired by the theory of nanotubes [104] and similar to that used in Refs. [45, 86] for symmetric GB.

A nanotube is uniquely defined by a pair of integers (m, n) relating the chirality vector $\mathbf{C}_h$ to the basis vectors of the hexagonal lattice $(\mathbf{a}_1, \mathbf{a}_2)$ as

$$\mathbf{C}_h = m\mathbf{a}_1 + n\mathbf{a}_2 \tag{3.1}$$

where

$$\mathbf{a}_1 = r_{cc}(-\sqrt{3}/2, 3/2) \qquad \mathbf{a}_2 = r_{cc}(\sqrt{3}/2, 3/2) \tag{3.2}$$

and $r_{cc} = 1.42$ Å is the interatomic distance in graphene giving $a_0 = \sqrt{3}r_{cc}$ as lattice constant (see Fig. 3.1a). For nanotubes, the vector $\mathbf{T}$ orthogonal to $\mathbf{C}_h$ gives the nanotube axis and $\mathbf{C}_h$ gives the direction of rolling. In terms of (m, n) the vector $\mathbf{T}$ is given by

$$\mathbf{T} = \frac{t_1}{k}\mathbf{a}_1 + \frac{t_2}{k}\mathbf{a}_2 \tag{3.3}$$

where

$$t_1 = -m - 2n \qquad t_2 = 2m + n \tag{3.4}$$

and k is the greatest common divisor of $|t_1|$ and $|t_2|$.

Furthermore we call $\mathbf{R}_A$ and $\mathbf{R}_B$ the positions of the two atoms in the unit cell of the hexagonal lattice. The case

$$\mathbf{R}_A = r_{cc}(0, 1, 0) \qquad \mathbf{R}_B = r_{cc}(0, 2, 0) \tag{3.5}$$

is illustrated in the unit cell shown in Fig. 3.1b.

While for nanotubes the vectors $\mathbf{C}_h$ and $\mathbf{T}$ are used to define a rectangle of given chirality to be rolled, for GB the chirality vector $\mathbf{C}_h$ determines the direction of the grain boundary while the rectangular area is the graphene grain, as shown in Fig. 3.1a. In the CSL approach the second grain is symmetric with respect to the GB direction given by $\mathbf{C}_h$.

The length $d(m, n)$ of $\mathbf{C}_h$ in our basis is

$$d(m, n) = |\mathbf{C}_h| = |m\mathbf{a}_1 + n\mathbf{a}_2| \equiv r_{cc}\sqrt{3\Sigma} \tag{3.6}$$

where

$$\Sigma = m^2 + mn + n^2 \tag{3.7}$$

There may be different pairs (m, n) that give the same value of Σ. For example $\Sigma = 91$ may be obtained by pairs $(1, 9)$ and $(5, 6)$ so that, for $\Sigma = 91$, equation (3.7) has the 4 solutions $(1, 9); (9, 1); (5, 6); (6, 5)$.

The couples $(1, 9); (9, 1)$ and $(5, 6); (6, 5)$ are symmetric and are described by a single tilt angle in the CSL theory whereas *e.g.* the pair $(1, 9); (5, 6)$ is not symmetric and requires to define the two misorientation angles of the two grains

$$\cos\phi_i = \frac{2m_i + n_i}{2\sqrt{m_i^2 + m_i n_i + n_i^2}} \quad i = 1, 2 \tag{3.8}$$

In this way, by selecting two grains with the same Σ we can satisfy periodic boundary conditions also for non symmetric grains selecting different chirality vectors $\mathbf{C}_{h1}$ and $\mathbf{C}_{h2}$ together with the orthogonal vectors $\mathbf{T}_1$ and $\mathbf{T}_2$. This procedure allows to cut two rectangular grains with the same periodicity d that, after proper reorientation, can be joined together to form the GB, labelled now by two pairs of indexes (m_1, n_1) and (m_2, n_2). In case of symmetric grains i.e. $n_1 = n_2$ and $m_1 = m_2$ we can define $\theta = \phi_1 + \phi_2$.

Since the two grains are rectangular, the final structure forms a rectangular unit cell which contains two grains with two GB. This construction gives us a starting point for the search of metastable non symmetric GB that we describe in the next Section.

3.2.4   Search of (meta)stable DBGB

Once the procedure for building GB considers also asymmetric grains, most situations will yield structures with large strain and atoms that are too close to each other,

from 1.5 Å till 0.1 Å or even less. We have used two parameters to help the search for favourable structures. First, we introduce the parameter r_{min} which controls the minimal distance between atoms. If two atoms are closer than r_{min} then this pair is replaced by a single atom with average coordinates. The parameter r_{min} influences the density of atoms along the grain boundary. We have searched with different values, namely $r_{min} = 0.1, 0.4, 1.2$ Å. This procedure is physically justified because, in situation of crystal growth at high temperature, carbon atoms would be redistributed in such a way as to avoid too close overlap of the atomic cores. The other free parameter in our scheme is the shift $\mathbf{r}_{sh}$ of the sublattice vectors $\mathbf{R}_A$ and $\mathbf{R}_B$

$$\mathbf{R}_A = \mathbf{r}_{sh} + r_{cc}(0,0,0) \qquad \mathbf{R}_B = \mathbf{r}_{sh} + r_{cc}(0,1,0) \tag{3.9}$$

We use two values

$$\mathbf{r}^1_{sh} = r_{cc}(0,0,0) \qquad \mathbf{r}^2_{sh} = r_{cc}(0,1,0) \tag{3.10}$$

where $\mathbf{r}^1_{sh}$ puts the origin of the cell on one atom and $\mathbf{r}^2_{sh}$ gives the $\mathbf{R}_A$ and $\mathbf{R}_B$ shown in Fig. 3.1.

We use the freedom given by the procedure described above to construct thousands of initial configurations with GB. For each configuration, we optimize the structure by annealing the sample from 3300K by Monte Carlo simulations in the NPT ensemble with the LCBOPII interatomic potential. After a large number of Monte Carlo moves, we find structures that do not evolve any more and can be considered as metastable. Among all these configurations we search automatically the ones with two-fold coordinated carbon atoms.

Among these possibilities, the structure with 5-8-7 rings (see Fig. 3.3) is the simplest and most common. Therefore we have concentrated on this structure as prototype of DBGB. For simplicity, we have then constructed samples with 5-7-8 DBGB and different periods with symmetric grains defined by (m,n) and θ. Further relaxation of the selected structure with SIESTA affects the structure of graphene GB only marginally, which confirms the accuracy of our atomistic energy minimization. Lastly we calculate electronic and magnetic properties with SIESTA.

We have checked the stability of the 5-8-7 DBGB also by performing constant-temperature Molecular Dynamics (MD) with Nose thermostat using the DFT package SIESTA at 3300K with a time step of 1 fs. The time dependence of temperature, energy and pressure are shown in Fig. 3.2. After 1000 MD steps the structure of the 5-8-7 defect keeps its original geometry. During the dynamics, however, we observe an exchange of a 6-ring with a 7-ring that causes a mirror reflection of the 5-8-7 point defect with respect to the GB line. This transformation that keeps the original structure of the two-fold coordinated atom is shown in Fig. 3.5d.
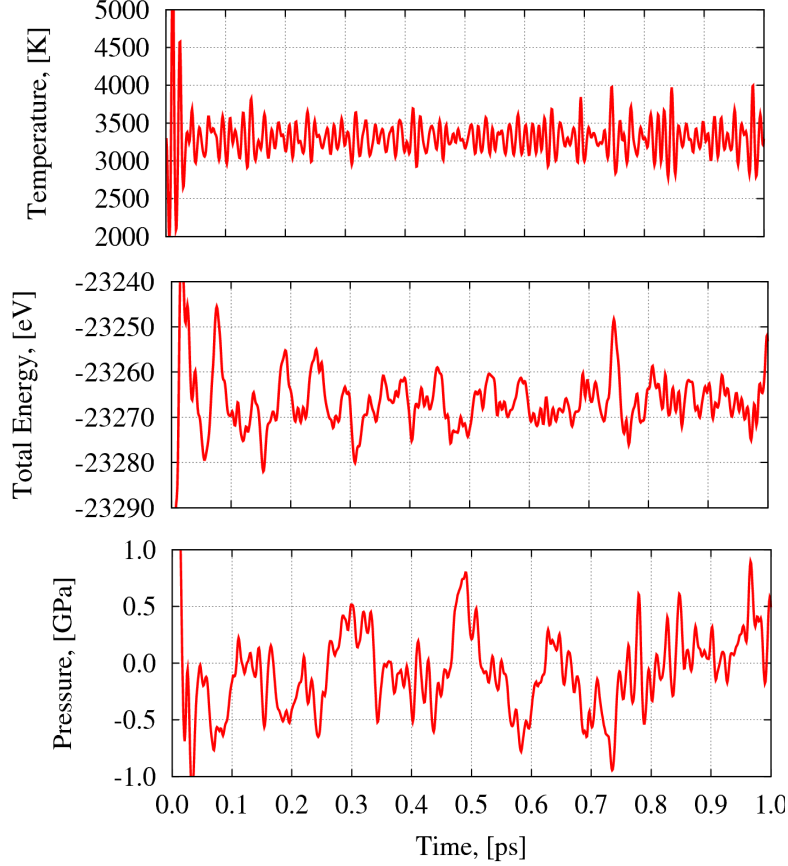
Figure 3.2: Time dependence of temperature T, total energy E_T and pressure (total stress) P during 1000 steps of MD annealing for a sample with GB with two 5-8-7 defects and 150 atoms. The mean values are $M(T) = 3299.39$ K, $M(E_T) = -23266.89$ eV, $M(P) = -0.056$ GPa with standard deviation $\sigma(T) = 187.64$ K, $\sigma(E_T) = 4.80$ eV, $\sigma(P) = 0.327$ GPa and correlation $\rho(T, E_T) = 0.039$, $\rho(P, E_T) = -0.247$, $\rho(T, P) = 0.177$.

3.3 Structure and energetics of DBGB in graphene

A more general way of describing GB is to present them as arrays of dislocations [43]. Low energy symmetric GB are nothing but arrays of 5-7 (glide) dislocations. The DBGB that we select in our search for metastable structures contain more complicated structural elements characterized by the presence of 8-, 9- and 4-fold rings. These rings appear also in simulations of disordered graphene [85] and graphene at high temperature [105], and were experimentally observed in electron bombarded graphene [90].

In Ref. [106] another type of dislocation, the shuffle dislocation shown in Fig. 3.4, with one 8-fold ring with one dangling bond, has been proposed as a potential carrier of a magnetic moment. In our search for metastable structures with dangling bonds,
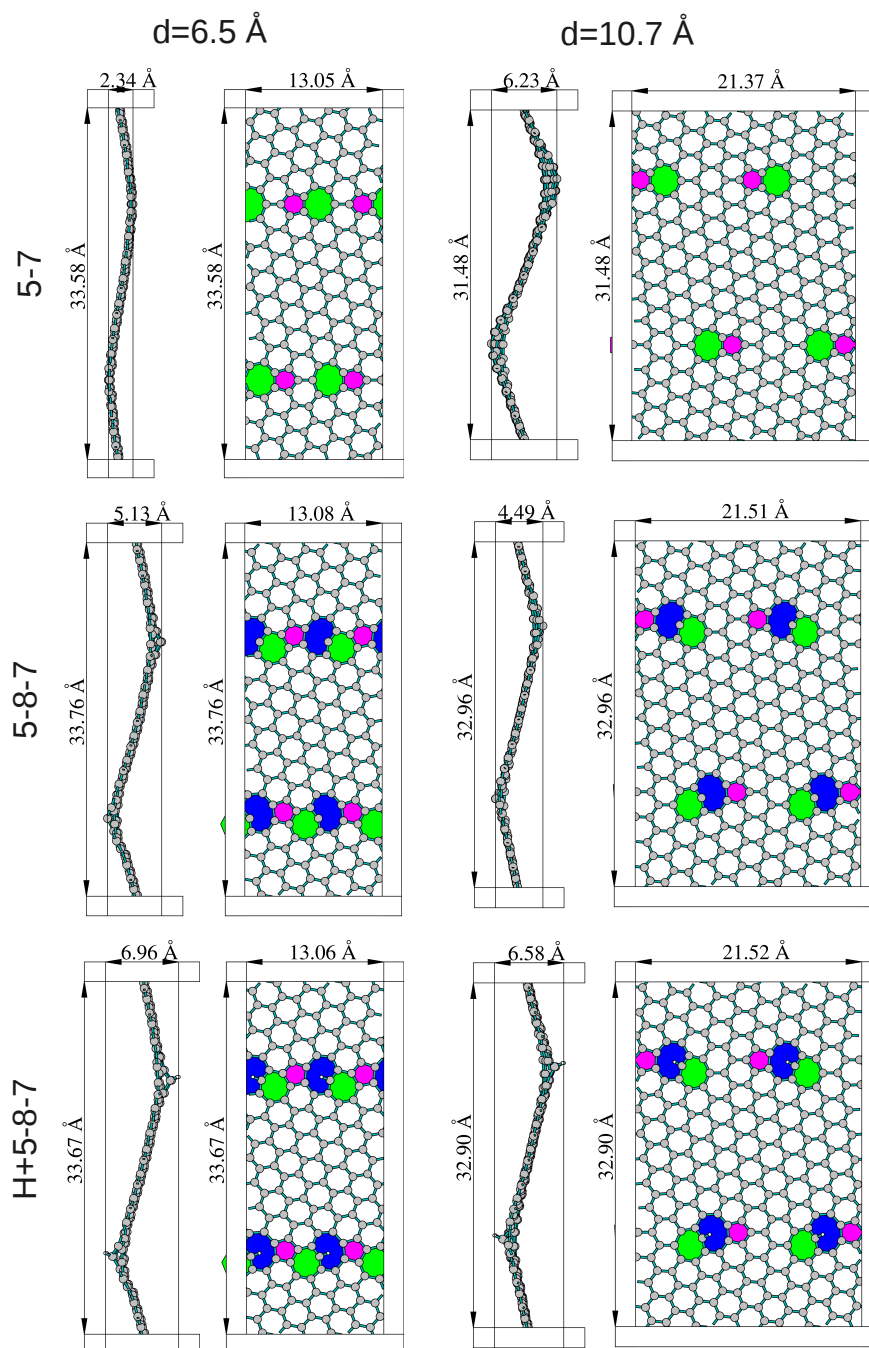
Figure 3.3: Side and top view of (from top to bottom) 5-7, 5-8-7, H+5-8-7 GB for two values of the period d, left: $d = 6.5$ Å, right: $d = 10.7$ Å. The unit cell is replicated twice in the GB direction. For clarity, 7-rings are green (light gray), 5-rings are pink (gray) and 8-rings are blue (black).
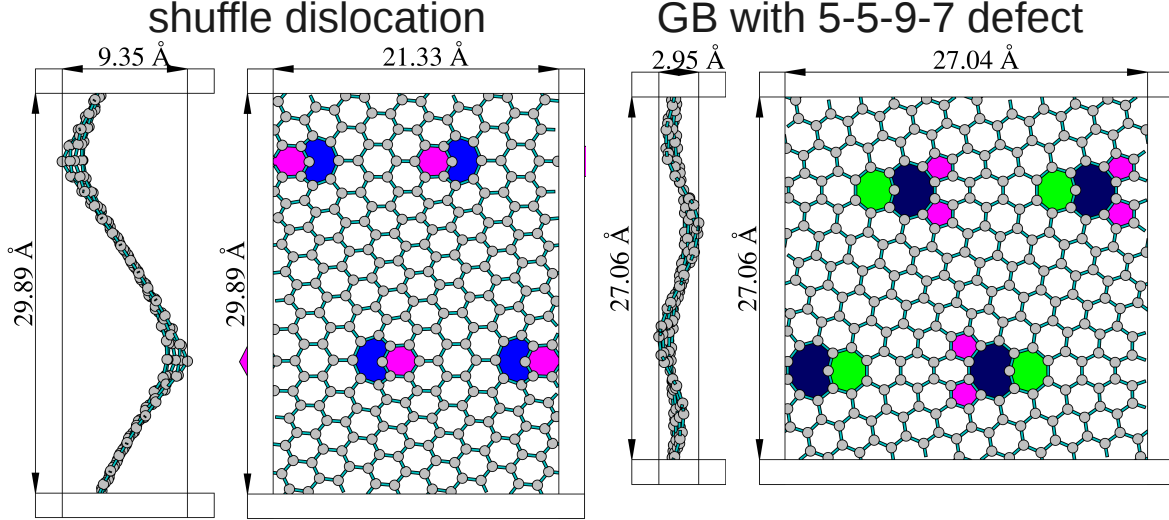
Figure 3.4: Side and top view of shuffle (left) and 5-5-9-7 GB. The unit cell is replicated twice in the GB direction. For clarity, in the shuffle GB we colour also the 6-ring.

we have found 8-fold rings only in combination with other non-hexagonal rings. If we construct a 8-ring shuffle dislocation we find that above 2400K it transforms to a 5-8-7 configuration (these two dislocation configurations are characterized by the same Burgers vector as will be discussed in detail below). By looking at Figs. 3.3 and 3.4 one can see that the shuffle GB (i.e. the wall of shuffle dislocations) has the largest out-of-plane distortion, which increases the strain in the structure [86] and might explain its instability.

In our Monte Carlo simulations at 3300K, we find most frequently the sequence 5-8-7 which has one two-fold coordinated carbon atom. This atom has one unpaired electron and, as a result, is the source of magnetic moment. We call this atom therefore a magnetic atom. If we remove the magnetic atom and apply further relaxation we find the non magnetic 5-7 defect. In Fig. 3.5 we show how the 5-8-7 is related to the 5-7 defect and how it can be constructed by either adding (Fig. 3.5b) or removing (Fig. 3.5a) an atom from it. The similar construction of a shuffle defect is shown in Fig. 3.5c. This procedure is technically reversible so that a 5-7 can be obtained by removing the magnetic atom and letting the structure rebound and relax.

One could expect the 5-8-7 DBGB to have the same Burgers vector of the glide and shuffle dislocation. In fact, if we consider the dislocation as a disclination dipole [43] the Burgers vector $\mathbf{b}$ is the product of the Frank vector of the disclination times the dipole arm. If we double the distance between the 5 and 7-fold rings that constitute the disclination, we could expect a twice larger Burgers vector $\mathbf{b} \rightarrow 2\mathbf{b}$. The 8-fold ring between the 5- and 7-fold rings can be considered as a shuffle dislocations with Burgers vector $-\mathbf{b}$ so that the resulting Burgers vector is $2\mathbf{b} - \mathbf{b} = \mathbf{b}$.

This analysis is supported by the data shown in Table 3.1 where we compare GB made of arrays of the 5-7 and 5-8-7 disclination dipoles shown in Fig. 3.3. The Burgers
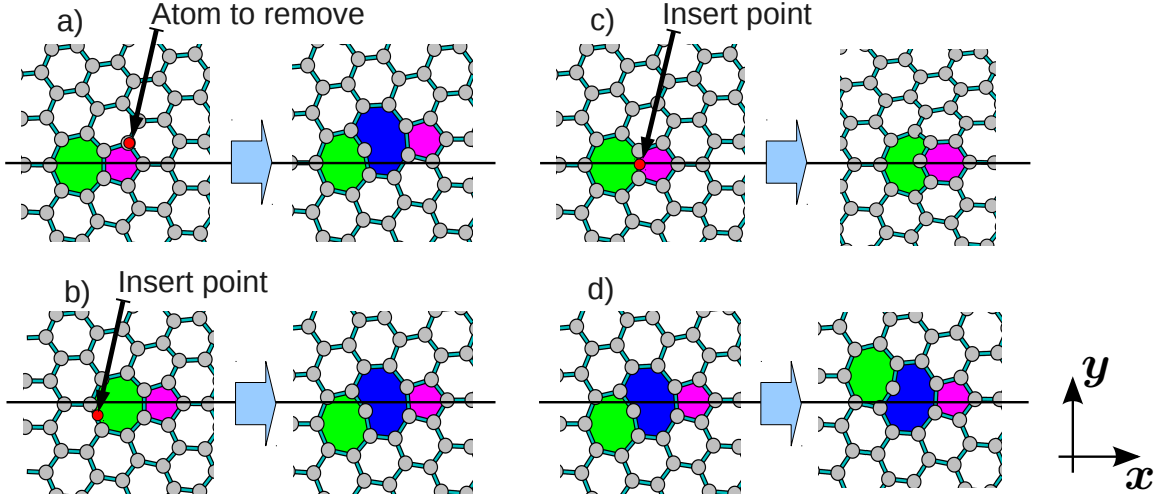
Figure 3.5: The 5-7 and 5-8-7 defects are related geometrically. There are two ways to construct a 5-8-7 defect from 5-7: remove an atom from pentagon (a), insert adatom to the bond belonging to heptagon (b). In the same way we can construct a shuffle dislocation from 5-7 (c). In panel d) we show the mirror transformation of the 5-8-7 observed in the MD simulations at T=3300 K described in section 3.2.4.

vector was calculated using the Frank equation [43]

$$b = 2d \sin \theta/2 \tag{3.11}$$

where d is the periodicity of the array and θ is the misorientation angle. One can indeed see that the Burgers vector of the 5-7 and 5-8-7 are almost the same. We also compare the formation energy of defects E_F calculated as

$$E_F = (E_{Total}^{Defect} - E_{Total}^{Graphene} \frac{N_{atoms}^{Defect}}{N_{atoms}^{Graphene}})/N_{Defects} \tag{3.12}$$

for different types of GB. The formation energy of the 5-8-7 GB is approximately twice the one of the 5-7 for the same periodicity, which is not surprising since the dangling bond costs some additional energy. The larger formation energy for the larger periodicity is consistent with the finding [86] that dislocation cores attract each other, contrary to three-dimensional materials.

The presence of the dangling bond makes bonding to other species possible. We have therefore studied the 5-8-7 also when the magnetic atom is bound to a hydrogen atom, a structure we call H+5-8-7, or to an oxygen atom or OH group, that we call O+5-8-7 and OH+5-8-7 respectively. The top and side view of H+5-8-7 shown in Fig. 3.3 do not differ much from the 5-8-7. Only the local structure of the magnetic atom is somewhat changed. In particular, the bonds to its two carbon neighbors go from $\sim$ 1.37 Å in 5-8-7 to $\sim$ 1.41 Å in H+5-8-7, a value closer to the bulk value 1.42 Å. The angle between these two bonds is also changed. The rest of the structure remains basically the same as shown in Fig. 3.6 also for the case of oxygen and OH.

Table 3.1: Summary of the studied defects with GB period d, Burgers vector **b**, GB formation energy E_F and hydrogen adsorption energy (with respect to the hydrogen atom) E_{ads}. The tilt angle together with Burgers vector were calculated for z-projected geometries i.e. completely flat samples with z=0. The binding energy of the hydrogen molecule in the used model is $E_{H_2} = 4.53$ eV.

GB	GB period d (Å)	Tilt angle $\theta°$	Burgers vector **b** (Å)	E_F (eV/defect)
5-7	6.52	20.8	2.360	2.31
5-8-7	6.54	21.7	2.467	6.83
H+5-8-7	6.53	21.7	2.461	$E_{ads} = 4.78$
5-7	10.69	13.7	2.544	3.87
5-8-7	10.76	12.7	2.378	8.01
H+5-8-7	10.76	12.5	2.350	$E_{ads} = 4.60$
shuffle	10.66	13.2	2.451	8.16
5-5-9-7	13.59	17.7	4.185	8.63

It is remarkable that the adsorption energy of the H+5-8-7 is just a bit higher than the H_2 binding energy calculated within the same method. This means that, within our computational scheme, the hydrogenation of DBGB is energetically favourable. At the same time, the difference is small and one should take into account that the density functional within GGA underestimates strongly the binding energy of H_2 molecule. Fortunately, the issue of the hydrogenation does not affect qualitatively our conclusions about the structure (as it is shown here) and magnetism (as will be shown below) of DBGB.

Since the 5-8-7 DBGB has minimal Burgers vector and low strain in view of its flatness it is natural to assume that it has the lowest energy among DBGB and therefore represents the most natural candidate as source of magnetism in GB. That is why we will focus on this structural element in the rest of this chapter. Of course more complicated DBGB exist and, as an example, we show in Fig. 3.4 the structure of a GB with $\theta = 17.7°$ formed by a periodic array of a 5-5-9-7 structural element. As reported in Table 3.1, this GB has formation energy just slightly higher than the 5-8-7 and an almost double Burgers vector. The latter statement is justified by taking into account the change of type of GB from zigzag to armchair [45]. In the following section we examine in detail the 5-8-7 in comparison to the 5-7.
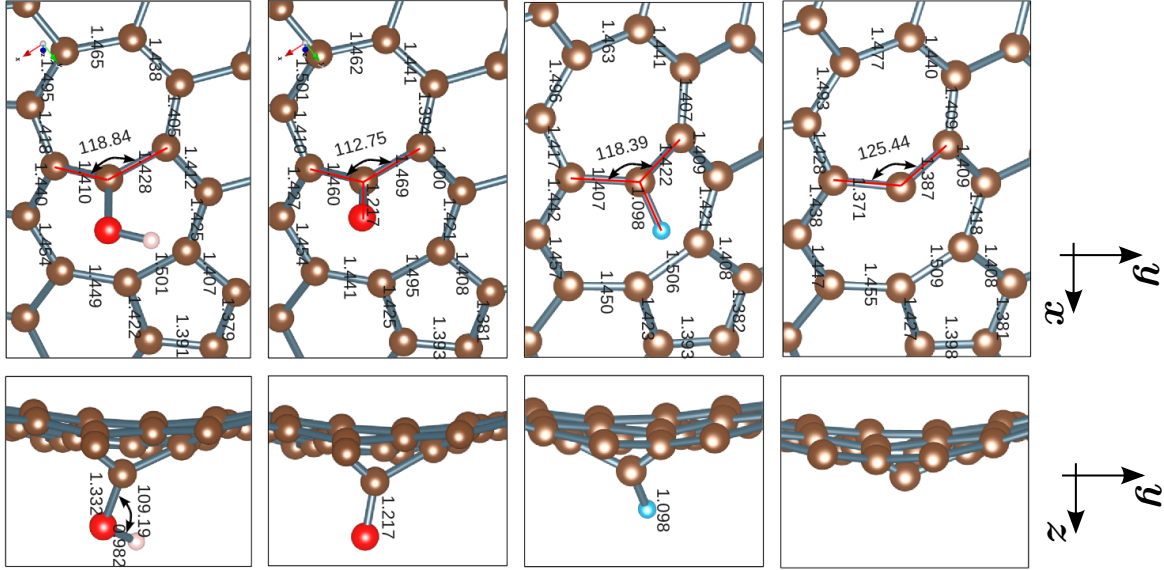
Figure 3.6: Bond lengths and C-C-C angle of magnetic atom for (from left to right) OH+5-8-7, O+5-8-7, H+5-8-7, 5-8-7 DBGB.

3.4 Electronic structure and spin density of DBGB in graphene

We have calculated the spin polarized density of states (DOS) of selected DBGB by means of SIESTA. We project the states onto the orbitals representing the p_x, p_y and p_z. In Appendix A we validate our approach against previous results for the H-saturated zigzag graphene edges [107, 108] while comparing them to non saturated edges. In Fig. 3.7 we present the spin polarized DOS for ferromagnetically oriented magnetic moments associated to the dangling bond of a 5-8-7 and H+5-8-7 with period $d = 6.5$ Å. We see that the DOS is mostly related to p_z and is essentially different for spin up and spin down. For the H+5-8-7 there is even an almost half-metallic situation with the Fermi energy lying just below the gap for majority spin electron states. Below the Fermi energy but relatively far from it, there is also a smaller gap for minority electron states. The tiny p_x, p_y components are related to the distortion from a planar sp^2 bond. In Table 3.2 we report the magnetic moments per magnetic atom. They are in general not integer. Importantly, hydrogen adsorption does not destroy the magnetic moment. This is because the magnetic atom is not like a usual dangling bond that can be fully saturated by hydrogen. A carbon atom participates with three electrons to in-plane bonding and with the fourth to the p_z band. Therefore the two-fold coordination in the plane provides a dangling bond that adds to and distorts the p_z orbital. The OH group reduces further the magnetic moment whereas oxygen destroys it completely.

Lastly, we have found that the out of plane corrugation affects the magnetic moment
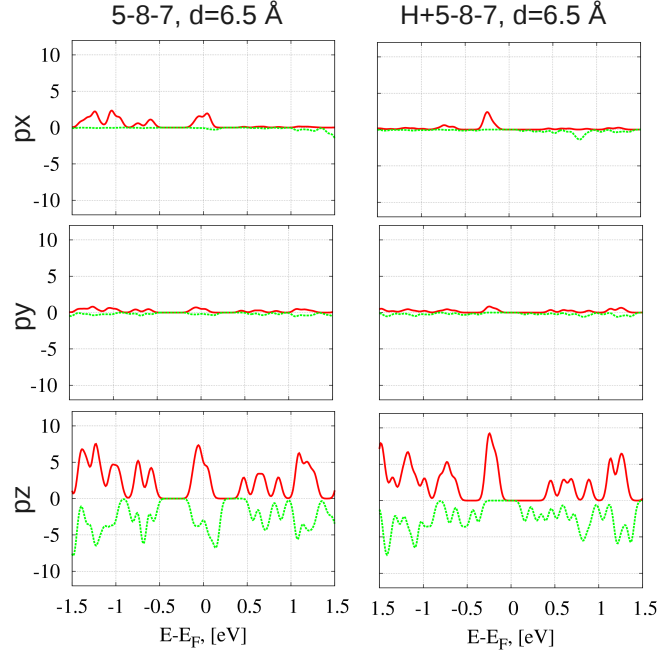
Figure 3.7: p_x, p_y and p_z components of total DOS for 5-8-7 and H+5-8-7 DBGB with misorientation angle $\theta = 21.7°$. Red solid and dashed green curves are for spin-up and spin-down respectively.
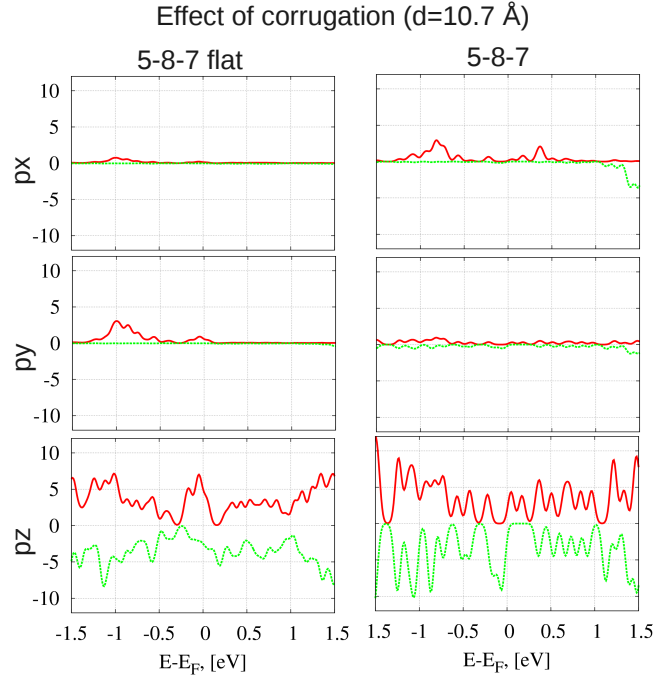
Figure 3.8: The effect of corrugation on the DOS (see the text) is seen by comparing the minimal energy 5-8-7 DBGB with the flat one. Red solid and dashed green curves are for spin-up and spin-down respectively.
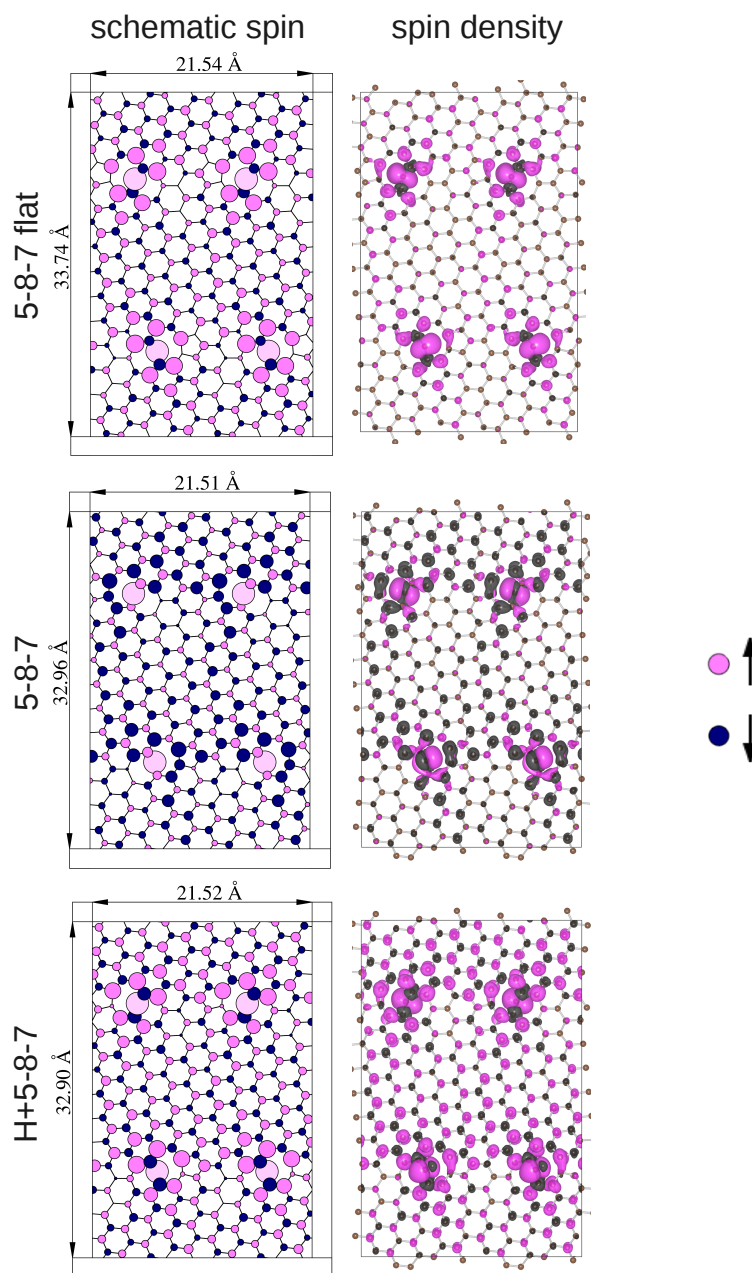
Figure 3.9: Right panels: isosurface plot of the spin density for the 5-8-7 DBGB with $\theta = 12.7°$. Left panels: symbolic representation of the spins per atom (see text). Pink (gray) and blue (dark gray) represent spin-up and spin-down, respectively. In the left panels the magnetic atoms are light pink (light gray). From top to bottom: flat configuration; minimum energy configuration without hydrogen; minimum energy configuration with hydrogen.

schematic spin   spin density
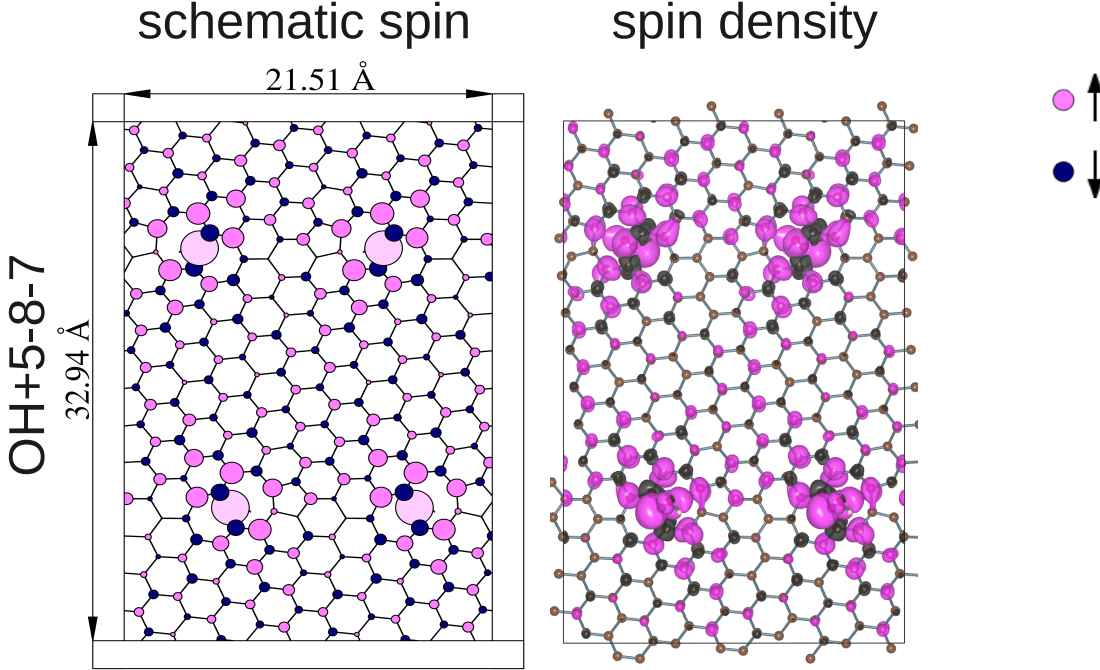
Figure 3.10: Right panel: isosurface plot of the spin density for the OH+5-8-7 DBGB with $\theta = 12.7°$. Left panel: symbolic representation of the spins per atom (see text). Pink (gray) and blue (dark gray) represent spin-up and spin-down, respectively. In the left panels the magnetic atoms are light pink (light gray).

of the 5-8-7 while it is not important for the H+5-8-7. In principle this effect can be used to control magnetic moments through strain and therefore it deserves a more detailed discussion. To this aim, in Fig. 3.8 we compare the DOS of the 5-8-7 with the one obtained for the same structure without allowing out-of-plane distortions, namely for a flat 5-8-7. Since the out of plane corrugation is larger for $d = 10.7$Å (see, Fig. 3.3) we have chosen this case to illustrate this effect. One can see that the DOS are essentially different for the cases with and without out of plane deformations. The different DOS are also reflected in the almost double value of the magnetic moments of the flat 5-8-7 as reported in Table 3.2. Conversely, the magnetic moments of relaxed and flat H+5-8-7 are comparable.

    To understand the origin of this effect we have studied the spin density in the system. In Fig. 3.9 and Fig. 3.10 we use two representations of the spin density. The one to the right is the most common representation of isosurfaces of the spin density. The representation to the left, gives the amount of spin per atom obtained from Mulliken population analysis represented as a sphere of radius proportional to the logarithm of the spin. This representation makes it possible to visualize also the small spin density components. In this way one can see that the up and down components away from the defect seem to be located on the A and B sublattices of graphene.

Table 3.2: Magnetic moment contribution in μ_B from magnetic atom which carries dangling bond (DB atom) for the studied samples with two GB and one magnetic defect per GB.

System	from DB atom	number of DB atoms	from non DB atoms	from whole system
H+5-8-7 d=6.5 (Å)	0.530	2	0.956	2.001
5-8-7 d=6.5 (Å)	0.933	2	0.843	2.708
H+5-8-7 flat d=6.5 (Å)	0.496	2	1.019	1.997
5-8-7 flat d=6.5 (Å)	0.921	2	0.850	2.692
OH+5-8-7 d=10.7 (Å)	0.291	2	0.468	1.068
H+5-8-7 d=10.7 (Å)	0.542	2	0.895	1.963
5-8-7 d=10.7 (Å)	0.455	2	-0.742	0.169
H+5-8-7 flat d=10.7 (Å)	0.455	2	1.037	1.933
5-8-7 flat d=10.7 (Å)	0.987	2	0.990	2.964
shuffle d=10.7 (Å)	0.424	2	-0.011	0.837
5-5-9-7 d=13.6 (Å)	0.889	2	-0.333	1.445

This alternation is broken by the defect in a way that depends on the out of plane distortions. In fact, in the flat 5-8-7, the magnetic atom (light gray) with spin up has the two nearest neighbour of spin down whereas in the relaxed 5-8-7 the nearest neighbours have the same spin up of the magnetic atom.

The H+5-8-7 is not sensitive to the corrugation, i.e. the spin distribution for the flat case is very similar to the one shown for the relaxed H+587 in Fig. 3.9.

Table 3.3: Magnetic moment contribution in μ_B from A- and B-sublattices for 4 studied cases.

system	m_A	m_B	$m_A + m_B$	with H	$m_A + m_B$
zz	1.464	-0.154	1.310	-	1.29 from [108]
H+zz	0.453	-0.134	0.330	0.310	0.30 from [107]
2H+zz	-0.233	0.738	0.505	0.625	-
C+zz	-0.080	0.390	0.310	-	-

3.5 Validation test for magnetism of zigzag graphene edge with and without hydrogenation

To check our computational scheme we have carried out electronic structure calculations for two cases where graphene is supposed to be magnetic, namely, zigzag edges
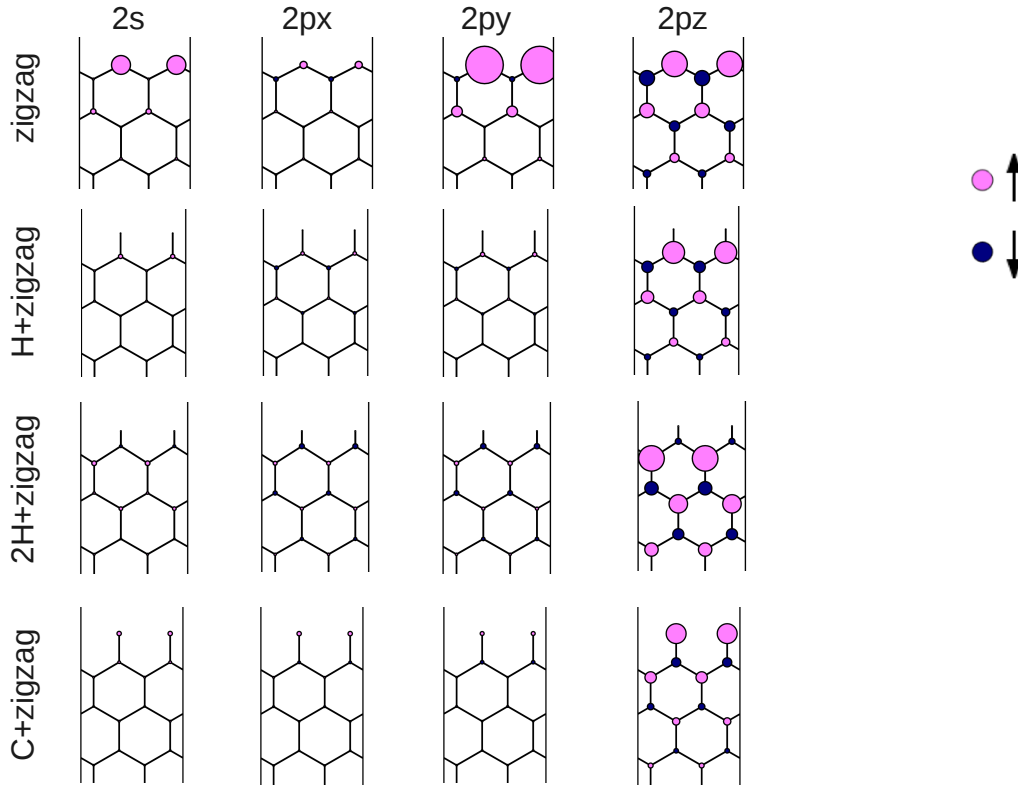
Figure 3.11: Zigzag, single hydrogenated zigzag, double hydrogenated zigzag and model zigzag graphene edge with carbon. For each case the magnetic moment decomposition over atomic orbitals for carbon atoms only is shown according to Mulliken atomic orbital population analysis. The square of each circle is proportional to the value of magnetic moment contribution. Pink (light gray) and blue (dark gray) are positive and negative values of spin respectively.

[107, 108] with and without passivation by single- and double hydrogen and carbon-terminated zigzag edge (see Fig. 3.11). The results are shown in Table 3.3. One can see that in all cases we have an excellent agreement with previous results. Furthermore, we present in Table 3.4 a more detailed information about the orbital contributions to the magnetic moments.

3.6 Conclusions

Grain boundaries (GB) seem to be unavoidable structural elements of large enough graphene samples, irrespective of their preparation. By analogy with conventional three-dimensional material science, one may expect that they will affect strongly both the mechanical and electronic properties of graphene. From a theoretical point of

Table 3.4: Detailed information about distribution of magnetic moment over orbitals for 1-fold (1nn) 2-fold (2nn) 3-fold (3nn) coordinated edge carbon atoms in the four different systems shown in Fig. 3.11, i.e. zz for zigzag, H+zz for single hydrogenated zigzag, 2H+zz for double hydrogenated zigzag and C+zz for model zigzag graphene edge with carbon atom at the edge

C-atom	2s	2px	2py	2pz	all-d	sum
zz 2nn	0.176	0.026	0.691	0.320	-0.009	1.206
zz 3nn	0.002	-0.010	-0.012	-0.112	0.075	-0.060
H+zz 2nn	0.001	0.007	0.010	0.266	-0.002	0.290
H+zz 3nn	0.002	-0.008	-0.006	-0.071	0.025	-0.057
2H+zz 2nn	-0.004	-0.013	-0.015	-0.019	0.036	-0.017
2H+zz 3nn	0.012	0.008	0.010	0.345	0.000	0.375
C+zz 1nn	0.010	0.011	0.009	0.226	0.002	0.256
C+zz 2nn	0.004	-0.004	-0.007	-0.048	0.018	-0.038
C+zz 3nn	0.002	0.002	0.000	0.074	-0.003	0.075

view, GB are very complicated objects due to the multiscale character of the problem. Both long-range deformations extending over tens of thousands of atoms and specific atomistic and electronic structure of the cores are essential. Therefore usually people study only special GB, mostly, those which can be constructed by the CSL approach [86, 45]. These GB are, indeed, usually the most energetically favorable. At the same time, e.g. for CVD growth of graphene on metals [76, 77], one could expect that various crystallites grow independently from many centers and more complicated GB will be formed. To attack this problem we have combined large-scale atomistic simulations using the LCBOBII potential [65] with ab-initio calculations. We have studied in detail GB containing the 5-8-7 defect which is the carrier of magnetic moment. Based on the results presented here one can conclude that a generic GB should contain magnetic moments which are robust enough, in particular, with respect to hydrogenation. Since GB in graphene are one-dimensional objects, they cannot lead to magnetic ordering at any finite temperature. We have shown, however, that the very existence of magnetic moments at the GB dangling bonds modifies the local electronic structure around the Fermi energy that can be probed by STM.

Chapter 4

Electronic, magnetic and transport properties of graphene ribbons terminated by nanotubes

We study by density functional and large scale tight-binding transport calculations the electronic structure, magnetism and transport properties of the recently proposed graphene ribbons with edges rolled to form nanotubes. Edges with armchair nanotubes present magnetic moments localized either in the tube or the ribbon and have metallic or half-metallic character, depending on the symmetry of the junction. These properties have potential for spin valve and spin filter devices with advantages over other proposed systems. Edges with zigzag nanotubes are either metallic or semiconducting without affecting the intrinsic mobility of the ribbon. Varying the type and size of the nanotubes and ribbons offers the possibility to tailor the magnetic and transport properties, making these systems very promising for applications.

Table 4.1: Total spin magnetization S (in unit of μ_B per unit cell) as a function of the index of AC nanotube (N, N) and size of nanoribbon P (in unit of ZZ rows). The results in this table are for samples obtained by rolling the edges of the same unrolled graphene ribbon with width of 40 ZZ rows.

N	P	S (symmetric)	S (asymmetric)
9	4	0.000	1.499
8	8	0.995	1.499
7	12	1.371	1.499
6	16	1.481	1.499
5	20	1.500	1.500
4	24	1.500	1.500
3	28	1.494	1.500

4.1   Introduction

The atomic structure of graphene edges is important for the determination of the electronic and magnetic properties of graphene, especially for narrow graphene nanoribbons [53, 49, 56, 58, 61, 109, 110, 91, 111, 112, 60, 113]. The natural termination of graphene is given either by zigzag (ZZ) or armchair (AC) edges. Theoretical studies [56] find that the minimal energy structure is instead given by a reconstruction of the zigzag edges to form pentagons and heptagon (57) but this structure has been only rarely observed [62, 63] possibly due to a large free energy barrier [99]. Recent theoretical work [114] on the stability of different graphene edges structures has shown that graphene edges can also fold back on themselves and reconstruct as nanotubes, with low formation energy (see atomic structures in figure 4.1). Previous theoretical work had considered such a structure among many other possible configurations made by a combination of nanotubes and graphene nanoribbons [115, 116] suggesting that such structure could be formed in solution.

In this chapter, we show that, besides protecting the edges from contamination and reconstructions, nanotubes at the edges may lead to magnetism and are not detrimental for the electronic mobility despite the row of sp^3 hybridized atoms at the ribbon-tube junction. We study the electronic and magnetic properties of these systems by a combination of density functional theory (DFT) and large scale tight binding (TB) simulations of transport properties. Our calculations suggest that these systems could be used for a variety of applications that we sketch in figure 4.2.

We consider systems formed by a nanoribbon terminated on both sides by the same AC or ZZ nanotube. We notice that a ribbon with AC edges is terminated by ZZ nanotubes and a ribbon with ZZ edges is terminated by AC nanotubes. Nanoribbons terminated by AC nanotubes present interesting magnetic properties. By rolling the ZZ edges of a nanoribbon, two types of AC nanotubes can be formed, as shown in figure 4.1. If the atoms at the nanoribbon ZZ edge scroll and bind to the same sublattice sites

Edges with armchair nanotube
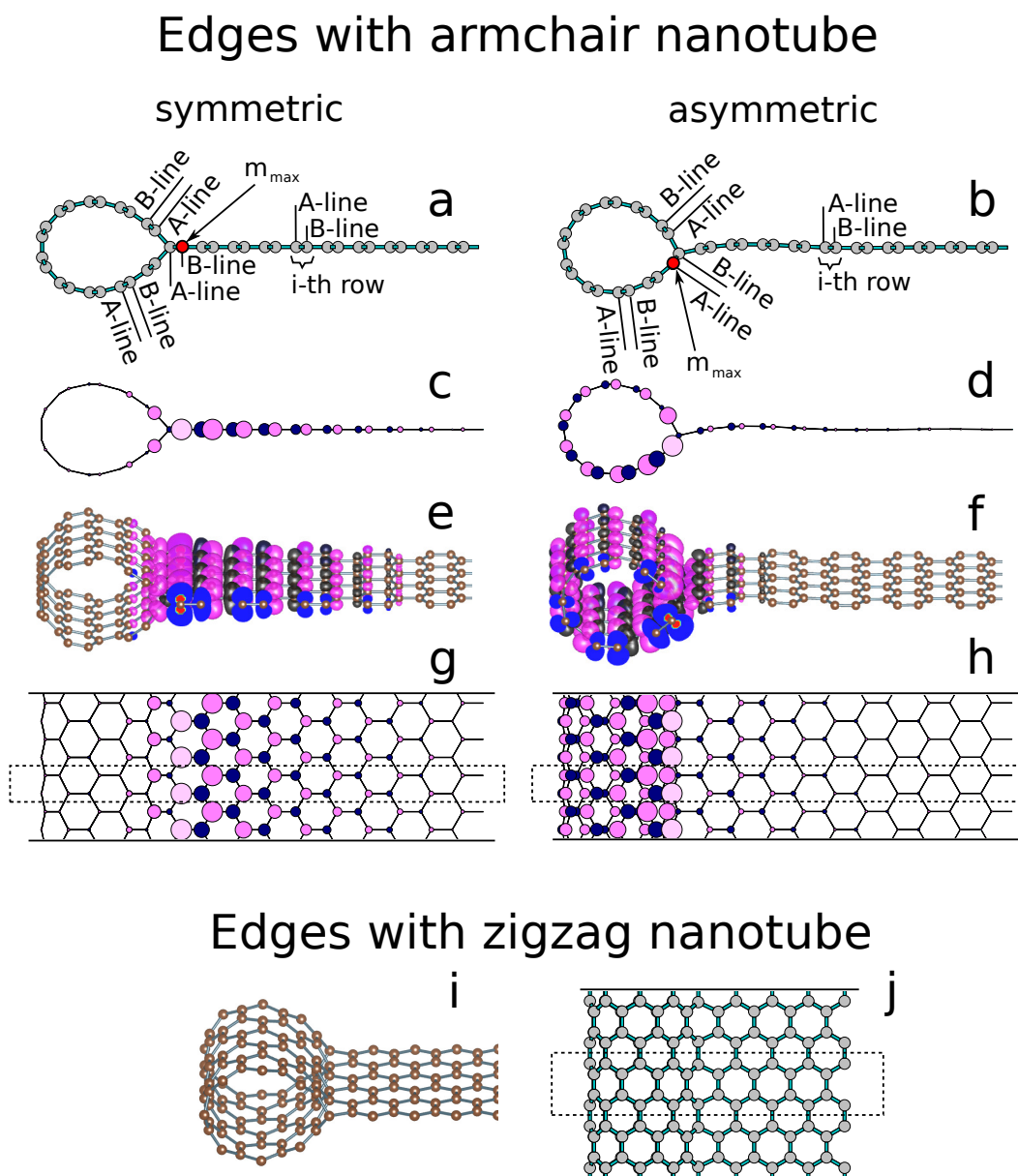
Figure 4.1: (a-h) Structure and spin density for symmetric (left) and asymmetric (right) AC nanotube terminated edges. (a,b) Atomic structure; (c,d) Side, (e,f) 3D and (g,h) top view of schematic spin representation. The box with dashed line in (g,h) indicates half of the unit cell in the DFT calculation. For the symmetric case, the contribution to the magnetic moment from atoms belonging to the A- and B- sublattices are $m_A = 0.958$ μ_B and $m_B = -0.217$ μ_B (per half unit cell), and for the asymmetric case $m_A = 1.048$ μ_B and $m_B = -0.300$ μ_B. The maximum of the magnetic moment is located on the atom indicated by the arrow with the value $m_{max} = 0.379$ μ_B in both symmetric and asymmetric cases. (i,j) 3D and top view of AC nanoribbons terminated by ZZ nanotubes. The box with dashed line in (j) indicates half of the unit cell in the DFT calculation.
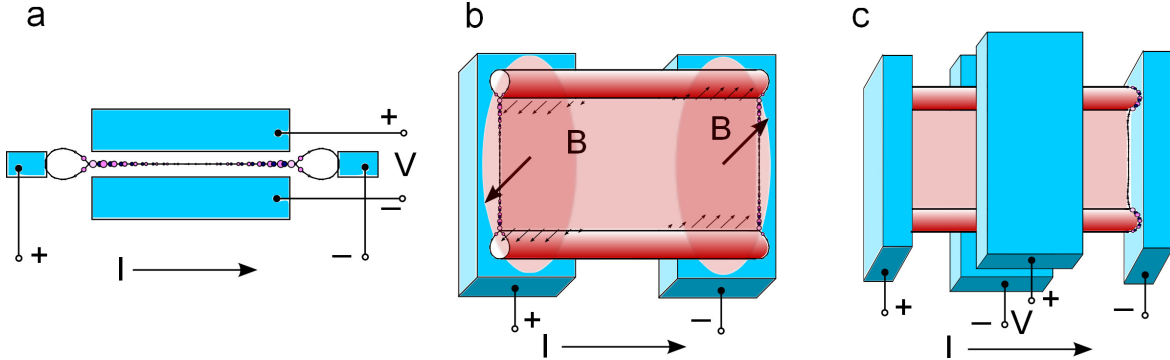
Figure 4.2: Sketch of spintronics devices based on carbon nanoribbons terminated by AC nanotubes. (a) A spin valve based on the symmetric case: a gate can be used to switch from the antiferromagnetically coupled state to the ferromagnetically coupled excited state, favouring spin transport from one nanotube to the other across the ribbon. (b) For both symmetric and asymmetric case, high magnetoresistance could be achieved by applying magnetic fields of different sign at the ends of the nanoribbons, as proposed in [117] for ZZ nanoribbons. (c) For the asymmetric case, a gate along the ribbon could be used to switch between two half-metallic energy regions to realize either a spin filter or a spin valve.

within the nanoribbon, the formed AC nanotube has mirror symmetry with respect to the nanoribbon plane; if the bonding sites belong to opposite sublattice, there is no such kind of symmetry (compare figure 4.1b to figure 4.1a). We call these two cases *symmetric* and *asymmetric* which corresponds to *armchair* and *armchair-like* in Ref. [114], respectively. The common point of these two cases is that the sublattice symmetry is broken, because all the sp^3 hybridized carbon atoms at the junction belong to one sublattice as shown in figure 4.3. Due to the Lieb theorem [91, 113], this gives the possibility of spin polarization around the junctions. Since the theorem applies to the Hubbard model, accurate calculations for the real system are necessary to investigate this possibility. Beside these symmetry considerations relevant for graphene, a general condition for magnetism that derives from the Stoner criterion is the presence of peaks in the density of states at the Fermi energy for non spin polarized calculations. As we show in the following, both symmetric and asymmetric ZZ nanoribbons terminated by AC nanotubes present such peaks and therefore are good candidates for magnetism since they satisfy both the Lieb and Stoner requirements.

4.2   Edges terminated by armchair nanotubes

In order to study the magnetic properties, we performed (spin polarized) DFT calculations by SIESTA [22, 23, 24]. We used generalized gradient approximation with Perdew-Burke-Ernzerhof parametrization (GGA-PBE) [28] and a standard built-
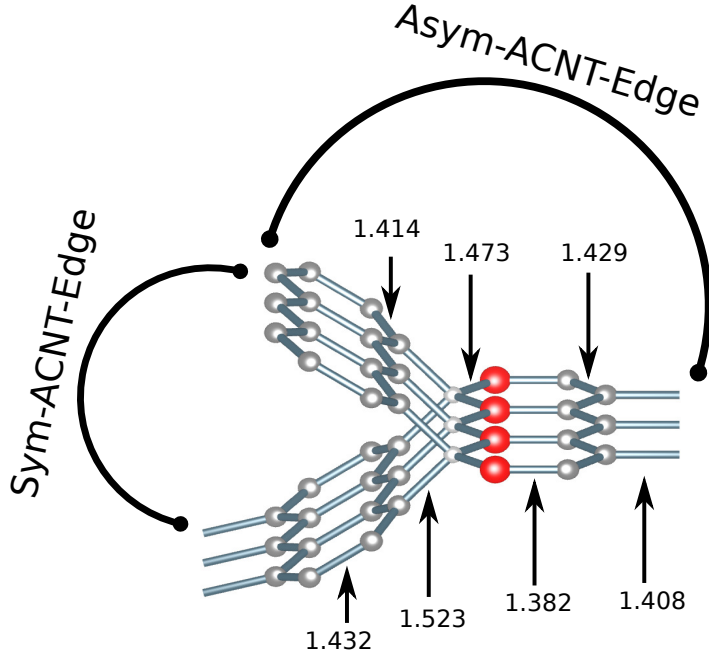
Figure 4.3: Sketch of the junction between carbon nanoribbon and AC nanotube. The junction itself is similar for both symmetric and asymmetric AC nanotube terminated edges, and the main difference is the different connection of the AC nanotube. The carbon-carbon distance indicated in the figure is for the symmetric case (N=5 and P=20), and the difference to the asymmetric case is negligible. In both symmetric and asymmetric cases, the maximum magnetization are located at the sp^2 atoms (red) which are coupled to two sp^3 atoms (light gray).

in double-ζ polarized (DZP) [25] basis set to perform geometry relaxation.

In Figure 4.4 we show the non spin-polarized band structure and density of states of both symmetric and asymmetric ZZ nanoribbons with AC nanotubes at the edges. We see that indeed sharp speaks at the Fermi energy in the density of states are present as a consequence of the flat band located at this energy. This flat band resembles the one due to dangling bonds in zz nanoribbons. In Ref. [56] it was shown that the 57 reconstruction of the ZZ edges could split this band shifting it away from the Fermi energy. The termination with nanotubes leaves a band at the Fermi energy if no spin polarization is allowed. For the symmetric case, it is easy to visualize the character of this band as a pz state decaying from the junction both in the nanoribbon and in the nanotube, as shown in Figure 4.4e. Instead of a change of bond character as for the 57 reconstruction, for our system it is the magnetic polarization that removes this state from the Fermi energy. In Figure 4.5 we show the spin polarized band structure and density of states, showing the splitting of the flat band at E_F into spin up and spin down levels and the consequent disappearance of the peaks at the Fermi energy in the density of states.
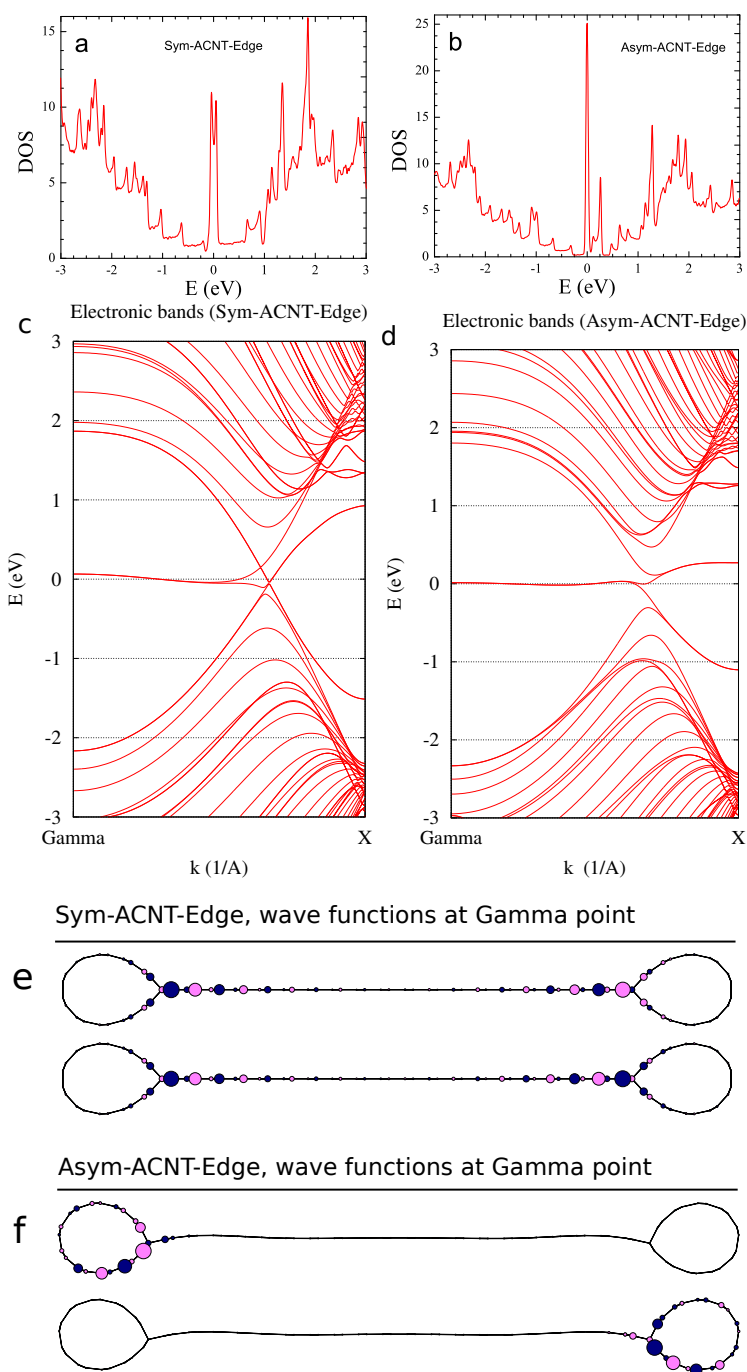
Figure 4.4: Non-spin-polarized density of states and band structure calculated by DFT for ZZ nanorribons with (a,c) symmetric and (b,d) asymmetric AC nanotube terminated edges ($N = 5$ and $P = 20$ for both cases). The density of wave functions at Γ point are shown in (e) for symmetric case and (f) for asymmetric case.
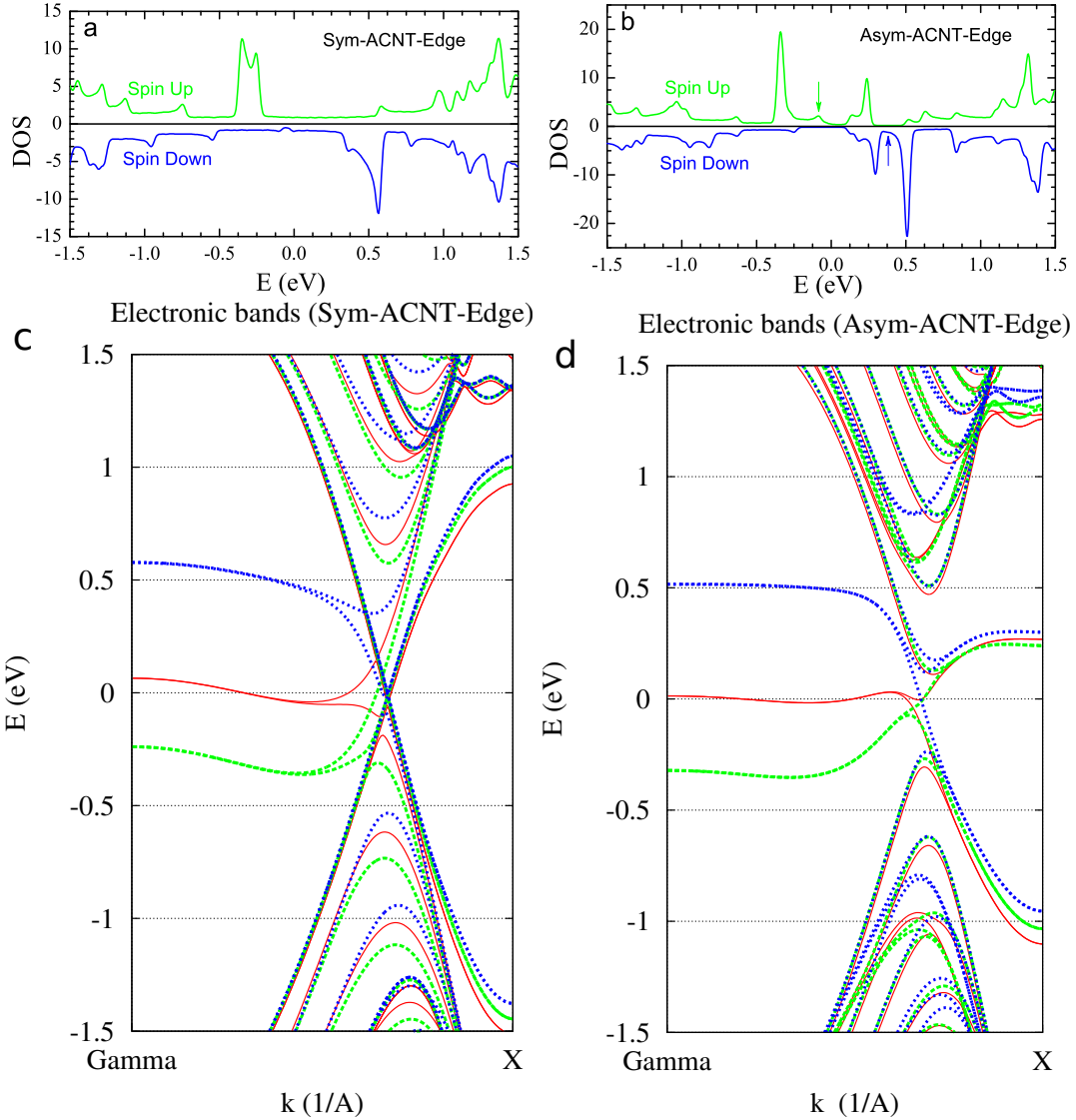
Figure 4.5: Spin-polarized Density of states and band structure (bold dashed curves) calculated by DFT for ZZ nanorribons with (a,c) symmetric and (b,d) asymmetric AC nanotube terminated edges ($N = 5$ and $P = 20$ for both cases). The arrows in (b) indicate the half-metalic energy regions for either spin up or spin down. For comparison, we show the non-spin-polarized band structure by red solid curves in (c,d).

We find that, in both symmetric and asymmetric cases, there is spin polarization near the ribbon-tube junction, i.e., near the sp^3 hybridized carbon atoms. Note that the bond distance of these four-fold coordinated atoms is 1.52 Å like in diamond. The spin polarization is mainly located in the nanoribbon for the symmetric case and within the tube for the asymmetric case (see the isosurface plot of the spin density together with its symbolic representation in figure 4.1c-h). The up/down spins are

59

distributed over the A/B sublattices respectively. The label m_{max} indicates the atom with the highest magnetic moment. A possible explanation for the localization of the spin polarization can be found by realizing that the largest polarization is on the sp^2 atoms at the junction in between two sp^3 atoms (see red atoms in Figure 4.3). The atoms with this particular configuration are either inside the nanotube or inside the nanoribbon and this corresponds to the location of the spin polarization. We are also tempted to conjecture that the localization results from a frustration mechanism. In fact in the symmetric case, where the polarization is located in the nanoribbon, the sp^3 atoms break the bipartite symmetry in the ribbon (making magnetization possible) whereas for the asymmetric case, the sp^3 atom breaks the bipartite symmetry in the nanotube.

For the symmetric case, the value of the spin polarization increases with increasing nanoribbon width, and saturates at 1.50 μ_B per unit cell, when the nanoribbon width is wider than 16 ZZ rows; For the asymmetric case, the spin polarization is always 1.50 μ_B per unit cell, irrespective of the nanoribbon width and nanotube radius (see Table 4.1).

For the asymmetric case the spins are located inside the two nanotubes and therefore the exchange interaction between opposite edges is negligible. For the symmetric case, the spins on the two edges are coupled antiferromagnetically, similarly to hydrogen terminated graphene edges [107, 108]: for the structure shown in figure 4.1a, the energy of antiparallel spin configurations is 22 meV per unit cell (see figure 4.1g) lower than for parallel configurations. This sizeable coupling across the ribbon makes the symmetric systems promising as spin valve devices [118]. In figure 4.2a we show a configuration similar to that proposed for dumbbell graphene structures on the basis of the Hubbard Hamiltonian in the mean field approximation [119]. A gate could be used to bring the system from the antiferromagnetically coupled state to the ferromagnetically coupled excited state, favouring spin transport from one nanotube to the other across the ribbon. Moreover, both for the symmetric and asymmetric case, the magnetic moments along the ribbon-tube junction are qualitatively similar to the case of ZZ edges of nanoribbons. Therefore, high magnetoresistance could be expected, as proposed in [117] for nanoribbons with ZZ edges, by applying magnetic fields of different sign at the ends of the nanoribbon. A sketch of this device for our systems is shown in figure 4.2b.

The spin polarized density of states (DOS) reveals other features of interest for spintronics related to half-metallic character. In figure 4.5a and 4.5b we show the spin polarized DOS for the symmetric and asymmetric case respectively. We see that the symmetric case is metallic for both spins in the whole range of energy. The asymmetric case, instead, is a half-metal near the Fermi energy E_F, namely it is metallic for spin up and insulating for spin down. The half-metallic character of our systems provides opportunities as spin filters without the need of external electric fields [120], magnetic fields [121], ferromagnetic strips [122], impurities [123, 124, 125] or defects [126, 127]. Furthermore, there is the opposite half-metallic character at higher energies. Around 0.4 eV, there is insulating character for spin up and metallic character for spin down.

As sketched in figure 4.2c, a gate along the ribbon could be used to switch between these two half-metallic energy regions and affect selectively the spin transport.

4.3   Edges terminated by zigzag nanotubes
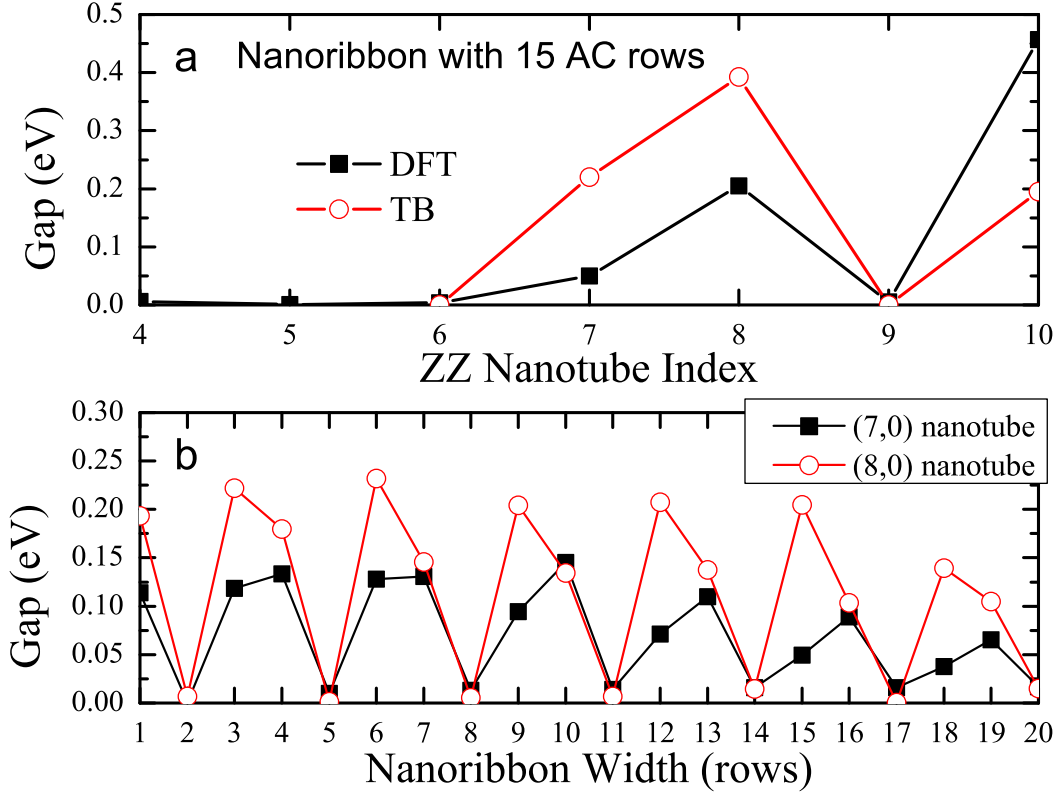
Figure 4.6: Band gap size-dependence in ZZ nanotube terminated AC nanoribbons. (a) Fixed nanoribbon with 15 AC rows for varying size of the terminating ZZ nanotube. (b) Fixed ZZ nanotube (8, 0 and 7, 0) edges for varying width of the AC nanoribbon.

We come now to the case with ZZ nanotubes shown in figure 4.1i-j. For this case, there is only one type of ribbon-tube junction that preserves sublattice symmetry implying that there is no magnetization nor midgap states [91, 113]. The electronic structure and transport properties, however, strongly depend on the AC ribbon width and on the ZZ tube radius. In TB models, a AC nanoribbon is metallic if the number of AC rows is equal to $3l + 2$, where l is a positive integer, and semiconducting otherwise [53, 128]. Furthermore, ZZ nanotubes are metallic for index equal to $3l$ [52]. In more general models, the properties of AC nanoribbons and ZZ nanotubes may differ from the ones predicted by TB, due to possible self passivation of the edges for nanoribbons and for the $\sigma - \pi$ band mixing for small nanotubes [52]. By using DFT calculations,
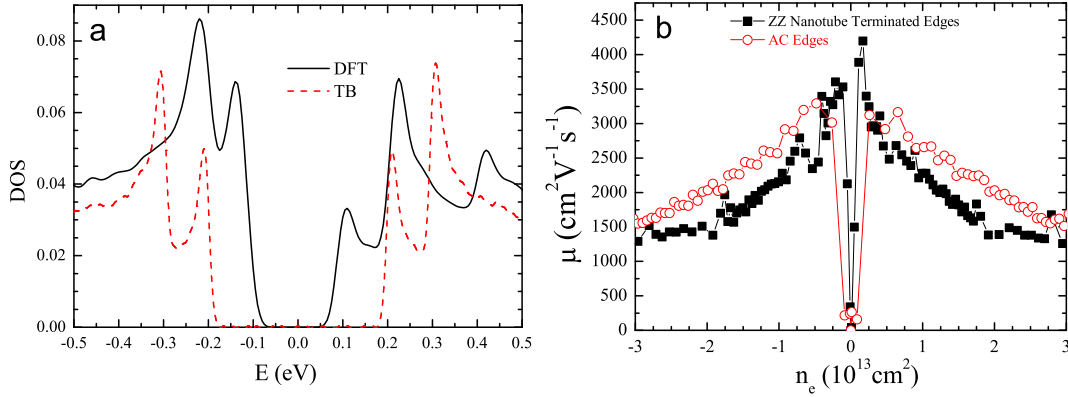
Figure 4.7: (a) Comparison of DOS of a nanoribbon with 15 AC rows terminated by (8,0) ZZ nanotubes calculated by DFT and TB. (b) Comparison of the mobility of a nanoribbon with 15 AC rows, terminated either by (8,0) ZZ nanotubes or by AC edges in TB. The charge density n_e is obtained from the density of state ρ in panel (a) by $n_e(E) = \int_0^E \rho(\epsilon) \, d\epsilon$. The sample contains 600000×47 carbon atoms for the case with ZZ nanotube terminated edges, and 2000000×15 for the case with AC edges.

we found that our joined system becomes a semiconductor with a gap of the order of few hundreds meV if both nanoribbon and nanotube are semiconducting. The energy gap as a function of geometry is shown in figure 4.6. The size of the nanotube has to be large enough for the opening of a band gap (figure 4.6a). For the joined system with semiconducting ZZ nanotubes, there is a clear periodicity (3 ZZ rows) in the dependence of the energy gap on the nanoribbon width (figure 4.6b). For the studied cases, the value of the gap varies between 30 and 600 meV.

Since we want to calculate the transport properties by means of a simpler model, suitable for large samples, we have also calculated the energy structure of our system by π-band TB calculations where we consider only the nearest-neighbour hopping $t = 2.7$ eV between the carbon atoms [129, 130] for all bonds. The comparison between the gaps calculated by TB and DFT shown in figure 4.6a gives the same periodicity and a qualitative agreement. For the case of a AC nanoribbon with 15 rows terminated by (8,0) ZZ nanotubes we compare in figure 4.7a the TB and DFT DOS, which again are in qualitative agreement as to support the validity of the transport calculations we show next. The electronic transport properties of a semiconducting nanoribbon with or without nanotube terminated edges are obtained by using large scale TB simulations with about thirty million carbon atoms [129, 130]. In figure 4.7b we show that the electronic mobility parallel to the edges as a function of charge density are quite similar in these two cases. The mobility of the joined system is about 2250 $cm^2 V^{-1} s^{-1}$ at charge density $n_e \sim 10^{13} cm^2$, which is only slightly smaller than the one of the AC nanoribbon at the same charge concentration.

4.4   Conclusion

In summary, we have studied the electronic and magnetic properties of graphene nanoribbons with three types of nanotube terminated edges. The spin magnetization is found to be 1.5 μ_B per unit cell in the ground state of both symmetric and asymmetric AC nanotube terminated edges. For symmetric AC nanotube terminated edges, the spin density is located in the ribbon whereas, for the asymmetric case, it is located within the tube. In the ZZ nanotube terminated edges, there is a band gap opening of the order of few hundreds meV, if the constituent tube and nanoribbon are both semi-conducting. The conductivity and mobility in the presence of ZZ nanotube terminated edges is comparable to the one of the AC nanoribbon itself.

Our calculations suggest that these systems are not only advantageous because the edges are protected against any kind of chemically induced disorder but also because, by tailoring the ribbon/tube structure, they offer a wealth of possible applications for transport and spintronics.

Chapter 5

Structure and magnetism of disordered carbon

Carbon has many ordered allotropes but also interesting amorphous structures. As a result of particular growth mechanisms it is found also in disordered porous structures formed by interconnected nanometer sized clusters, often called nanofoams. An example of this type of structures, as revealed in Transmission Electron Microscope (TEM) experiments [131, 8], is shown in Fig. 5.1a,b. These carbon nanofoam structures have been obtained by high-repetition-rate laser ablation of a glassy carbon target in an ambient non-reactive Ar atmosphere. Scanning Tunneling Microscopy (STM) reveals a mixed sp^2 sp^3 bonding and curved graphite-like sheets. The Fourier Transform of STM images reveals clusters arranged with period of 5.6 Å [131, 8, 9].

A reason of interest for these structures is the presence of ferromagnetic behaviour up to 90 K reported in Ref. [9] which raises questions about the mechanism for this phenomenon. These disordered structures might present magnetic moments related to undercoordinated atoms or to particular atomic arrangements. The purpose of this chapter is to investigate, by means of a large number of realizations of nanosized clusters, if some atomic arrangements appear recurrently and can give rise to magnetic moments and/or to magnetic order.

(a)　　　　　　　　　　　　　　**(b)**
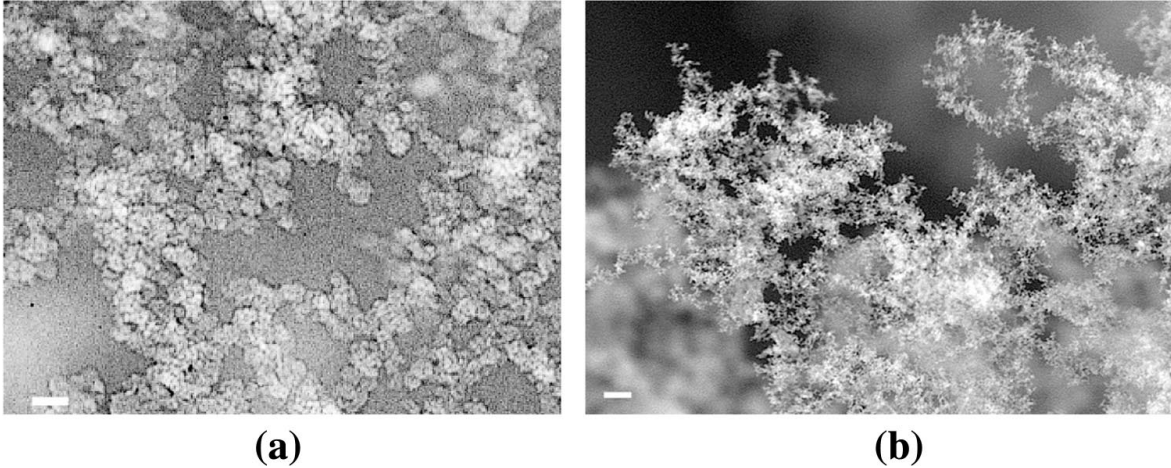
Figure 5.1: Transmission electron micrograph of the carbon foam, showing characteristic clusters (10 nm scale bar) (a). (b) Scanning electron micrograph of the foam, showing the web-like form at lower magnification (100 nm scale bar). (from [131])

5.1　Outline of this chapter

We first describe in section 5.2 the procedure to generate, in an automated fashion, series of disordered samples and the criteria to analyse this large set of results (about 24300 realizations) according to total energy, coordination and magnetic moments. In our search we consider cluster structures periodically repeated to form a bulk. In this way we disregard the possibility of magnetism related to the surfaces.

In section 5.3 we present a first screening of the magnetic properties that are the focus of our study.

In section 5.4 we examine the distribution of total energy, some structural properties and try to establish a kind of phase diagram to relate the presence of sizeable magnetic moments to the total energy of the structure. In this section we show, as a side result that we do not pursue further at this stage, that a large number of samples have energies in a narrow range just higher than that of diamond and graphite and might represent interesting metastable structures.

In section 5.5 we set up a model, based on the graph theory to analyse the networks of bonds around a magnetic atom. This model has been used to analyse the allotropes of C_{60} in a famous paper by Wales [132] revealing a distribution of energy with many deep minima separated by high barriers forming a funnel with minimum energy corresponding to the icosahedral C_{60}. Furthermore the graph theory can be related to the concept of bipartite lattices that play an important role in graphene. Also in our search we find that carbon can form a wealth of metastable disordered structures with not a high penalty in terms of energy. We aim at finding the reason why some of these realizations carry magnetic moments and may even lead to ferromagnetic behaviour.

In section 5.6 we single out only the states with sizeable magnetic moments and

analyse them in the spirit of the mean field approximation in terms of exchange energies. Most magnetic structures have antiferromagnetic order but a few of them present a hint of ferri- or ferromagnetic order. Unfortunately the LDA-CA and GGA-PBE approximations often do not agree in the evaluation of total energy and give small variations in bond lengths. Nevertheless we show that besides these disagreements result obtained in both model are qualitatively consistent.

In the last section 5.7 we focus on the most interesting samples found in our search and try to establish some recurrent features and minimal requirements for the presence of magnetic order.

Our search and analysis is certainly not exhaustive and many questions remain open but it represents a first systematic attempt to grasp the physics and bonding leading to ferri/ferromagnetism in disordered carbon structures. To invite other contributions to this fascinating topic we also give in the Appendix the structure and coordinates of the selected samples presented in section 5.7.

5.2 Procedure for the generation of disordered samples

In this section we describe how we first generate nanosized disordered samples and relax them to find (meta)stable structures and then calculate their magnetic properties. We calculate electronic and magnetic structures within the DFT [20, 21] by means of the SIESTA code which implements DFT on a localized basis set [22, 23, 24]. We used LDA with Ceperly and Alder parametrization (LDA-CA) [26, 27] and a standard built-in double-ζ polarized (DZP) [25] basis set to perform geometry relaxation. The DZP basis set represents core electrons by norm-conserving Troullier-Martins pseudopotentials [101] in the Kleynman-Bylander nonlocal form [102]. For a carbon atom this basis set has 13 atomic orbitals: a double-ζ for 2s and 2p valence orbitals and a single-ζ set of five d orbitals. The cutoff radii of the atomic orbitals were obtained from an energy shift equal to 0.02 Ry which gives a cut-off radius of 2.22 Å for s orbitals and 2.58 Å for p orbitals. The real-space grid is equivalent to a plane-wave cutoff energy of 400 Ry, yielding ≈ 0.08 Å resolution for the sampling of real space. We used k-point sampling of the Brillouin zone based on the Monkhorst-Pack scheme [103] with total 32 k-points. An iterative conjugate gradient (CG) procedure is then applied to reach stable or metastable structures. The geometries were relaxed until all interatomic forces were smaller than 0.04 eV/Å and the total stress less than 0.0005 eV/Å^3. No geometrical constrains were applied during relaxation. It is important to notice that, due to the random nature of the samples, many of them have to be metastable also after the CG minimization and, for example, after MD relaxation could reconstruct to energetically more favourable structure and change their magnetic property.

To construct structures similar to those observed experimentally [131, 8] (see Fig. 5.1a,b), we generated samples with unit cells with size 5-10 Å. To simulate the exper-

imental conditions of high pressure we used geometries compressed up to 45% of their equilibrium size. According to our calculations by DFT with the SIESTA code the initial structures have an internal pressure of 2000-6000 kBar.

To compensate the high internal stress, the CG relaxation leads to drastic changes of the initial structure. In this way, the minimization procedure gives a chance to reach different high energy metastable configurations with the possible presence of magnetic states, similar to the situation observed experimentally for carbon nanofoams (Fig. 5.1a,b).

Table 5.1: Number of magnetic samples with total (absolute) spin polarization m (m_{abs}) calculated using equations (5.4) corresponding to a set of magnetization intervals in μ_B.

N_{atoms}	$N_{samples}$	$m(m_{abs}) > 0.01$	> 0.05	> 0.10	> 0.25	> 0.5	> 1.0
5	1000	22(23)	22(23)	21(22)	2(2)	2(2)	0(0)
6	1000	0(0)	0(0)	0(0)	0(0)	0(0)	0(0)
7	1000	26(26)	26(26)	26(26)	14(14)	14(14)	0(0)
8	10000	7(7)	3(7)	3(4)	1(2)	0(1)	0(1)
9	1000	7(9)	7(7)	6(6)	3(3)	3(3)	0(0)
10	4000	27(27)	27(27)	26(26)	22(23)	16(18)	0(0)
11	1000	6(6)	6(6)	6(6)	5(5)	3(3)	0(0)
12	1000	14(15)	13(14)	12(13)	9(11)	3(7)	0(2)
13	1000	11(13)	10(11)	10(11)	8(9)	6(7)	1(3)
14	1000	15(15)	13(14)	12(14)	11(13)	7(12)	0(2)
15	1000	16(16)	15(16)	14(16)	12(15)	10(15)	1(2)
16	1100	28(28)	24(28)	22(27)	18(25)	13(21)	0(5)
24	100	4(4)	4(4)	4(4)	4(4)	3(4)	0(0)
64	100	5(13)	3(9)	3(8)	3(8)	3(8)	3(8)

To generate the initial geometries we used the following approach. First of all, we calculate the volume per atom in the graphite unit cell:

$$v_{atom}^{graphite} = \frac{3\sqrt{3}}{4} r_{cc}^2 r_{ll} \tag{5.1}$$

where $r_{cc} = 1.42$ Å is the carbon-carbon interatomic distance in the layer and $r_{ll} = 3.35$ Å is the interlayer distance in graphite. Since we will construct compressed unit cells by scaling of the coordinates, it is convenient to express r_{ll} in terms of r_{cc}. For graphite $r_{ll} = 2.36\ r_{cc}$. In this way, the volume $v_{atom}^{graphite}$ can be written as proportional to r_{cc}^3 and $\sqrt[3]{v_{atom}^{graphite}}$ becomes proportional to r_{cc}. Rescaling the unit cell size by r_{cc}^{custom} we can construct the initial cubic unit cell for a given number of atoms $N_{atoms} = n$ with lattice constant a as

$$a = \frac{\sqrt[3]{n v_{atom}^{graphite}}}{r_{cc}} r_{cc}^{custom} \tag{5.2}$$

To allocate the required number of atoms within the prepared cubic unit cell we randomly generated atomic coordinates. If the newly generated position is closer than r_{cc}^{custom} to any atom we replaced such a pair by one atom with average position. At the end, the geometry has such a property that any two atoms are not closer than r_{cc}^{custom}. For the case $r_{cc}^{custom} = 1.42$ Å the density of the generated system is equal to the one of graphite. We used $r_{cc}^{custom} = 1.1$ Å that gives a density ≈ 2.15 higher than graphite.

To calculate the density of graphite using (5.1) we use the equation:

$$\rho = \frac{\mu_{carbon}}{N_{Avogadro} v_{atom}^{graphite}} \tag{5.3}$$

where $\mu_{carbon} = 12.01$ g/cm^3 is a molar mass of carbon.

Table 5.2: An overview of the obtained information about coordination in all studied configurations. The percentage of samples with specific coordination is shown for each series of atoms. Since the case of 6-sp^2 is not applicable to the series with 5 atoms and it duplicates the value of all-sp^2 configurations for the series with 6 atoms we keep these two cells empty.

N_{atoms}	$N_{samples}$	all-sp^2	2-sp^2	4-sp^2	6-sp^2	all-sp^3	1-sp	2-sp	3-sp
5	1000	0.0	15.4	38.1	-	46.4	17.8	0.0	1.3
6	1000	33.2	32.4	25.0	-	9.3	7.3	4.9	0.0
7	1000	0.0	30.8	19.1	32.2	17.3	8.1	0.2	0.0
8	10000	22.7	22.0	23.6	9.0	22.4	1.5	0.4	0.0
9	1000	0.0	25.6	31.3	14.3	17.2	1.8	0.1	0.0
10	4000	10.2	22.5	22.5	24.1	11.3	2.5	0.6	0.05
11	1000	0.0	23.0	29.6	19.9	12.8	3.2	0.5	0.2
12	1000	4.6	21.1	24.7	16.7	12.8	1.8	0.3	0.0
13	1000	0.0	24.1	24.1	19.5	7.1	3.0	0.5	0.0
14	1000	2.0	17.3	21.8	23.9	6.5	2.6	0.4	0.0
15	1000	0.0	18.0	21.6	22.8	6.5	4.5	1.3	0.0
16	1100	1.2	16.3	21.5	20.7	7.5	4.5	0.3	0.2
24	100	0.0	4.0	11.0	21.0	0.0	6.0	3.0	0.0
64	100	0.0	0.0	0.0	0.0	0.0	11.0	4.0	1.0

Such a randomly generated geometry with high internal pressure and constrains on the number of atoms per unit cell is then minimized by CG letting the atomic positions within the cell and the cell lattice parameters vary. We then study each sample to search for magnetic states in pure carbon materials. We have studied in this way 24300 samples. A first screening gives $\approx 1\%$ (see Table 5.1) of the samples with magnetic states and different type of coordination (see Table 5.2). In Table 5.2 we analyse the coordination in samples with 5 to 64 atoms in the unit cell.

In the following we use the following notation to refer to a specific sample, namely ACxx-yyyy where AC stays for amorphous carbon, xx is the number of atoms in the unit cell and yyyy denotes a specific sample. As an example, the sample AC07-0010 shown in Fig. 5.9 is the tenth of a series with 7 atoms in the unit cell.

69

We see that also samples with only sp^2 or sp^3 bonding are found. Their number decreases for the larger unit cells as expected because there are many more possible configurations. We find, as expected from considerations that will be discussed in section 5.5, no samples with all-sp^2 atoms for odd N_{atoms}. Unexpected is that for $N_{atoms} = 8$ there is a maximum number of all-sp^3 samples. For the samples with mixed bonding we report the percentage of samples with 2, 4 or 6 sp^2 bonded atoms. Within the many possible configurations, we distinguish those with all-sp^2 atoms (graphite-like structure), all-sp^3 atoms (diamond-like structure), configurations with two-fold coordinated atoms and mixed configurations with different percentage of sp^2/sp^3 atoms. The two first groups (all-sp^2 and all-sp^3) are non magnetic and the last two groups are possible candidates for magnetic states as it will be discussed in more details in section 5.5.

To distinguish between ferromagnetic and antiferromagnetic samples we use the total spin polarization m calculated as a sum of magnetic moments over all atoms and the total absolute spin polarization m_{abs} calculated for absolute values of atomic magnetic moments in the following way:

$$m = \sum_{i=1}^{N_{Atoms}} s_i, \quad m_{abs} = \sum_{i=1}^{N_{Atoms}} |s_i|, \quad s_i = q_i^{up} - q_i^{down} \tag{5.4}$$

where q_i^{up} - charge corresponding to spin "up" at the i-th atoms, q_i^{down} - charge corresponding to spin "down" at the i-th atoms. (see section 1.5 in the introduction for more details).

Such equations allow to detect both antiferromagnetic samples, where the value $m = 0$ and $m_{abs} \neq 0$, and ferromagnetic ones for which $m = m_{abs}$. Moreover we found a set of samples where $m > 0$ and $m \neq m_{abs}$. This is a sign of ferrimagnetic properties.

5.3   Search of magnetic states

To identify the geometrical structures responsible for the magnetic states, we perform a numerical experiment based on a *generate and test* approach [133] with elements of genetic algorithms [134]. Such a method is convenient in view of the available large amount of computational facilities which allows to calculate automatically thousands of independent configurations. We varied the number of atoms together with the unit cell size and number of configurations in the computational series iteratively to identify the most typical geometrical structures carrying magnetic states.

We started with 64 atoms per sample and 100 samples in the series. We found 5 configurations with total spin polarization $m > 0.010\mu_B$ and only 3 with $m > 0.500\mu_B$, (see Table 5.1 last row) where m is expressed in (5.4). At the same time, from Table 5.1 we see that within the series with 64 atoms besides the samples with sizeable total spin polarization m there are a number of samples (i.e. 8-3=5 samples) where m is small

while m_{abs} is of the order of μ_B. This facts is a clear evidence of antiferromagnetic arrangement of magnetic moments in the ground state as discussed at the end of section 5.2.
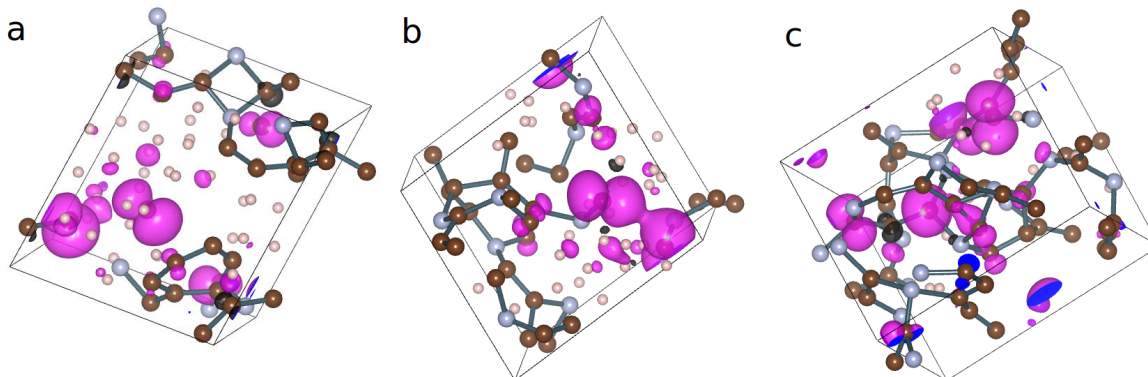
Figure 5.2: Examples of spin polarized structures for disordered carbon (64 atoms per unit cell) after relaxation, showing atoms with magnetic states (pink clouds) surrounded by nonmagnetic ones. The atoms in sp^3 hybridization are small balls marked by light gray, the atoms in sp^2 hybridization are balls marked by brown. The atoms in sp^3 hybridization having sp^2 neighbours are balls marked by gray. The 1D chains of sp^2 atoms separated by single sp^3 atoms are marked by bonds. Here we see well distinguishable networks made of 1D sp^2 chains. We see that not all the magnetic atoms belong to sp^2 chains. The geometry is visualized by the VESTA program [36].

A first analysis shows that magnetic moments are carried by individual atoms in specific atomic configurations. We used an automated procedure to detect different types of hybridization based on the number of neighbours within a radius of 1.8 Å. Typical configurations with magnetic atoms are shown in Fig. 5.2a,b,c. We have highlighted the presence of networks of sp^2 atoms. We will come back to the relation between these networks and the magnetic atoms in section 5.5.

One might have expected the source of uncompensated spin to be dangling bonds originating from 2-fold carbon atoms as it was shown for grain boundaries in [135]. We find instead that also 3-fold carbon atoms may have uncompensated spin and that this latter case occurs at least one order of magnitude more frequently than 2-fold atoms. While for 2-fold coordinated atoms the magnetic moment is clearly related to a dangling bond, the situation of 3-fold coordinated atoms is more complex. Depending on the bond angles, it may correspond to a planar sp^2 configuration like in graphite or to a sp^3 configuration with a dangling bond as found for instance at the ideal (111) diamond surfaces.

At the same time, within the first series of samples with 64 atoms we have shown that only 3 configurations have more than one magnetic atom. This suggests that probably the geometrical conditions which make atoms magnetic can be detected based on smaller and simpler geometries with fewer atoms per unit cell. To do so we iteratively reduced the number of atoms together with the unit cell size.

In the second series with 100 configuration and 24 atoms per sample we found 4 configurations with total spin polarization $m > 0.005\mu_B$ and only 3 with $m > 0.500\mu_B$. Typically, we had 1-2 magnetic atoms per unit cell.

In view of the small number of magnetic atoms in each sample, to make our search for structures with magnetic states more efficient we have increased the total number of configurations in the series up to few hundreds and varied the number of atoms in the unit cell. We generated and optimized series of thousands of configurations with 16 to 5 atoms per unit cell. Let us notice first a few interesting facts. First of all, we did not find any magnetic configurations within 1000 samples in the series with 6 atoms per unit cell and only 3 magnetic configurations with $S > 0.100\mu_B$ within 10000 samples in the series with 8 atoms per unit cell. The series with 5 and 7 atoms per unit cell instead present magnetic configurations. This could be a sign of the importance of the parity of the number of atoms in the unit cell.

By reducing the number of atoms per unit cell we also reduce the number of possible relaxed configurations. This reduction is reflected in the presence of duplicate geometries up to variations in the directions of the unit cell vectors. The presence of duplicate geometries also suggests that, within the constraints imposed by the sample construction, such geometries are more preferable than the others.

5.4   Energy and magnetism

Within thousands of calculated configurations with formation energy lying between 0.0 and 2.0 eV/atom above diamond, as shown in Fig. 5.3 a few hundreds magnetic ones were found with different energies and spin polarizations. We note in passing that, besides diamond and graphite there is another sharp peak at low energy. Since these configurations are not magnetic we do not discuss them here and they will be the subject of the future studies. In Fig 5.4 we analyse the relation between formation energy and magnetic moments. The total energy per atom for magnetic configurations lies in a relatively restricted range of 0.6-1.5 eV/atom above diamond and graphite, most of them being in 0.8-1.2 eV/atom energy range. Also we see that in general we cannot identify any specific energy-spin region for particular series of calculations excluding the series with 7 atoms per sample (see top polygon in Fig. 5.4) and partly the series with 10 atoms per sample (see middle polygon in Fig. 5.4). The presence of duplicates, especially for the series with 5-11 atoms that we have already discussed in 5.3, is indicated by ellipses. Low energy configuration are indicated by rectangles and we see that they cluster in the two regions indicated by shaded polygons for energy $\leq$ 0.8 eV/atom.

As mentioned in the introduction, we see that there are many metastable configurations at energies relatively low (only 10-15 % higher than diamond and graphite). The special character of the energy landscape of carbon systems, related to the fact that carbon can form a wealth of structures, often with very high energy barriers among

Table 5.3: Comparison of the 6 computational models used to calculate the formation energy of 5 carbon allotropes, i.e. 3 sets of parameters within GGA-PBE and 3 sets of parameters within the LDA-CA approximation. Here E_{mesh} gives the resolution for the sampling of real space based on the plane-wave cutoff energy. E_{cutoff} is the cutoff radius of the atomic orbitals. (see section 5.2) Two types of basis sets were chosen: the standard DZP and the custom one constructed for graphitic materials using the approach described in [25, 136]. Notice that the minimal energy structure is graphite for GGA-PBE and diamond for LDA-CA.

GGA-PBE, 32 k-points	DZP	DZP	custom
$E_{mesh} = 400$ Ry	$E_{cutoff} = 1$ mRy	$E_{cutoff} = 20$ mRy	basis
diamond	0.021	0.008	0.112
graphene	0.007	0.066	0.003
graphite-A	0.002	0.015	0.001
graphite-AB	0.000	0.001	0.000
graphite-ABC	0.001	0.000	0.001
LDA-CA, 32 k-points	DZP	DZP	graphite
$E_{mesh} = 400$ Ry	$E_{cutoff} = 1$ mRy	$E_{cutoff} = 20$ mRy	basis
diamond	0.000	0.000	0.000
graphene	0.195	0.257	0.079
graphite-A	0.173	0.166	0.059
graphite-AB	0.156	0.131	0.044
graphite-ABC	0.157	0.132	0.044

them, has been pointed out in the seminal work of [132] where all the 1812 possible structures of C_{60} are shown to form a funnel of well separated, deep minima not too far in energy from the absolute minimum corresponding to icosahedral C_{60}.

5.5 Structure and magnetism

As we have seen in the previous section, magnetic structures are rare and the relation between structure and magnetism is certainly not trivial. We try and use the graph theory [137] to relate structure and magnetism. To take advantage from this theory we need to have only one odd numbered coordination. This is realized in our carbon system where no atoms with one bond or five bonds are present because such a configuration is especially unstable and was never observed in our calculations.

We start by a lemma that we have derived ourselves although it might be reported already in the literature.

Lemma. Any connected graph with nodes having 2, 3 or 4 neighbours always has an even number of nodes with 3 neighbours.

Proof. Suppose we have N_2 nodes with 2 neighbours, N_3 nodes with 3 neighbours and N_4 nodes with 4 neighbours. Each edge connects two nodes. Due to this fact,
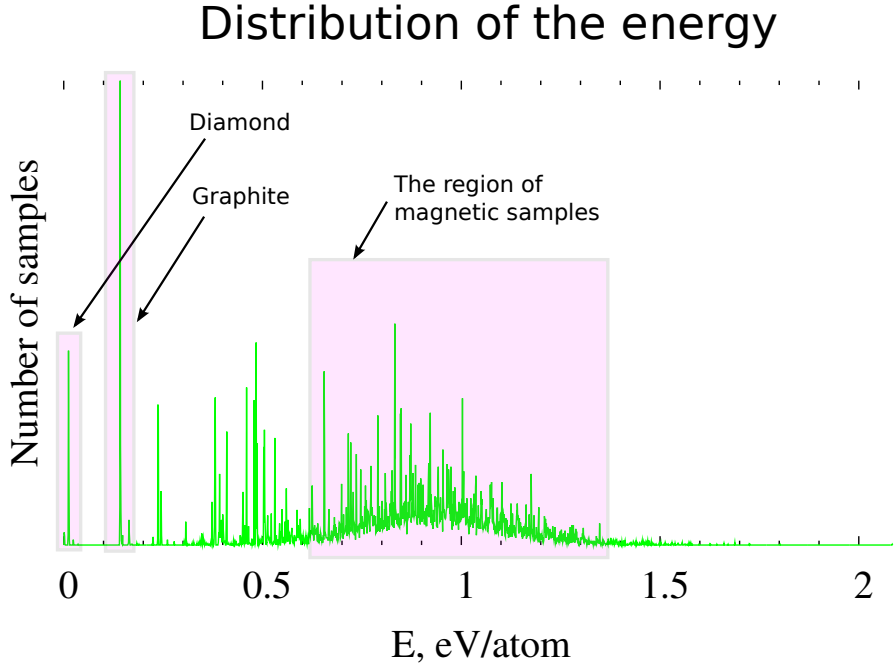
**Figure 5.3:** Distribution for the energy referred to diamond of all the calculated samples. The energy intervals marked as "diamond" and "graphite" corresponds to the specified systems, the third shaded energy interval contains magnetic samples and is further analysed in Fig. 5.4.

the total number of edges in the graph is $(2N_2 + 3N_3 + 4N_4)/2 = M$, where M is an integer positive number, whence $3N_3 = (2M - 4N_4 - 2N_2) = 2(M - 2N_4 - N_2)$. This means that $3N_3$ is an even number. In fact, since 3 is odd, the multiplication $3N_3$ can be even only if N_3 is even.

The structure of the graph described in the lemma corresponds to the structure of disordered carbon where we have atoms with either 2, 3 or 4 neighbours. This case corresponds either to atoms in sp, sp^2 and sp^3 hybridization or atoms in sp^2 and sp^3 hybridization with dangling bonds (2 and 3 neighbours respectively).

The importance of this lemma lies, as it will be shown later, in the relation between magnetic states and the presence of atoms in sp^2 hybridization. Based on our calculations, we usually observe a non compensated spin located at atoms in sp^2-hybridization with 3 neighbours and an unpaired π-orbital. Another important observation is that sp^2 atoms usually group in network structures made of 1D chains of sp^2 atoms as shown in Fig. 5.2. Such a structure may be represented as a bipartite graph. Graphene has a 2D bipartite unit cell [1]. An example of a graph representation for graphene is shown
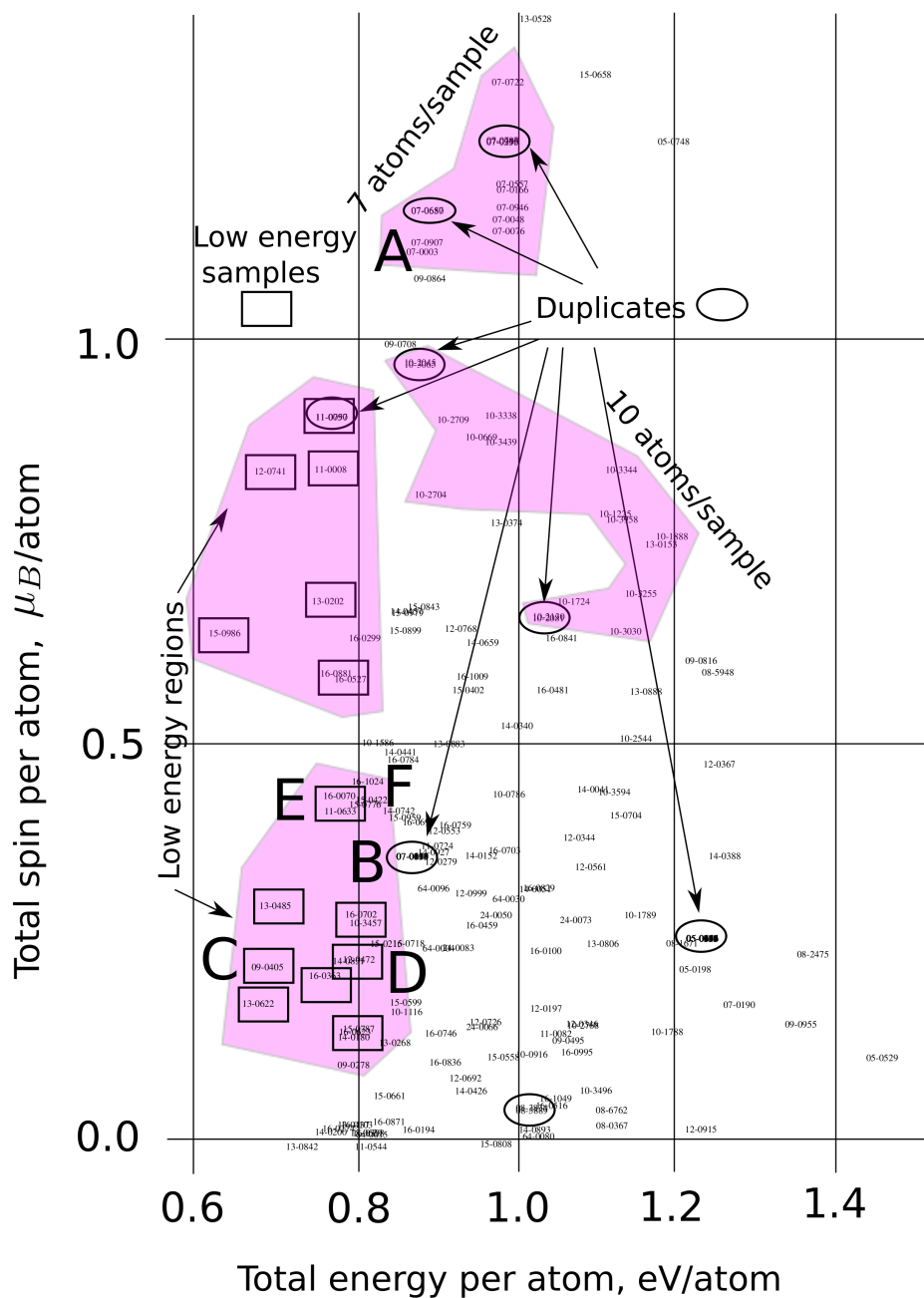
Figure 5.4: Total spin per atom as a function of total energy per atom (referred to diamond) for magnetic structures. Each point has a name combining the number of atoms and index in the series. Few regions of spin and energy are marked by light gray polygons. Within them, ellipses indicate the existence of many duplicates as described in the text. The two left shaded regions contain low energy structures marked by rectangles. The structures indicated as A, B, C, D are shown in Fig. 5.10, 5.9, 5.11 right and 5.11 left respectivelly.
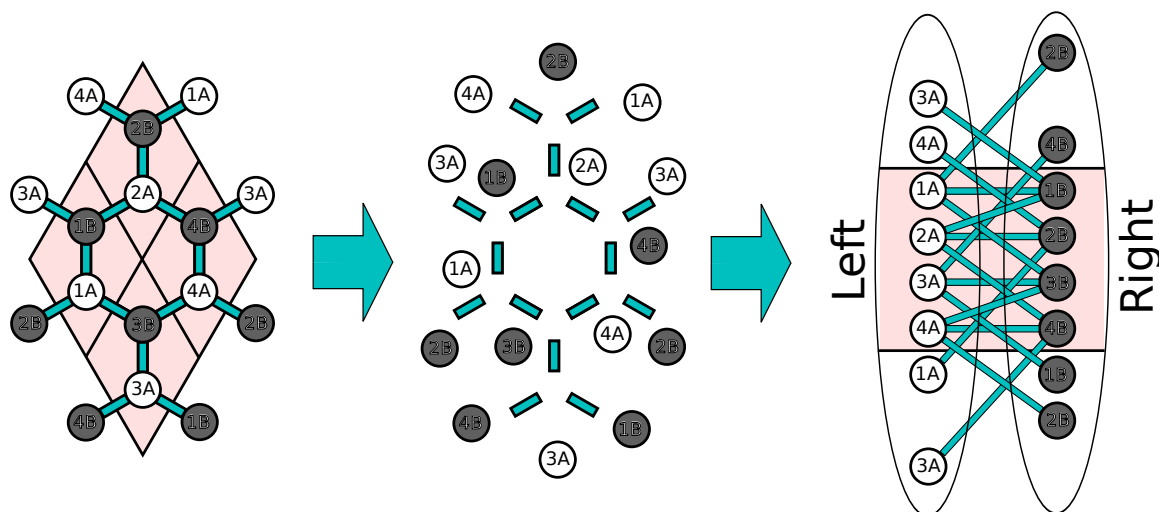
Figure 5.5: An example of the division procedure that maps the bipartite lattice of graphene into two disjointed subgraphs called as Left and Right. From left to right: a 2X2 supercell of graphene indicated by the light gray polygons. Atoms belonging to the A-sublattice (B-sublattice) are represented by white (gray) balls with labels 1A(B), 2A(B), 3A(B), 4A(B). Since we consider 2D periodical structure we also show the periodical images outside the unit cell. Through an intermediate step we can construct the Left and Right subgraphs as indicated.
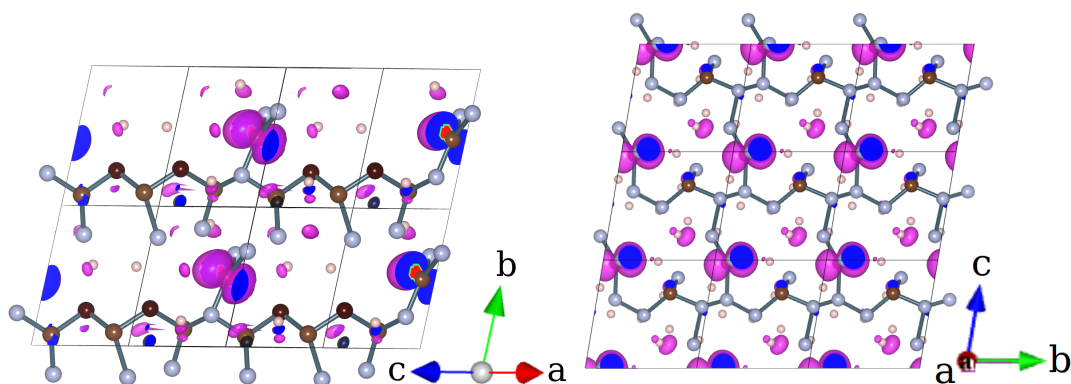
Figure 5.6: sp^2-sp^3 1D chain (left) and 2D-network (right) examples. As previously (see Fig. 5.2) for better representations we use different colours for atoms in sp^2 and sp^3 hybridization having different neighbouring atoms.

in Fig. 5.5. According to the Lieb theorem [138, 91, 113] we can expect the presence of nonzero spin if the number of atoms in the Left and Right subgraphs is different. But according to the above lemma, we always have an even number of atoms with 3 neighbours so that most structures will have the same amount of atoms in the left and right subgraphs. As a result, to have magnetic states, we need specific geometric structures. For example, in the simplest case, the source of uncompensated spin could be a single sp^2 atom surrounded by sp^3 atoms. But, according to the lemma, we will always have at least one more sp^2 atom located somewhere in the unit cell. If these two atoms are either in different subgraphs or form a bond, no magnetic states may be expected.

One straightforward consequence of the above considerations is that the absence of sp^2 atoms in the unit cell, i.e. a fully sp^3 structure, means the absence of any magnetic states. Within 24300 optimized configurations we have 4132 fully sp^3 structures and all of them are non magnetic.

Since sp^2 atoms are the crucial ingredient to have magnetic states, we analyse our samples by evidencing the connections between sp^2 atoms. In this way we identify networks of bonds between them, as shown in Fig 5.2a,b,c and more in detail in Fig 5.6. To make the network of sp^2 atoms more evident we have marked the sp^3 atoms with tiny balls so that the remaining geometry looks like a 3D network of 1D chains of sp^2 atoms. Such a 3D network may consist of a set of isolated clusters or may form an infinite structure due to the periodic boundary conditions in any or all directions of the unit cell.

Let us now consider one of the simplest cases where we can expect magnetic states on the basis of the lemma: two sp^2 atoms not bonded to each other within the unit cell. We can automatically detect all such configurations. Within 24300 we found 990 samples with only two 3-fold atoms not bonded to each other where 34 of them have appreciable magnetic moments in ferro- or ferri- or antiferromagnetic configurations ($m > 0.020 \ \mu_B$ or $m_{abs} > 0.020 \ \mu_B$). For completeness, we give the distribution of magnetic samples within each series: 8:1, 9:1, 10:6, 12:6, 13:3, 14:5, 15:4, 16:8 (N_{atoms}:$N_{samples}$) where 3 of them are with $m < 0.020 \ \mu_B$ and $m_{abs} > 0.020 \ \mu_B$, 20 of them are with $m \approx m_{abs}$ and other 11 with $m_{abs} > m$.

In all 34 structures the distance between the 2 sp^2 atoms > 2.19 Å. Since we use a localized basis set with cut-off radius and the standard set of parameters which give the cut-off radius of s orbital 2.22 Å (see description in section 5.4) we did one check with longer cut-off radius for one similar sample. For smaller cut-off energy which gives $r^{2s}_{cut-off} = 3.07$ Å and $r^{2p}_{cut-off} = 3.84$ Å we get practically the same value of m for the fully relaxed geometry, ruling out the possibility of a numerical artefact. The requirement of a minimal distance of 2.19 Å between 3-fold coordinated atoms gives 613 samples instead of 990, increasing the percentage of magnetic samples to $\approx 5.5\%$.

Within all 613 samples, we found that the 2 sp^2 atoms have either 0, 1 or 2 common neighbours but we could not find any correlation between the number of common neighbours and the presence of magnetic states. We notice, however, that the presence of 2 common neighbours means that two 3-fold coordinated atoms form a tetragon.
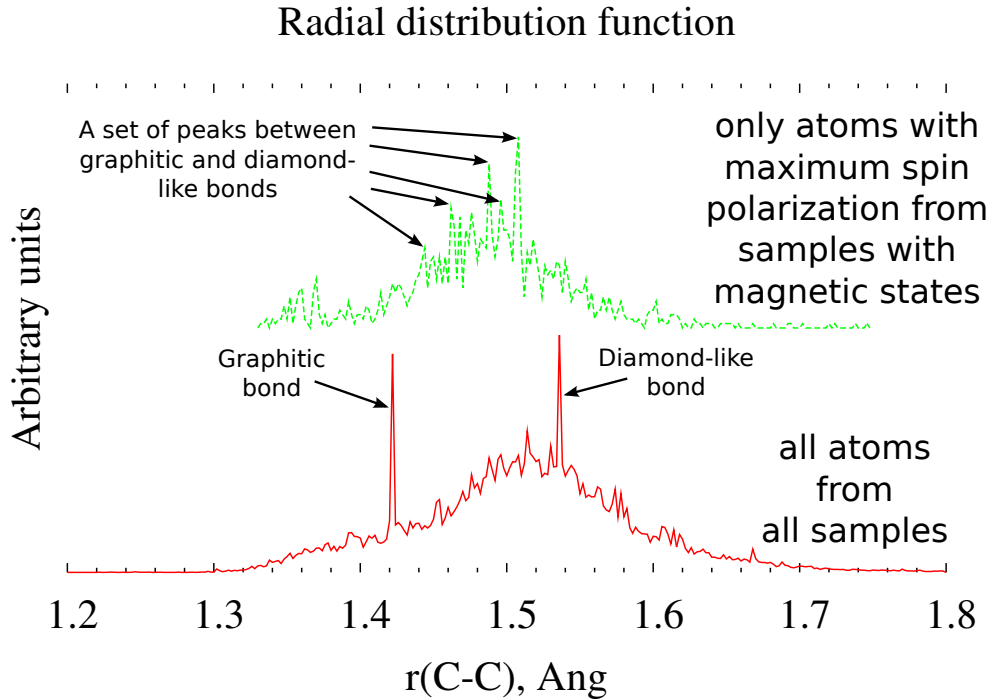
Figure 5.7: Comparison of the radial distribution functions calculated for all atoms of all 24300 optimized samples with that calculated by considering only the atoms which carry maximal magnetic moment.

Interestingly, such a situation was found 4 times for the 34 samples with a magnetic state, a relatively high percentage.

The above analysis was performed to identify some general geometrical configurations leading to magnetism starting from the simplest possible situation. Our analysis accounts then for only 34 of the total 202 structures with magnetic moments. Nevertheless we have seen that the local environment, namely the interatomic distances and coordination of the atoms carrying a magnetic moment, plays a role. A way to further investigate this point is to compare the radial distribution function (rdf) of magnetic atoms with all others as we do in Fig. 5.7. If we average over all atoms of all 24300 studied configurations, the rdf presents two sharp peaks at the interatomic distance of graphite (1.42 Å) and diamond (1.54 Å) and a broad distribution around them from $\sim$ 1.32 Å to $\sim$ 1.7 Å. If we consider only the atom with maximum (non-zero) magnetic moment within each sample, we find that the two sharp peaks disappear, in agreement with our discussion that rules out the possibility of magnetism for atoms with only

graphitic (fully sp^2) or only diamond(fully sp^3) bonds. We see instead a number of peaks in between these two distances that have to be related to a mixed bonding. We notice that a few peaks are rather pronounced but we did not manage to assign each of them to a specific bonding configuration.

In this chapter we have tried to find out the most promising configurations giving rise to magnetism. As we have discussed the minimal conditions to have magnetic moments are very stringent and lead to a very small percentage of magnetic structure among the thousands studied. Nevertheless some exist and, as we show in the next section 5.6, could lead to magnetic order if suitably repeated. Moreover, since our analysis only gives a first insight in this phenomenon, we examine in detail in Section 5.7 the structure of the most interesting realizations found in our quest.

5.6 Exchange energy

In this section we focus on the samples with atoms carrying a magnetic moment and examine the possibility of magnetic order in the spirit of mean field theories.

The samples we studied have mostly orthorhombic unit cells with lattice vectors a, b and c where all three periodic directions are different (i.e. anisotropic crystal). If the unit cell has only one atom with magnetic moment much larger than the others, we calculate the exchange energy J for each periodic direction separately. To do so, we double the original unit cell in the chosen direction and initialize the spins on the two magnetic atoms as "up" and "down" in the first and second periodic images respectively and calculate the total energy which we call here E_{AFM}. By initializing the spins on the two magnetic atoms as "up" and "up" we calculate the total energy E_{FM}. From these two values we calculate the mean field parameters (exchange energy) as

$$J = \frac{E_{AFM} - E_{FM}}{2} \tag{5.5}$$

Since we have three independent values of J calculated for unit cells doubled in the direction of the a, b and c lattice vectors, we call them here as J_a, J_b and J_c. In order to automatize the evaluation and ordering of J even though we do not have a priori any knowledge of the studied geometry we use the following procedure. We start by taking only the samples which have at least one positive value among J_a, J_b, J_c. Then, for the chosen sample, we sort the values of J_a, J_b, J_c in descending order. The sorting breaks the relation with the a, b and c vectors so that we rename the sorted values as J_1, J_2, J_3 where J_1 is always positive and $J_1 \geq J_2 \geq J_3$. Finally we group all the chosen samples, sorting them by J_1 in descending order and make the plot shown in Fig. 5.8.

We have to note that, particularly for the large samples, and in any case in view of the large number of studied samples, we could not study the stability of the magnetic samples with respect to temperature. We could only perform the conjugated gradient
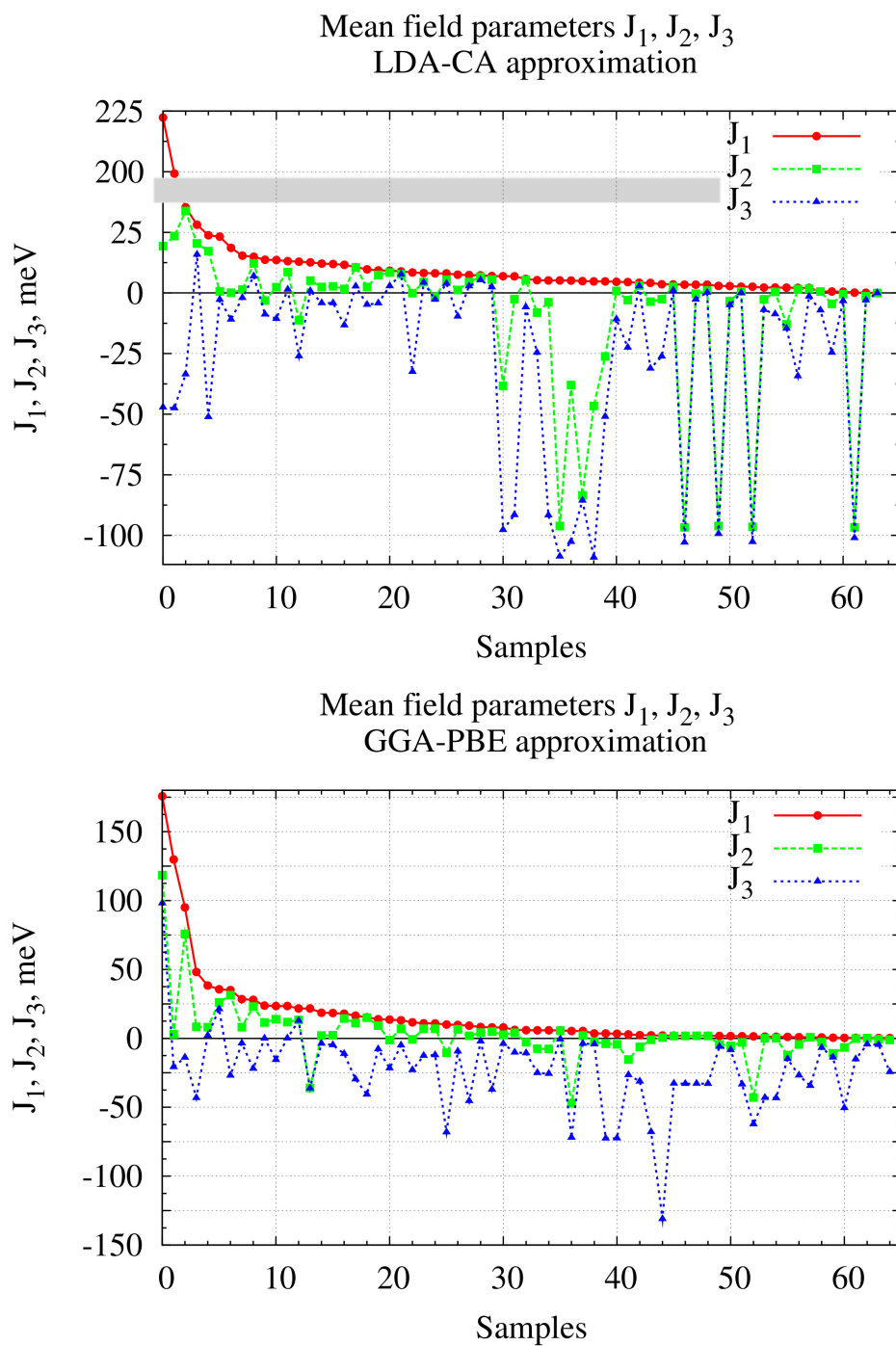
Figure 5.8: Mean field parameters J_1, J_2, J_3 calculated using equation (5.5) in 3 periodical directions sorted by the automatic procedure described in the text. Two approximations were used, i.e. LDA-CA (top panel) and GGA-PBE (bottom panel). Notice the cut in the Y axis of the top panel.

optimization for the doubled cells. Both configurations with parallel and antiparallel orientation of magnetic moments were checked in this way.

The first 10 points in Fig. 5.8 with the highest values of J in LDA-CA approximation, correspond to the following samples: AC07-0657, AC07-0680, AC07-0003, AC16-0070, AC07-0907, AC14-0388, AC14-0742, AC12-0367, AC15-0776, AC16-1024. The first 10 points in GGA-PBE approximation correspond to the samples AC14-0831, AC07-0907, AC15-0656, AC13-0119, AC15-0267, AC10-1116, AC07-0003, AC09-0394, AC07-0657, AC09-0027. Only the two samples AC07-0657 and AC07-0907 are among the first 10 in both approximations. Beside two these samples, the sample AC14-0831 has, in both approximations, a positive value of all three J's. Unfortunately, as expected, the LDA-CA and GGA-PBE approximations often do not agree, especially for such a complicated case as disordered carbon where changes in the bond length up to 2-3% can dramatically change the geometry and electronic properties. In contrast to plane geometries, like the graphene grain boundaries examined in [135], these 3D, disordered geometries usually do not have any symmetry that can compensate small variations in the bond length. Despite these shortcomings, two samples with the highest values of J are present in both approximations. This fact serves as evidence of a qualitative agreement between the two used approximations.

After these considerations on the qualitative applicability of the used approximations, we can draw some conclusions based on the important physical observations found in these calculations. First of all, the only few samples that have all three values of J positive, making it possible to expect 3D ferromagnetism, have very small values of J only up to few meV. This finding agrees with the fact that 3D ferromagnetism has been experimentally observed in carbon nanofoams only up to 90 K.

Most samples have two positive values of J (see Fig. 5.8) making it possible to have 2D lattices of magnetic moments with ferromagnetic arrangement. In some cases the values of J are rather large and might lead to high Curie temperature. Since, in 2D ferromagnetic order can exist, we pay special attention to this important case. When the third value of J is negative, the system has antiparallel coupling of 2D ferromagnetic networks. To exclude this effect and have only ferromagnetic couplings, we have to separate the 2D networks by imposing additional geometrical constrains. In Fig. 5.11 we show how this could be realized by creating 2D grain boundaries which naturally appear during growth of 3D crystals. Such a geometrical isolation of 2D structures could lead to ferromagnetic order in a bulk 3D system. In the next section 5.7 we discuss the geometry of the most promising structures, namely those with high values of the J parameters.

5.7 Examples of magnetic structures
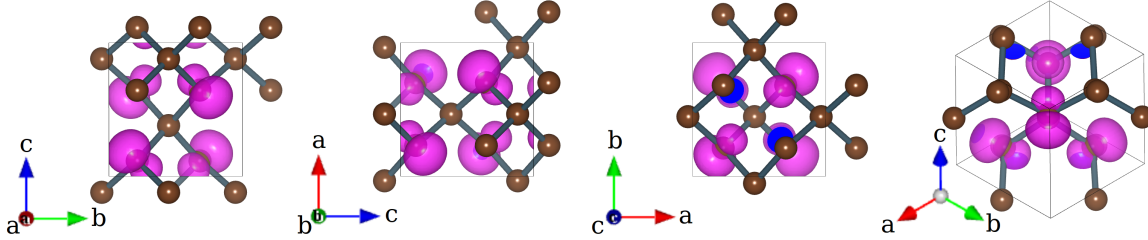
Figure 5.9: Spin density isosurface plot and unit cell of the sample AC07-0010 shown (from left to right) in the plane orthogonal to the 100, 010, 001 and 111 directions. This structure occurs 11 times in a set of 1000 samples.

Here we show a few geometrical examples discovered in our search which could be important from different points of view. Out of many and many different geometries within the series with small number of atoms, we will pay attention to the samples AC07-0003 and AC07-0010 (marked as A and B in Fig. 5.4). Sample AC07-0003 has high values of two J parameters (see top-10 list in the text related to Fig. 5.8) and was found several times with small variations in geometry and sample AC07-0010 has a highly symmetric geometry with 4 sp^2 atoms with magnetic moments and appeared 11 times.

Also we will pay attention to two samples, AC09-0405 and AC14-0831 (marked as C and D in Fig. 5.4), due to their low formation energy (left filled region in Fig. 5.4, relatively simple structure, similarity to the geometry of graphite and ferromagnetic arrangement of magnetic moments.

Finally we briefly discuss two more complicated structures, AC09-0708 and AC15-0267, which have 3D ferromagnetic properties according to the GGA-PBE approximation.

An example of a 3D bipartite unit cell is presented by the sample AC07-0010 shown in Fig. 5.9. Its structure can be described by considering a sequence of steps starting from a face-centered cubic cell. Taking into account all 6 atoms sitting at the center of each face of the unit cell, we can construct an octahedron with 6 vertexes and 8 faces. Within the 8 faces, we can choose 4 ones in such a way that any two of them have no common edge. Putting 4 atoms at the center of the 4 chosen faces of the octahedron together with the original 3 atoms sitting at the faces of the cubic unit cell would finally produce our geometry. The final structure has 7 atoms where 3 of them are 4-fold coordinated in sp^3 hybridization and 4 atoms are 3-fold coordinated in sp^2 hybridization. Each of the 4 sp^2 hybridized atoms carries a magnetic moment shown as a pink cloud in Fig. 5.9 and contributes the value $m_C = 0.061$ μ_B to the total spin polarization. The geometry has 3+4=7 atoms and (3x4+4x3)/2=12 bonds each of them of 1.51 Å, corresponding to a peak in the rdf of magnetic atoms in Fig.
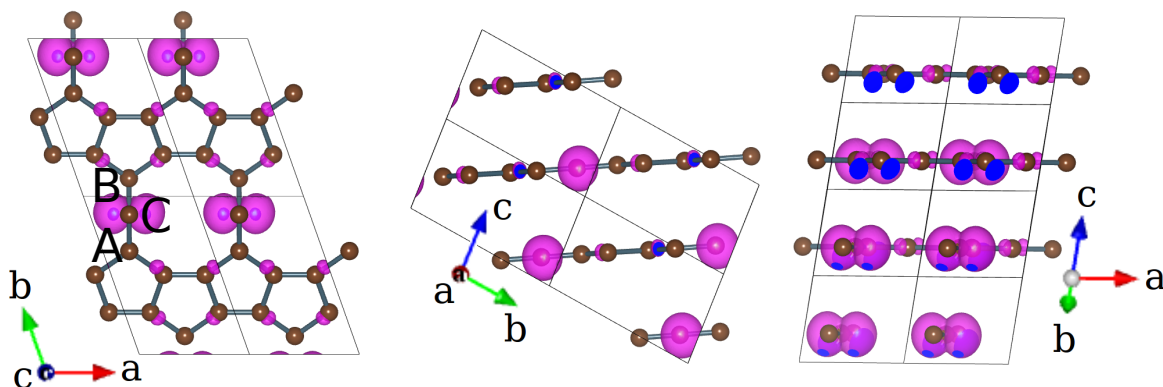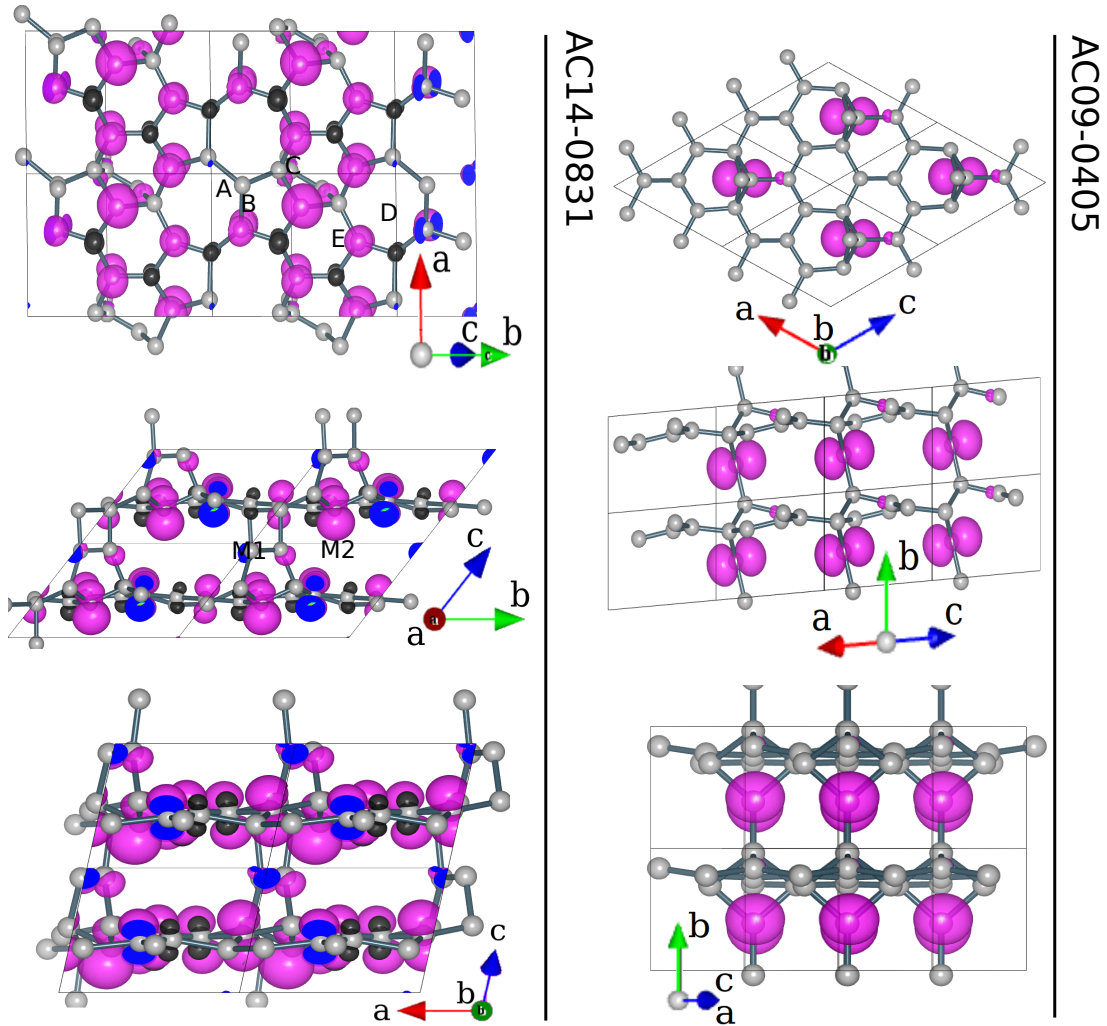
Figure 5.10: Spin density isosurface plot of the sample AC07-0003. Top, side and front views.

5.7. This structure presents a frequently occurring pattern where a 3-fold coordinated carbon atom in the sp^2 hybridization is surrounded by 3 sp^3 atoms. In Fig. 5.5) we have seen that graphene has a 2D bipartite unit cell with one atom in the Left and one in the Right subgraphs. The sample AC07-0010 has a 3D bipartite unit cell with 4 sp^2 atoms in the Left and 3 sp^3 atoms in the Right subgraph. This situation is similar to the structure of half hydrogenated graphene [139] where only the carbon atoms on one sublattice are sp^3 bonded to a hydrogen. Exactly this feature allows us to apply the Lieb theorem [138, 91, 113] and expect non zero total spin polarization in agreement with the result of our DFT calculations.

The magnetic states in the sample AC07-0003 shown in Fig. 5.10 are related to the presence of dangling bonds on two-fold coordinated carbon atoms labelled as C in the left panel of Fig. 5.10. Beside the rather high values of two mean field parameters J's (see Fig. 5.8 and text), such a structure has another interesting geometrical property. In Ref. [56], the energy of several types of edges was considered and the reconstructed 5-7 zigzag edges with pentagons and heptagons were found to have the lowest energy. Also other types of reconstructed edges were studied and the armchair 5-6 (pentagon-hexagon) structure was found to have not much higher energy than the lowest. The reconstructed 5-6 armchair edge is a structure which can be used to construct the geometry of the sample AC07-0003. To do so we have to take two armchair 5-6 edges and connect them together using two two-fold coordinated atoms from the pentagons on each edge (atoms A and B in Fig. 5.10 left) with the addition of an intermediate carbon atom labeled as C. Such a junction saturates all dangling bonds of atoms A and B while keeping an unpaired electron on atom C. The sample AC07-0003 is made of a stacking of such 2D planes with magnetic atoms. One could describe this structure as a graphite lattice where the planes contain grain boundaries with two-fold atoms carrying magnetic moments.

Another family of structures which can be seen as modifications of the graphite structure is represented by the two samples AC09-0405 and AC14-0831 both shown in Fig. 5.11. The first one, AC09-0405, has a graphite-like structure made of two graphene

Figure 5.11: Spin density isosurface plot of AC09-0405 and AC14-0831 samples. For better representativity the unit cell of AC14-0831 was rotated in such a way to put two of the lattice vectors along the graphene plane.

planes separated by an interplane distance $d_{ll} = 3.17$ Å (to be compared to 3.35 Å in graphite). The key feature of this geometry is the presence of a 3-fold coordinated interstitial atom between the graphene planes with magnetic moment $m_C = 0.155 \ \mu_B$. Although this sample has been found in our random search, one can identify a set of simple geometrical steps to construct it. Let us consider 4 in-plane unit cells of an AA-stacked graphite, namely a unit cell with 8 atoms and vertical periodicity equal to the interplane distance. In the top right panel of Fig. 5.11 4 such unit cells are shown. Now select an arbitrary carbon atom in the unit cell and apply the following procedure. We replace this atom with two atoms, one above and one below the original plane. In getting out of plane, these two atoms become close enough to form a bond between planes. This geometry has to be further relaxed to obtain the final structure

shown in the right panels of Fig. 5.11. Once we calculate the spin polarized electronic density, we find that a large magnetic moment appears on one of the two interstitial atoms. As shown in the right bottom panel of Fig. 5.11 the magnetic atom is part of a tetragon, a feature that we have discussed in Section 5.5 and that appears in 4 of the 34 magnetic samples with two sp^2 atoms. Possibly, the almost square form of the tetragon, with angles close to 90 degrees, is of importance.

The second example of graphite-like structure is AC14-0831 shown in Fig. 5.11. We can describe its structure as a graphite made of planes of graphene connected through an interplane dimer C2 (atoms M1 and M2 in Fig. 5.11 left-middle). Moreover, each graphene plane has a grain boundary [140, 141, 80] made of a continuous line of Stone-Wales 5-7-7-5 defects [142]. Another way to imagine the structure of this grain boundary is to join together two grains with zigzag edges reconstructed as zigzag-57 [56] (Fig. 5.11 top-left). The interplane dimer C2 forms one pentagon and one tetragon with bottom and top planes respectively (Fig. 5.11 left-middle). The tetragon is formed by bonds between the C2 dimer and two heptagons in the grain boundary in the graphene plane (atoms A and B in Fig. 5.11 left-top) while the pentagon is formed by bonds between the C2 dimer and 3 atoms belonging to the hexagons in the graphene plane (atoms C, D, E in Fig. 5.11 left-top). The parallel alignment of the A-B bond to the vector connecting the atoms C and D gives the possibility of connecting the planes through the interplanar dimer M1-M2 by forming a pentagon and a tetragon with planar arrangement.

The origin of the magnetic states in this configuration is again explained by the Lieb theorem [138, 91, 113] since the sp^3 atoms C and D, belonging to the same sublattice, break the bipartite lattice symmetry. This situation is similar to the one encountered in Chapter 4 for the junction of a nanotube with a graphene ribbon [143]. Also there, the sp^3 atoms were breaking the bipartite symmetry, leading to magnetic moments.

The last set of samples discovered in our search has a 3D ferro/ferri-magnetic structure with large values of J. The samples AC16-0070 and AC15-0776 studied by LDA-CA (point N4 and N9 in Fig. 5.8 top) have a complicated geometry that we do not show here because it cannot be described in a simplified way as done previously. Within the samples studied by GGA-PBE we select AC15-0267, AC10-1116 and AC09-0708 (points N4, N5, N12 in Fig. 5.8 bottom) and show two of them in Fig. 5.12. The sample AC15-0267 can be classified as a graphite-like geometry with modifications in the graphene plane (i.e. grain boundaries and/or point defects) and interplane atoms (see Fig. 5.12 left-middle) similar to the geometry of AC14-0831. One more example of magnetic states due to the presence of dangling bonds is given by the sample AC09-0708 shown in the right panels of Fig. 5.12. This sample also has a layered structure where the two fold coordinated atoms always connect two layers. Each layer itself is made of two pentagons and two octagons arranged along a line between two zigzag rows. A top view of the sample gives an image very similar to the high angle grain boundary found for graphene on Ni in ref. [83].

All structures presented in this section are reported in the Appendix in the xsf file format suitable for use in the VESTA program [36].
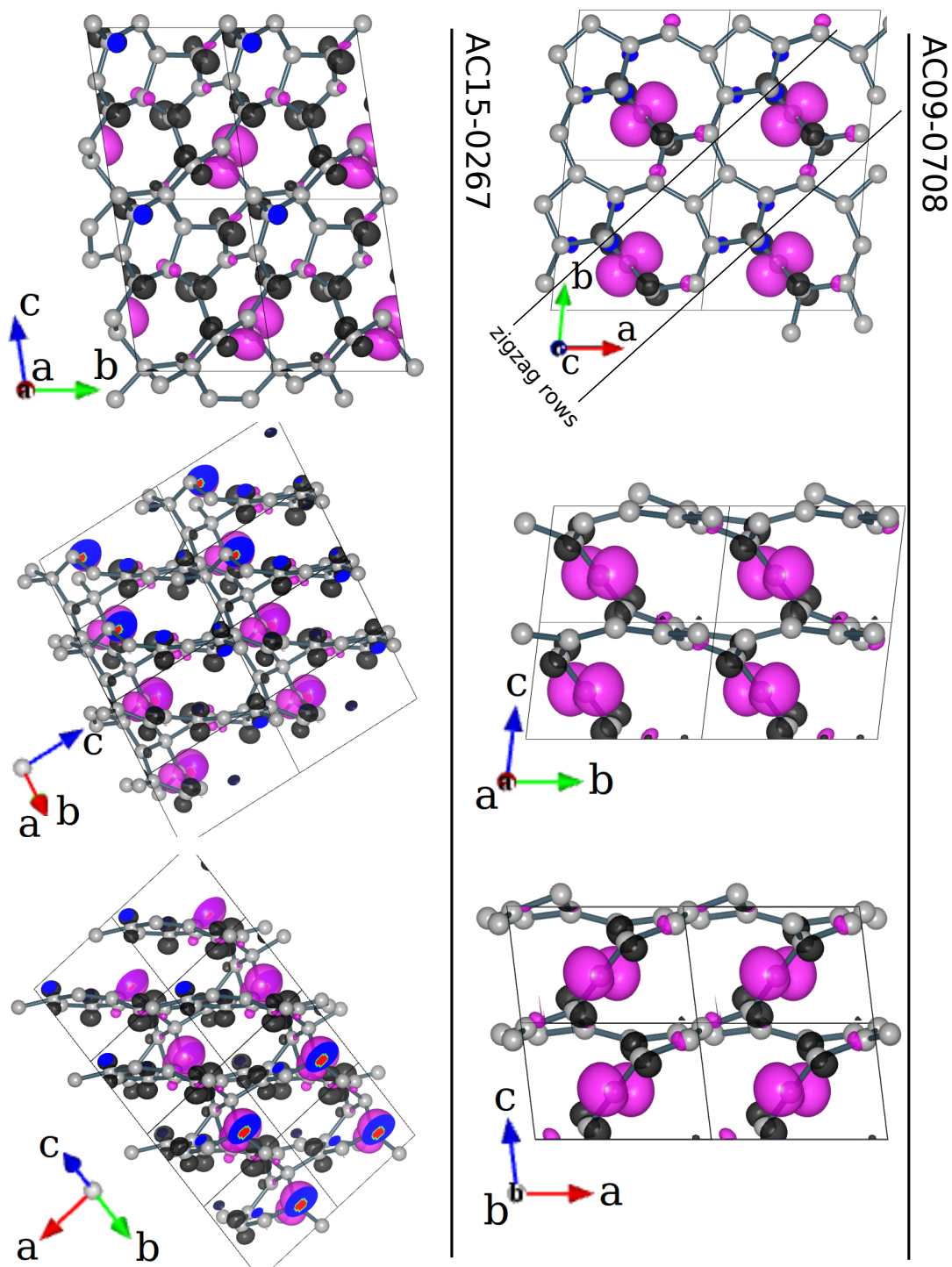
Figure 5.12: Spin density isosurface plot of the samples with 3D ferrimagnetic properties studied within GGA-PBE approximation.

5.8 Conclusions

In this chapter we have presented the results of a massive, automated search of disordered carbon structures with magnetic states. We have tried to identify the common structural features present in the samples where magnetic moments appear. In our analysis we have used elements of graph theory and the analogy to structural motifs in graphene grain boundaries. We believe that our computational approach can lead to progress in the understanding of $s-p$ electron magnetism. This task is however still far from complete and the ways to create magnetic order are still elusive and will require further investigations.

Appendix A

Geometry of magnetic carbon structures

To invite other contributions to this fascinating topic we give here the structures and coordinates of the selected samples presented in section 5.7 of chapter 5. Coordinates of the samples indicated in bold face are in the xsf file format suitable for use in the VESTA program [36]. It is also possible to download the same files from here [144] where, after the structural data presented in this appendix, also the magnetisation density on a 3D grid is given.

= AC07-0003.xsf (LDA-CA) =

```
CRYSTAL
PRIMVEC
3.612119 -0.753491 -0.012559
-0.753491 5.597208 -0.256742
-0.012559 -0.256742 3.212877
PRIMCOORD
7 1
6 0.366702 3.228975 2.998248
6 0.644662 1.159799 1.867044
6 2.698047 1.964710 2.547218
6 0.618532 4.630033 0.475717
6 0.858486 5.774530 1.165454
6 2.892894 0.688410 1.860012
6 1.346896 2.503804 -0.659426
```

= AC07-0010.xsf (LDA-CA) =

```
CRYSTAL
PRIMVEC
3.549133 -0.000652 -0.001402
-0.000652 3.549255 -0.001631
-0.001402 -0.001631 3.548629
PRIMCOORD
7 1
6 2.487469 0.751410 0.405783
6 -0.122821 1.583149 3.121223
6 1.650974 3.358448 3.119529
6 0.819916 2.419018 0.405182
6 0.817212 0.749293 2.285469
6 2.484001 2.415802 2.288480
6 1.652205 1.584366 1.345821
```

= AC09-0405.xsf (LDA-CA) =

```
CRYSTAL
PRIMVEC
4.772368 0.041943 -1.339252
0.041943 3.169901 -0.035346
-1.339252 -0.035346 4.773555
PRIMCOORD
9 1
6 1.379449 1.211283 2.375900
6 0.983459 -0.110845 2.765921
```

```
6 1.731633 2.488277 0.311727
6 -1.661513 2.375219 1.983419
6 3.442896 2.491156 2.023574
6 4.100400 2.240449 -0.345172
6 2.356199 2.181241 3.011144
6 -0.013667 2.686176 3.768721
6 0.745157 2.181604 1.399339
```

= AC14-0831.xsf (LDA-CA) =

```
CRYSTAL
PRIMVEC
4.849237 0.317760 -0.383480
0.317760 5.080545 -0.058149
-0.383480 -0.058149 4.645736
PRIMCOORD
14 1
6 2.868509 0.045732 1.162088
6 -0.239195 0.059033 3.929375
6 2.454660 1.172871 1.974821
6 4.936299 3.227961 3.941798
6 4.686594 5.385780 0.868419
6 4.025327 2.635564 -0.920744
6 -0.487281 0.957895 0.129901
6 0.829000 4.216112 0.368784
6 0.269912 5.772545 2.512603
6 1.226732 2.472597 3.621706
6 2.362227 4.210486 0.434003
6 3.590372 1.933145 2.353593
6 2.742908 3.215408 -0.508364
6 1.219785 1.478675 2.601759
```

= AC15-0776.xsf (LDA-CA) =

```
CRYSTAL
PRIMVEC
4.616000 -0.406854 -0.172872
-0.406854 4.847671 -0.140578
-0.172872 -0.140578 4.188634
PRIMCOORD
15 1
6 1.174550 4.103143 0.623598
6 1.861997 1.968623 0.582340
6 2.742942 4.269498 0.624322
```

```
  6 2.947446 1.780887 1.819937
6 3.008134 4.325478 2.102337
6 3.606176 0.447493 4.098199
6 0.082808 0.246539 3.294148
6 0.769103 2.766932 1.235723
6 2.688973 0.693498 2.844454
6 2.609411 2.977773 2.692222
6 1.258166 1.248708 3.352590
6 3.039953 2.914214 0.005657
6 1.063619 2.766570 2.693872
6 3.991898 1.903641 0.712595
6 0.446436 3.869272 3.498050


= AC16-0070.xsf (LDA-CA) =
CRYSTAL
PRIMVEC
4.822003 0.383144 -0.150519
0.383144 5.035109 -0.246954
-0.150519 -0.246954 4.188021
PRIMCOORD
16 1
6 0.809957 1.102835 0.422542
6 3.909180 0.951293 2.201017
6 0.567831 3.909486 0.634355
6 2.451197 1.309575 2.848269
6 5.031227 0.578290 3.141339
6 0.652162 3.680934 3.267093
6 1.535275 0.114944 2.561616
6 4.898265 3.509038 1.753393
6 2.235466 3.823814 3.055961
6 4.118321 4.717481 1.064850
6 2.890935 4.171439 0.341996
6 2.457371 2.654478 2.223465
6 4.411768 2.149276 1.243780
6 2.925331 2.687290 0.844562
6 1.281699 -0.175381 1.165825
6 1.988089 1.524544 4.249918
```

```
= AC09-0708.xsf (GGA-PBE) =
CRYSTAL
PRIMVEC
4.866303 0.206339 -0.236017
0.206687 4.865862 0.237583
-0.209562 0.208351 3.234590
PRIMCOORD
9 1
6 1.692902 3.991494 3.191736
6 2.966742 4.432779 2.816513
6 0.014111 2.312788 3.191486
6 2.332370 1.675497 1.267455
6 1.599288 2.407639 0.392077
6 0.409607 4.621718 3.121964
6 4.439134 1.245480 2.579592
6 3.063608 0.942698 2.143922
6 4.249940 3.802345 2.885633


= AC10-1116.xsf (GGA-PBE) =
CRYSTAL
PRIMVEC
3.398919 -0.533787 0.051873
-0.534963 4.344658 0.276706
0.048649 0.276078 4.854477
PRIMCOORD
10 1
6 -0.180366 1.048847 0.995151
6 1.171111 0.757593 0.371141
6 3.140779 0.760248 2.568651
6 1.939896 3.967189 3.548277
6 2.394987 1.586068 0.390720
6 0.918025 4.102250 4.682954
6 1.469178 3.876000 1.195374
6 0.167765 2.509957 3.019837
6 1.193294 3.293902 2.460597
6 3.082504 2.768839 4.267774
```

= AC13-0119.xsf (GGA-PBE) =
```
CRYSTAL
PRIMVEC
4.799652 0.587515 0.008143
0.585366 4.668862 0.367251
0.006508 0.368912 4.067691
PRIMCOORD
13 1
6 2.711552 1.253031 3.799337
6 3.408505 3.809068 1.825770
6 2.218403 3.792774 2.748473
6 1.402673 2.426417 1.046304
6 3.917130 -0.022107 1.946160
6 1.670094 1.322784 1.799694
6 1.458049 0.583712 3.091918
6 5.695524 5.145338 0.305913
6 2.761236 0.629607 1.171062
6 1.040714 3.769794 1.642575
6 4.421377 4.951445 3.773921
6 2.501746 2.842511 3.939301
6 3.708563 3.254647 0.500249
```

= AC15-0267.xsf (GGA-PBE) =
```
CRYSTAL
PRIMVEC
4.387947 0.245011 0.004477
0.254262 4.501578 -0.377553
-0.019412 -0.379486 5.783572
PRIMCOORD
15 1
6 0.996838 0.286437 0.113559
6 4.013682 0.534122 5.278529
6 2.938242 0.356469 2.968787
6 4.157717 4.527538 3.604890
6 1.634750 3.361754 4.547122
6 1.536083 3.983841 0.989995
6 2.182375 2.027602 4.687208
6 1.654130 1.681312 0.151850
6 3.773794 2.986816 0.908528
6 0.783315 3.288531 3.472803
6 0.904677 2.606292 1.133115
6 2.700176 -0.530954 1.844100
```

```
6 2.094739 1.438490 3.297868
6 3.172593 1.979415 -0.006875
6 1.172729 2.251077 2.586400
```

= AC15-0656.xsf (GGA-PBE) =
```
CRYSTAL
PRIMVEC
4.314439 0.344511 0.377673
0.278738 4.539489 -0.218486
0.363610 -0.315954 4.920256
PRIMCOORD
15 1
6 2.383225 1.298619 3.517846
6 0.670337 4.267562 3.171072
6 3.289150 0.662153 4.596275
6 3.196476 4.055108 -0.181615
6 1.082958 2.042807 3.640344
6 2.531218 1.753573 0.990425
6 2.379167 3.322134 0.754728
6 2.966738 3.612069 2.176384
6 0.377598 1.957753 2.250284
6 0.714909 3.278845 4.309695
6 1.742908 0.185062 2.800066
6 1.014680 4.018577 0.718130
6 4.487511 3.829772 2.274225
6 3.171762 2.094118 2.464346
6 1.262017 0.928980 1.514513
```

Bibliography

[1] Novoselov K S, Geim A K, Morozov S V, Jiang D, Zhang Y, Dubonos S V, Grigorieva I V and Firsov A A 2004 *Science* **306** 666–669

[2] Esquinazi P, Setzer A, Höhne R, Semmelhack C, Kopelevich Y, Spemann D, Butz T, Kohlstrunk B and Lösche M 2002 *Phys. Rev. B* **66**(2) 024429

[3] Esquinazi P, Spemann D, Höhne R, Setzer A, Han K H and Butz T 2003 *Phys. Rev. Lett.* **91**(22) 227201

[4] Esquinazi P and Hhne R 2005 *J. Magn. Magn. Mater.* **290-291** 20–27

[5] Mombrú A W, Pardo H, Faccio R, de Lima O F, Leite E R, Zanelatto G, Lanfredi A J C, Cardoso C A and Araújo-Moreira F M 2005 *Phys. Rev. B* **71**(10) 100404

[6] Ohldag H, Tyliszczak T, Höhne R, Spemann D, Esquinazi P, Ungureanu M and Butz T 2007 *Phys. Rev. Lett.* **98**(18) 187204

[7] Talapatra S, Ganesan P G, Kim T, Vajtai R, Huang M, Shima M, Ramanath G, Srivastava D, Deevi S C and Ajayan P M 2005 *Phys. Rev. Lett.* **95**(9) 097201

[8] Rode A, Elliman R, Gamaly E, Veinger A, Christy A, Hyde S and Luther-Davies B 2002 *Applied Surface Science* **197-198** 644–649

[9] Rode A V, Gamaly E G, Christy A G, Fitz Gerald J G, Hyde S T, Elliman R G, Luther-Davies B, Veinger A I, Androulakis J and Giapintzakis J 2004 *Phys. Rev. B* **70**(5) 054407

[10] Cervenka J, Katsnelson M I and Flipse C F J 2009 *Nat. Phys.* **5** 840–844

[11] Edwards D M and Katsnelson M I 2006 *J. Phys.: Condens. Matter* **18** 7209–7225

[12] Takahashi M, Turek P, Nakazawa Y, Tamura M, Nozawa K, Shiomi D, Ishikawa M and Kinoshita M 1991 *Phys. Rev. Lett.* **67**(6) 746–748

[13] Murata K, Ushijima H, Ueda H and Kawaguchi K 1992 *J. Chem. Soc., Chem. Commun.* (7) 567–569

[14] Korshak Y V, Medvedeva T V, Ovchinnikov A A and Spector V N 1987 *Nature* **326** 370–372

[15] Torrance J B, Oostra S and Nazzal A 1987 *Synth. Met.* **19** 709–714

[16] Ovchinnikov A A and Spector V N 1988 *Synth. Met.* **27** B615–B624

[17] Makarova T L, Sundqvist B, Hohne R, Esquinazi P, Kopelevich Y, Scharff P, Davydov V A, Kashevarova L S and Rakhmanina A V 2001 *Nature* **413**(6857) 716–718

[18] Makarova T and Palacio F 2006 *Carbon Based Magnetism: An Overview of the Magnetism of Metal Free Carbon-based Compounds and Materials* (Elsevier Science)

[19] Sepioni M, Nair R R, Tsai I L, Geim A K and Grigorieva I V 2012 *EPL (Europhysics Letters)* **97** 47001

[20] Hohenberg P and Kohn W 1964 *Phys. Rev.* **136**(3B) B864–B871

[21] Kohn W and Sham L J 1965 *Phys. Rev.* **140**(4A) A1133–A1138

[22] Soler J M, Artacho E, Gale J D, Garcia A, Junquera J, Ordejon P and Sanchez-Portal D 2002 *J. Phys.: Condens. Matter* **14** 2745–2779

[23] Sanchez-Portal D, Ordejon P and Canadell E 2004 *Principles and Applications of Density functional Theory in Inorganic Chemistry II* 113 (Berlin: Springer)

[24] Artacho E, Anglada E, Dieguez O, Gale J D, Garcia A, Junquera J, Martin R M, Ordejon P, Pruneda J M, Sanchez-Portal D and Soler J M 2008 *J. Phys.: Condens. Matter* **20** 064208

[25] Junquera J, Paz O, Sánchez-Portal D and Artacho E 2001 *Phys. Rev. B* **64**(23) 235111

[26] Ceperley D M and Alder B J 1980 *Phys. Rev. Lett.* **45**(7) 566–569

[27] Perdew J P and Zunger A 1981 *Phys. Rev. B* **23**(10) 5048–5079

[28] Perdew J P, Burke K and Ernzerhof M 1996 *Phys. Rev. Lett.* **77**(18) 3865–3868

[29] Parr R G and Yang W 1989 *Density-Functional Theory of Atoms and Molecules* (Oxford University Press)

[30] Dreizler R M and Gross E K U 1990 *Density Functional Theory* (Springer)

[31] Martin R M 2010 *Electronic structure basic theory and practical methods* (Cambridge University Press)

[32] Rydberg H, Dion M, Jacobson N, Schröder E, Hyldgaard P, Simak S I, Langreth D C and Lundqvist B I 2003 *Phys. Rev. Lett.* **91**(12) 126402

[33] Boukhvalov D W and Katsnelson M I 2008 *Phys. Rev. B* **78**(8) 085413

[34] Numerov B V 1927 *Astronomische Nachrichten* **230** 359

[35] E A, D S P, P O, A G and M S J 1999 *Phys. Stat. Sol. (b)* **215** 809

[36] Momma K and Izumi F 2008 *J. Appl. Crystallogr.* **41** 653–658

[37] Frenkel J 1926 *Z. Phys.* **37** 572

[38] Orowan E 1934 *Z. Phys.* **89** 605, 634

[39] Taylor G I 1934 *Proc. Roy. Soc.* **A145** 362

[40] Polanyi M 1934 *Z. Phys.* **89** 660

[41] Peierls R E 1940 *Proc. Phys. Soc.* **52** 23

[42] Nabarro F R N 1947 *Proc. Phys. Soc.* **59** 256

[43] Hirth J and Lothe J 1982 *Theory of Dislocations* (Wiley)

[44] Frank F C 1951 *Phil. Mag.* **42** 809

[45] Yazyev O V and Louie S G 2010 *Phys. Rev. B* **81**(19) 195420

[46] Kronberg M L and Wilson F H 1949 *J. Metals* **185** 501

[47] Gurtov V A and Osaulenko R N 2007 *Solid state physics for engineers* (Technosphera)

[48] Nakada K, Fujita M, Dresselhaus G and Dresselhaus M S 1996 *Phys. Rev. B* **54**(24) 17954–17961

[49] Han M Y, Özyilmaz B, Zhang Y and Kim P 2007 *Phys. Rev. Lett.* **98**(20) 206805

[50] Chen Z, Lin Y M, Rooks M J and Avouris P 2007 *Physica E: Low-dimensional Systems and Nanostructures* **40** 228 – 232

[51] Fujita M, Wakabayashi K, Nakada K and Kusakabe K 1996 *Journal of the Physical Society of Japan* **65** 1920–1923

[52] Dubois S M M, Zanolli Z, Declerck X and Charlier J C 2009 *Eur. Phys. J. B* **72**(1) 1–24

[53] Son Y W, Cohen M L and Louie S G 2006 *Phys. Rev. Lett.* **97**(21) 216803

[54] Castro Neto A H, Guinea F, Peres N M R, Novoselov K S and Geim A K 2009 *Rev. Mod. Phys.* **81**(1) 109–162

[55] Brey L and Fertig H A 2006 *Phys. Rev. B* **73**(23) 235411

[56] Koskinen P, Malola S and Häkkinen H 2008 *Phys. Rev. Lett.* **101**(11) 115502

[57] Rakyta P, Kormányos A, Cserti J and Koskinen P 2010 *Phys. Rev. B* **81**(11) 115411

[58] Wassmann T, Seitsonen A P, Saitta A M, Lazzeri M and Mauri F 2008 *Phys. Rev. Lett.* **101**(9) 096402

[59] Wassmann T, Seitsonen A P, Saitta A M, Lazzeri M and Mauri F 2009 *physica status solidi (b)* **246** 2586–2591

[60] Kunstmann J, Özdoğan C, Quandt A and Fehske H 2011 *Phys. Rev. B* **83**(4) 045414

[61] Girit C O, Meyer J C, Erni R, Rossell M D, Kisielowski C, Yang L, Park C H, Crommie M F, Cohen M L, Louie S G and Zettl A 2009 *Science* **323** 1705–1708

[62] Koskinen P, Malola S and Häkkinen H 2009 *Phys. Rev. B* **80**(7) 073401

[63] Chuvilin A, Meyer J C, Algara-Siller G and Kaiser U 2009 *New J. Phys.* **11** 083019

[64] Li J, Li Z, Zhou G, Liu Z, Wu J, Gu B L, Ihm J and Duan W 2010 *Phys. Rev. B* **82**(11) 115410

[65] Los J H, Ghiringhelli L M, Meijer E J and Fasolino A 2005 *Phys. Rev. B* **72**(21) 214102

[66] Cresti A, Nemec N, Biel B, Niebler G, Triozon F, Cuniberti G and Roche S 2008 *Nano Research* **1**(5) 361–394

[67] CEA *MD simulations are performed with the parallel molecular dynamics code STAMP developed at CEA (France) using the original LCBOPII potential.*

[68] Chandler D 1987 *Introduction to Modern Statistical Mechanics* (Oxford University Press)

[69] Hänggi P, Talkner P and Borkovec M 1990 *Rev. Mod. Phys.* **62**(2) 251–341

[70] Los J H and et all *work in progress*

[71] Berger C, Song Z, Li T, Li X, Ogbazghi A Y, Feng R, Dai Z, Marchenkov A N, Conrad E H, First P N and de Heer W A 2004 *J. Phys. Chem. B* **108** 19912–19916

[72] Berger C, Song Z, Li X, Wu X, Brown N, Naud C, Mayou D, Li T, Hass J, Marchenkov A N, Conrad E H, First P N and de Heer W A 2006 *Science* **312** 1191–1196

[73] Blake P, Brimicombe P D, Nair R R, Booth T J, Jiang D, Schedin F, Ponomarenko L A, Morozov S V, Gleeson H F, Hill E W, Geim A K and Novoselov K S 2008 *Nano Lett.* **8** 1704–1708

[74] Hernandez Y, Nicolosi V, Lotya M, Blighe F M, Sun Z, De S, T M, Holland B, Byrne M, Gun'Ko Y K, Boland J J, Niraj P, Duesberg G, Krishnamurthy S, Goodhue R, Hutchison J, Scardaci V, Ferrari A C and Coleman J N 2008 *Nat. Nanotechnol.* **3**(9) 563–568

[75] Choucair M, Thordarson P and Stride J A 2009 *Nat. Nanotechnol.* **4**(1) 30–33

[76] Li X, Cai W, An J, Kim S, Nah J, Yang D, Piner R, Velamakanni A, Jung I, Tutuc E, Banerjee S K, Colombo L and Ruoff R S 2009 *Science* **324** 1312–1314

[77] Bae S, Kim H, Lee Y, Xu X, Park J S, Zheng Y, Balakrishnan J, Lei T, Ri Kim H, Song Y I, Kim Y J, Kim K S, Ozyilmaz B, Ahn J H, Hong B H and Iijima S 2010 *Nat. Nanotechnol.* **5**(8) 574–578

[78] Miller D L, Kubista K D, Rutter G M, Ruan M, de Heer W A, First P N and Stroscio J A 2009 *Science* **324** 924–927

[79] Coraux J, N'Diaye A T, Busse C and Michely T 2008 *Nano Lett.* **8** 565–570

[80] Loginova E, Nie S, Thürmer K, Bartelt N C and McCarty K F 2009 *Phys. Rev. B* **80**(8) 085430

[81] Park H J, Meyer J, Roth S and Skakalova V 2010 *Carbon* **48** 1088–1094

[82] Huang P Y, Ruiz-Vargas C S, van der Zande A M, Whitney W S, Levendorf M P, Kevek J W, Garg S, Alden J S, Hustedt C J, Zhu Y, Park J, McEuen P L and Muller D A 2011 *Nature* **469** 389

[83] Lahiri J, Lin Y, Bozkurt P, Oleynik I I and Batzill M 2010 *Nat. Nanotechnol.* **5** 326–329

[84] Grantab R, Shenoy V B and Ruoff R S 2010 *Science* **330** 946–948

[85] Malola S, Häkkinen H and Koskinen P 2010 *Phys. Rev. B* **81**(16) 165447

[86] Carlsson J M, Ghiringhelli L M and Fasolino A 2011 *Phys. Rev. B* **84**(16) 165423

[87] Yazyev O V and Louie S G 2010 *Nat. Mater.* **9** 806–809

[88] Valiev R Z, Islamgaliev R K and Alexandrov I V 2000 *Prog. Mater. Sci.* **45** 103–189

[89] Mesaros A, Papanikolaou S, Flipse C F J, Sadri D and Zaanen J 2010 *Phys. Rev. B* **82**(20) 205119

[90] Kotakoski J, Krasheninnikov A V, Kaiser U and Meyer J C 2011 *Phys. Rev. Lett.* **106**(10) 105505

[91] Yazyev O V 2010 *Rep. Prog. Phys.* **73** 056501

[92] Martínez-Martín D, Jaafar M, Pérez R, Gómez-Herrero J and Asenjo A 2010 *Phys. Rev. Lett.* **105**(25) 257203

[93] Python command line utility to print xyz-geometry to eps file format URL `http://sourceforge.net/projects/xyz2eps/`

[94] Python software foundation, python programming language, version 2.6.5 URL

`http://www.python.org/`

[95] Fasolino A, Los J H and Katsnelson M I 2007 *Nat. Mater.* **6** 858–861

[96] Los J H, Katsnelson M I, Yazyev O V, Zakharchenko K V and Fasolino A 2009 *Phys. Rev. B* **80**(12) 121405

[97] Zakharchenko K V, Katsnelson M I and Fasolino A 2009 *Phys. Rev. Lett.* **102**(4) 046808

[98] Karssemeijer L J and Fasolino A 2011 *Surf. Sci.* **605** 1611–1615

[99] Kroes J M H, Akhukov M A, Los J H, Pineau N and Fasolino A 2011 *Phys. Rev. B* **83**(16) 165411

[100] Zakharchenko K V, Los J H, Katsnelson M I and Fasolino A 2010 *Phys. Rev. B* **81**(23) 235439

[101] Troullier N and Martins J L 1991 *Phys. Rev. B* **43**(3) 1993–2006

[102] Kleinman L and Bylander D M 1982 *Phys. Rev. Lett.* **48**(20) 1425–1428

[103] Monkhorst H J and Pack J D 1976 *Phys. Rev. B* **13**(12) 5188–5192

[104] Saito R, Dresselhaus G and Dresselhaus M S 1988 *Physical Properties of Carbon Nanotubes* (Imperial College Press)

[105] Zakharchenko K V, Fasolino A, Los J H and Katsnelson M I 2011 *J. Phys.: Condens. Matter* **23** 202202

[106] López-Sancho M P, de Juan F and Vozmediano M A H 2009 *Phys. Rev. B* **79**(7) 075413

[107] Yazyev O V and Katsnelson M I 2008 *Phys. Rev. Lett.* **100**(4) 047209

[108] Bhandary S, Eriksson O, Sanyal B and Katsnelson M I 2010 *Phys. Rev. B* **82**(16) 165405

[109] Liu Z, Suenaga K, Harris P J F and Iijima S 2009 *Phys. Rev. Lett.* **102**(1) 015501

[110] Wimmer M, Akhmerov A R and Guinea F 2010 *Phys. Rev. B* **82**(4) 045409

[111] van Ostaay J A M, Akhmerov A R, Beenakker C W J and Wimmer M 2011 *Phys. Rev. B* **84**(19) 195434

[112] Jia X, Campos-Delgado J, Terrones M, Meunier V and Dresselhaus M S 2011 *Nanoscale* **3**(1) 86–95

[113] Katsnelson M I 2012 *Graphene: Carbon in Two Dimensions* (Cambridge University Press)

[114] Ivanovskaya V V, Zobelli A, Wagner P, Heggie M I, Briddon P R, Rayson M J and Ewels C P 2011 *Phys. Rev. Lett.* **107**(6) 065502

[115] Chernozatonskii L A, Sheka E F and Artyukh A A 2009 *JETP Letters* **89** 352–356

[116] Artyukh A A, Chernozatonskii L A and Sorokin P B 2010 *physica status solidi (b)* **247** 2927–2930

[117] Kim W Y and Kim K S 2008 *Nature Nanotech.* **3** 408–412

[118] Hill E W, Geim A K, Novoselov K, Schedin F and Blake P 2006 *IEEE Trans. Magn.* **42** 2694–2696

[119] Ma Z and Sheng W 2011 *Appl. Phys. Lett.* **99**(8) 083101

[120] Son Y W, Cohen M L and Louie S G 2006 *Nature* **444** 347–349

[121] Abanin D A, Lee P A and Levitov L S 2006 *Phys. Rev. Lett.* **96**(17) 176803

[122] Zhang Y T, Jiang H, Sun Q f and Xie X C 2010 *Phys. Rev. B* **81**(16) 165404

[123] Hod O, Barone V, Peralta J E and Scuseria G E 2007 *Nano Lett.* **7** 2295–2299

[124] Zheng X H, Wang R N, Song L L, Dai Z X, Wang X L and Zeng Z 2009 *Appl. Phys. Lett.* **95**

[125] Soriano D, Muñoz Rojas F, Fernández-Rossier J and Palacios J J 2010 *Phys. Rev. B* **81**(16) 165409

[126] Martins T B, da Silva A J R, Miwa R H and Fazzio A 2008 *Nano Lett.* **8** 2293–2298

[127] Lisenkov S, Andriotis A N and Menon M 2012 *Phys. Rev. Lett.* **108**(18) 187208

[128] Ezawa M 2006 *Phys. Rev. B* **73**(4) 045432

[129] Wehling T O, Yuan S, Lichtenstein A I, Geim A K and Katsnelson M I 2010 *Phys. Rev. Lett.* **105** 056802

[130] Yuan S, De Raedt H and Katsnelson M I 2010 *Phys. Rev. B* **82** 115448

[131] Rode A, Hyde S, Gamaly E, Elliman R, McKenzie D and Bulcock S 1999 *Applied Physics A* **69**(1) S755–S758

[132] Wales D J, Miller M A and Walsh T R 1998 *Nature* **394**(6695) 758–760

[133] Generate and test search URL `http://intelligence.worldofcomputing.net/ai-search/generate-and-test-search.html`

[134] Genetic algorithms URL `http://intelligence.worldofcomputing.net/machine-learning/genetic-algorithms.html`

[135] Akhukov M A, Fasolino A, Gornostyrev Y N and Katsnelson M I 2012 *Phys. Rev. B* **85**(11) 115407

[136] Anglada E, M Soler J, Junquera J and Artacho E 2002 *Phys. Rev. B* **66**(20) 205101

[137] Harary F 1969 *Graph theory* (Addison Wesley publishing company)

[138] Lieb E H 1989 *Phys. Rev. Lett.* **62**(10) 1201–1204

[139] Zhou J, Wang Q, Sun Q, Chen X S, Kawazoe Y and Jena P 2009 *Nano Letters* **9** 3867–3870

[140] Miller D L, Kubista K D, Rutter G M, Ruan M, de Heer W A, First P N and Stroscio J A 2009 *Science* **324** 924–927

[141] Coraux J, N'Diaye A T, Busse C and Michely T 2008 *Nano Letters* **8** 565–570

[142] Stone A and Wales D 1986 *Chemical Physics Letters* **128** 501 – 503

[143] Akhukov M A, Yuan S, Fasolino A and Katsnelson M I 2012 *New J. of Phys.* **14** 123012

[144] URL `ftp://ftp.science.ru.nl/pub/tcm/ac/`

Summary

In this thesis we have studied the structural and magnetic properties of different carbon systems like graphene edges, grain boundaries in graphene and disordered carbon with a focus on their magnetic properties. For each type of system we have found situations that might give rise to magnetic order if one would have enough control on the structure. The manuscript is organized as follows.

After the introductory chapter 1, in chapter 2 we have studied the 5-7 reconstruction of the zigzag graphene edges by a combination of first principles and semi-empirical calculations. We have shown that this structure has the lowest energy also when spin-polarized calculations are performed. We have identified a reaction coordinate for the reconstruction that we have used to evaluate the free energy barrier by the technique of umbrella sampling in Monte Carlo simulations.

In chapter 3 we have examined the possibility to have grain boundaries in graphene with low formation energy and dangling bonds which can give rise to magnetic states. To construct grain boundaries we have adopted ideas of the theory of nanotubes. Our approach allows to model not only symmetric grain boundaries described in the standard 'coincidence site lattice' theory of grain boundaries in solids but also non symmetric ones which have higher energy and internal stress. For many possible structures we have studied the electronic properties and the influence of curvature on the magnetic properties as well as the influence of saturation of dangling bonds by hydrogen, hydroxyl group and oxygen. We have found a promising configuration with 5-8-7 rings where the dangling bonds give rise to magnetic states.

In chapter 4 we have studied the electronic and magnetic properties of nanoribbons terminated by nanotubes, a recently proposed low energy structure. We have found that, depending on the type of junction between the ribbon and nanotubes, many different properties can be realized, including magnetic states. Based on the found properties, we have proposed several possible applications of this type of systems for spintronics.

In chapter 5 we studied the magnetic properties of disordered carbon based on a 'generate and test' approach which samples the coordinate space to find magnetic configurations in pure carbon systems. We have discovered a wealth of structures with

magnetic moments that could give ferromagnetic order. By comparing geometries with and without magnetic states we have identified a few criteria which have to be satisfied to expect magnetism in disordered carbon.

Samenvatting

In dit proefschrift hebben we de structurele en magnetische eigenschappen van verschillende koolstofsystemen bestudeerd, zoals de randen van grafeen, korrelgrenzen in grafeen en ongeordende koolstof, waarbij de focus ligt op hun magnetische eigenschappen. Voor ieder type systeem hebben we gevallen gevonden die aanleiding zouden kunnen geven tot magnetische orde, als men voldoende controle over de structuur zou hebben. De opzet van het manuscript is als volgt.

Na het inleidende hoofdstuk 1, hebben we in hoofdstuk 2 de 5-7 reconstructie van zigzagranden van grafeen bestudeerd met een combinatie van *ab initio* en semi-empirische methoden. We hebben laten zien dat deze structuur de laagste energie heeft, ook in berekeningen waarin de spinpolarisatie wordt meegenomen. We hebben een reactiecoördinaat voor het proces van de reconstructie aangewezen, die we hebben gebruikt om de vrije-energiebarrière te bepalen in Monte-Carlosimulaties met de techniek van 'umbrella sampling'.

In hoofdstuk 3 hebben we de mogelijkheid onderzocht van korrelgrenzen in grafeen met een lage formatie-energie en vrije bindingen, die aanleiding kunnen geven tot magnetische toestanden. Om korrelgrenzen te construeren hebben we ideeën gebruikt uit de theorie van nanobuizen. Onze aanpak stelt ons niet alleen in staat om symmetrische korrelgrenzen te modelleren, die worden beschreven in de standaardtheorie van 'coincidence site lattices' in vaste stoffen, maar ook niet-symmetrische korrelgrenzen die een hogere energie hebben en een interne spanning. Voor veel mogelijke structuren hebben we de elektronische eigenschappen en de invloed van kromming op de magnetische eigenschappen bestudeerd, evenals de invloed van verzadiging van de vrije bindingen met waterstof, hydroxylgroepen en zuurstof. We hebben een veelbelovende configuratie met 5-8-7 ringen gevonden, waarin de vrije bindingen aanleiding geven tot magnetische toestanden.

In hoofdstuk 4 hebben we de elektronische en magnetische eigenschappen bestudeerd van grafeenstroken met nanobuizen aan de zijkanten, een onlangs voorgestelde structuur met een lage energie. We hebben gevonden dat, afhankelijk van het type overgang tussen de strook en de nanobuizen, veel verschillende eigenschappen gerealiseerd kunnen worden, waaronder magnetische toestanden. Op basis van de eigenschappen die we

hebben gevonden, hebben we een aantal mogelijke toepassingen van dit type systemen voor spintronica voorgesteld.

In hoofdstuk 5 hebben we de magnetische eigenschappen van ongeordend koolstof bestudeerd met behulp van een 'generate en test' methode, die de coördinaatruimte doorloopt om magnetische configuraties in systemen van zuiver koolstof te vinden. We hebben veel verschillende structuren met magnetische momenten ontdekt die aanleiding zouden kunnen geven tot ferromagnetische orde. Door structuren met en zonder magnetische toestanden te vergelijken hebben we een aantal criteria opgesteld waaraan moet worden voldaan wil men magnetisme in ongeordend koolstof verwachten.

Publications

Akhukov M. A.; Fasolino A.; Katsnelson M. I., "Structure and magnetism of disordered carbon", in preparation.

Akhukov M. A.; Yuan Shengjun; Fasolino A.; Katsnelson M. I., "Electronic, magnetic and transport properties of graphene ribbons terminated by nanotubes", *New J. of Phys.* **14**, 123012 (2012).

Akhukov, M. A.; Fasolino, A.; Gornostyrev, Y. N.; Katsnelson M. I., "Dangling bonds and magnetism of grain boundaries in graphene", Phys. Rev. B **85** 115407 (2012).

Kroes, J. M. H.; Akhukov, M. A.; Los, J. H.; Pineau N.; Fasolino A., "Mechanism and free-energy barrier of the type-57 reconstruction of the zigzag edge of graphene", Phys. Rev. B **83** 165411 (2011).

Curriculum vitae

Name:	Mikhail Aleksandrovich Akhukov
Date of birth:	May 28, 1982
Place of birth:	Orenburg, Russian Federation
e-mail:	ma.akhukov@gmail.com

Summary

4+ years experience of scientific research in the field of computational condensed matter physics. 4+ years experience of software programming and engineering in the field of application programming, testing, virtualization and automation.

Education

Nov 2008 - Feb 2013	**Radboud University Nijmegen, Netherlands.** PhD research in computational condensed matter physics.
Sep 2005 - Jun 2007	**Moscow State University named after Lomonosov.** Studying applied mathematics and computer science.
Sep 1999 - Jun 2004	**Orenburg State University**, Radio physics and electronics, Specialist (MSc equivalent). Graduate work "Calculation ab intio electronic characteristics of small molecules for spectroscopy and molecular electronics", supervisor Prof. M. G. Kucherenko.
Sep 1997 - Jun 1999	**College of Electronics and Business, Orenburg** Studying programming.

Work experience (Moscow, Russia)

Sep 2006 - Oct 2008	**Parallels - Virtualization and Automation Solutions.** Autotest software developer, quality assurance department. Implementation of C++ autotest, automation of deploy system (shell and Python scripting).
May 2005 - May 2006	**Mosautomat, Startup IT project.** Application software programmer (Borland C++ Builder). Implementation of software for the internet kiosk.
Aug 2004 - Apr 2005	**ISC Komci AST, Consulting and Service Center.** Computer service engineer.